ATHANASIOS MARGIOLAKIS

ENHANCED TERAHERTZ EMISSION FROM ULTRAFAST LASER ABLATED GALLIUM ARSENIDE DEVICES

ENHANCED TERAHERTZ EMISSION FROM ULTRAFAST LASER ABLATED GALLIUM ARSENIDE DEVICES

ATHANASIOS MARGIOLAKIS

University of Crete
December 2018

Supervisor Prof Tsironis Giorgos
Physics Department
School of Sciences and Engineering
University of Crete

Co-Supervisor Prof Dani Keshav
Femtosecond Spectroscopy Unit
Okinawa Institute of Science and Technology - Graduate University

ABSTRACT

In this thesis research, is presented the study and development of the first photoconductive antenna for generating Terahertz (THz), made of a Gallium Arsenide (GaAs) substrate, treated with femtosecond laser pulses, demonstrating increased performance compared to non-ablated antennas. Ripples are observed on the surface of the device after the laser ablation and we assume they are responsible for the increased performance. They are studied theoretically and experimentally, in order to explain this behavior. For the first time, a theoretical model is made to study GaAs ultrafast dynamics under irradiation of femtosecond laser pulses. In this model, energy balance equations are used to explain the ultrashort time-scales and evolution of dynamics. They are resolved numerically due to their coupled non-linear complexity, while the stability of the solution is ensured. Evolution of carrier density, electron and lattice temperature are the measured variables in order to obtain the thermal response of GaAs. The optical properties with dependence to fluence and pulse duration of the laser are studied, namely reflectivity and dielectric constant. The ripple wavelength is numerically calculated from our model and compared to our experimental data. The material's damage threshold dependence on laser pulse duration was also calculated.

A parametric analysis based on the properties of the ablation laser pulse and how it affects the ripples was performed and the measured properties are the applied power intensity, the overlapping area on each spot, polarization angle and number of pulses per spot. In the last chapter, using THz-TDS setup, the laser ablated GaAs antenna is measured for its THz generation performance and compared to a non-ablated antenna. Despite higher THz efficiency the following I-V measurements of the photocurrent, return lower values. To explain this discrepancy, an Optical Pump THz Probe (OPTP) setup is used to measure the excited carrier lifetime and photoconductivity. Complementary, Fourier Transform Infrared (FTIR) measurements are performed, to confirm higher photo-absorption and Hall effect measurements are made for measuring the level of doping, sheet concentration and carrier mobility.

READING TIP

By using the **Backspace** key, you can return to the page where you clicked a hyperlink, which transferred you to a figure, equation, reference, section or acronym. This feature might not work with all PDF readers and certainly not on prints. Test it here by clicking this HyperLink (HL) and then pressing Backspace to return to this page.

PUBLICATIONS

Article 6 is awaiting publication!

The following articles were part of the PhD work and might contain ideas and figures that are explained in this thesis:

[1] A. Margiolakis, G. D. Tsibidis, K. M. Dani, and G. P. Tsironis. "Ultrafast dynamics and subwavelength periodic structure formation following irradiation of GaAs with femtosecond laser pulses." In: *Phys. Rev. B* 98 (22 2018), p. 224103. DOI: 10.1103/PhysRevB.98.224103. URL: https://link.aps.org/doi/10.1103/PhysRevB.98.224103.

[2] Julien Madéo, Athanasios Margiolakis, Zhen-Yu Zhao, Peter J. Hale, Michael K. L. Man, Quan-Zhong Zhao, Wei Peng, Wang-Zhou Shi, and Keshav M. Dani. "Ultrafast properties of femtosecond-laser-ablated GaAs and its application to terahertz optoelectronics." In: *Optics Letters* 40.14 (July 2015), p. 3388. ISSN: 0146-9592. DOI: 10.1364/OL.40.003388. URL: https://www.osapublishing.org/abstract.cfm?URI=ol-40-14-3388.

[3] Michael K.L. Man, Athanasios Margiolakis, Skylar Deckoff-Jones, Takaaki Harada, E. Laine Wong, M. Bala Murali Krishna, Julien Madéo, Andrew Winchester, Sidong Lei, Robert Vajtai, Pulickel M. Ajayan, and Keshav M. Dani. "Imaging the motion of electrons across semiconductor heterojunctions." In: *Nature Nanotechnology* 12.1 (Oct. 2017), pp. 36–40. ISSN: 17483395. DOI: 10.1038/nnano.2016.183. URL: http://www.nature.com/doifinder/10.1038/nnano.2016.183.

[4] S. Spence, T. Harada, A. Margiolakis, S. Deckoff-Jones, A.N. Shugar, J.F. Hamm, K.M. Dani, and A.R. Dani. "Applicability of Femtosecond Lasers in the Cross-section Sampling of Works of Art." In: *MRS Advances* 2.33-34 (Mar. 2017), pp. 1801–1804. ISSN: 20598521. DOI: 10.1557/adv.2017.242. URL: https://www.cambridge.org/core/product/identifier/S2059852117002420/type/journal{_}article.

[5] Takaaki Harada, Stephanie Spence, Athanasios Margiolakis, Skylar Deckoff-Jones, Rebecca Ploeger, Aaron N. Shugar, James F. Hamm, Keshav M. Dani, and Anya R. Dani. "Obtaining cross-sections of paint layers in cultural artifacts using fem-

tosecond pulsed lasers." In: *Materials* 10.2 (Jan. 2017), p. 107. ISSN: 19961944. DOI: 10.3390/ma10020107. URL: http://www.mdpi.com/1996-1944/10/2/107.

[6] Anya Dani, Taro Kuranari, Märt Toots, Athanasios Margiolakis, and Jennifer Mass. "Characterization and Provenance Study of 17th-18th Century Archaeological Ceramics from Okinawa and Ishigaki Islands." In: *Archaeometry* (2018).

"It is the mark of an educated mind to be able to entertain a thought without accepting it."
— Aristotle

ACKNOWLEDGMENTS

Firstly, I would like to express my sincere gratitude to my supervisor Prof. G. Tsironis for the continuous support of my Ph.D study and related research, for his patience, motivation, and immense knowledge. His guidance throughout my academic years has helped me in my research. The members of his group for the interesting meetings and the feedback for my presentation.

My sincere thanks also goes to Prof. K. M. Dani, who provided me an opportunity to join their team as a special research student in OIST graduate university, and who gave access to the laboratory and research facilities. I thank my fellow labmates, Pete, Balu, Julien, Taka, Michael, and Skylar for the stimulating discussions, for the sleepless nights we were working together before deadlines, and for all the fun we have had in the two years I spend there. Without their precious support, it would not be possible to conduct this research.

Also I thank the researchers in FORTH, Dr. G. Tsibidis for the guidance, collaboration and his unlimited support in the theoretical part of this work. Dr. E. Stratakis for giving me the opportunity to work on his team laser labs for some personal projects, with the help of Vangelis, Antonis and Elmina.

A thank you to the rest of my Ph.D committee Prof. Perakis, Prof. Makris, Prof. Kominis and Prof Zotos.

My sincere thanks also goes to my colleagues in the University of Crete and friends, Savvas, Alexandros, Giorgos, Irina, Leonidas, Dana, for giving me motivation and interesting scientific discussions to keep me going in finishing this work. A special thank goes to the MRG-UoC for hosting me the last two years in their offices and M.D. P. D. Sfirakis for his immense contribution in medicine.

Last but not the least, I would like to thank my parents, my brother, my sister and Aria for supporting me spiritually throughout writing this thesis and my life in general.

CONTENTS

LIST OF FIGURES

LIST OF TABLES

ACRONYMS

THz Terahertz

TDS Time-Domain Spectroscopy

FDS Frequency-Domain Spectroscopy

GaAs Gallium Arsenide

SI	Semi-Insulating
OPTP	Optical-Pump THz-Probe
SPPs	Surface Plasmon Polaritons
NIR	Near Infrared
IR	Infrared
DC	Direct Current
CW	Continuous Wave
FTIR	Fourier-transform infrared spectroscopy
FT-FIR	Fourier-transform far infrared spectroscopy
TiSapph	Titanium Sapphire
LIPSS	Laser Induced Periodic Surface Structures
SP	Surface Plasmon
LSFL	Low Spatial Frequency LIPSS
HSFL	High Spatial Frequency LIPSS
SEM	Scanning Electron Microscope
2DFT	Two-Dimensional Fourier Transform
NP	Number of Pulses
FDTD	Finite Difference Time Domain
PP	Pump-Probe
PCA	Photoconductive Antenna
IPA	Isopropanol
ND	Neutral Density
LT	Low Temperature
ZnTe	Zinc Telluride
EO	Electro-Optic
SNR	Signal to Noise Ratio

HL HyperLink

FFT Fast Fourier Transform

Si Silicon

FETs Field-Effect Transistors

ICs Integrated Circuits

MBE Molecular-Beam Epitaxy

LSI Large-Scale Integration

TD-ATR Time-Domain Attenuated Total Reflection

LTEM Laser Terahertz Emission Microscopy

QCLs Quantum Cascade Lasers

ICT Information and Communications Technology

UTC-PDs Uni-Traveling-Carrier Photodiodes

HEMTs High-Electron-Mobility Transistors

HBTs Heterojunction Bipolar Transistors

EOS-MLS Earth Observing System Microwave Limb Sounder

ALMA Atacama Large Millimetre Array

OR Optical Rectification

Part I

THEORY

1 FUNDAMENTALS

1.1 THZ RADIATION

1.1.1 *Intro*

The electromagnetic spectrum includes groups of frequencies that are categorized in microwaves, infrared radiation, visible light, ultraviolet light, X-rays and gamma-rays. Higher than the microwave and lower than the infrared frequencies a group called THz radiation exists (Fig. 1.1). The properties of this radiation is defined by its frequency at $1THz$, has a wavelength of $300\mu m$, a period of $1ps$, a photon energy of $4.1meV$, a wave number of $33cm^{\check{}1}$, and a black body temperature of $9.6K$. Terahertz waves have the same abilities as other frequencies, they can create photos by interacting with matter like visible light, create shapes passing through organisms or items like X-rays, and be the carrier of data like microwaves in telecommunications. Every object at room temperature produces black body radiation that is partially in the THz spectrum, thus producing THz. One more naturally occurring source is the background cosmic radiation that reaches the earth, which is also partially in the THz spectrum (Fig. 1.2). The aforementioned sources and many others are incoherent and cannot be exploited. Most of the THz spectrum was not utilized up until recently, because of absence of devices that could produce THz signals in a controlled manner nor devices that could detect and record such signals. That's the reason the part of frequency between microwaves

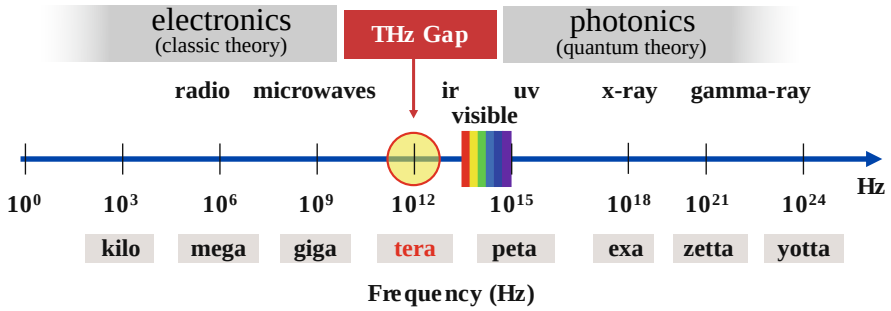

Figure 1.1: THz gap - spectrum

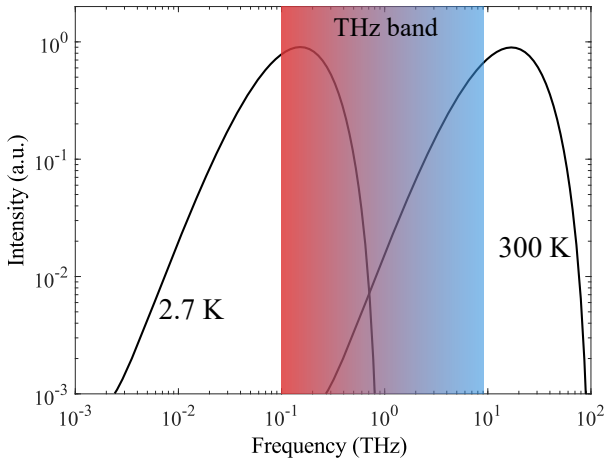

Figure 1.2: Cosmic and Black body radiation in the THz band

and infrared was called the THz gap. The first images generated by frequencies in this gap was in the 1960s and since then focused efforts have been made to fill in the gap. In 1995 those efforts have resulted in the birth of THz-TDS that fueled the interest in the field even more. The broad spectrum of applications that have emerged from the THz research is found in spectroscopy, medicine, microelectronics, agriculture, forensics/security and an expanding list of fields. Maxwell equations express the properties and behaviour of THz in the same way as to all other electromagnetic waves in the spectrum. Although there is a continuum in the electromagnetic spectrum THz are in a transition band of frequencies and they are more difficult to handle compared to its neighbouring frequencies. In scientific research the spectrum with lower frequencies than THz is the field of electronics and the higher side of the spectrum is the field of photonics/optics Fig a.1. As the name of the fields states, the mechanisms to generate radiation from each field are different. In the optics field a photon is produced from an electron during its transition from a higher energy state to a lower energy state, while in the electronics field the photon is produced by the electron while it oscillates in a circuit, Figure a.3. The differences between the two fields are summarized in table a.1. Neither of those fields can be used to approximate the behavior of THz waves. Understanding and utilizing THz waves requires novel techniques and tools to be developed. The drift motion of carriers in general is the source of electric wave generation. In the case of a typical RF device it is not possible to generate radiation with frequencies exceeding a few hundreds of GHz because THz are above the limit that the motion of carriers can oscillate. As mentioned before most of the generated light

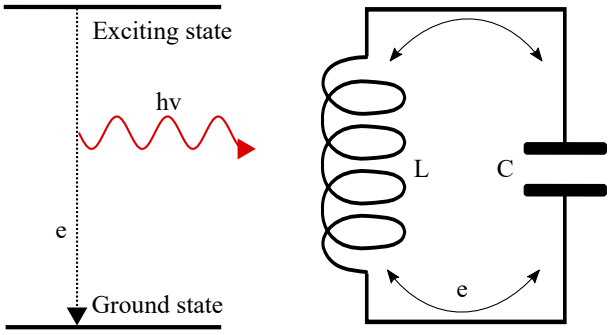

$$\omega = \frac{\Delta E}{\hbar} \qquad \omega = \frac{1}{(LC)^{1/2}}$$

Figure 1.3: Mechanisms in the generation of (a) optical waves and (b) electromagnetic waves

	Electromagnetics	Optics
Name	Electromagnetic waves	Optical waves
Principle	Maxwell equations	Schrodinger equations
Emission	Classical movement	Quantum transition
Measurement	Electric field	Intensity
Tools	Circuit, antenna, waveguide	Lens, mirror, fiber
Approximation	Uniform field	Uniform medium

Table 1.1: Comparing of electromagnetics and optics

comes from the carrier transition between different energy states with few exceptions such as synchrotron, Bremsstrahlung and black-body radiation. If the difference of the states is equal to a photon in the THz range, the energy is low enough that thermal relaxation can make it difficult to distinguish. Incompatibilities with optical and electromagnetic techniques can be found in the mediums and tools used, such as metallic wave-guides for microwave transport and optical fibers for light transport exhibit high losses in THz transport.

1.1.2 *Generation and Detection of THz Waves*

THz waves are mostly generated and detected by the same mechanisms and in the following paragraphs some of them will be presented. A common system in science for generation and detection of pulsed

THz is the Pump-Probe (PP) setup. In general doing a PP measurement requires a laser source that produces a train of pulses with pico to fs pulse duration. The beam is divided into two, pump and probe with the first generating THz while the lateral temporally sampling the THz field intensity creating the pulse profile. For the temporal sampling a mechanical delay line is utilized to create variation in the time of flight between pump and probe. A mechanical or electric modulation of the generated THz through an optical chopper or a function generator on the THz antenna, respectively can increase the sensitivity when the signal is sent to a Lock-in-amplifier. The resulted signal is usually few picoseconds long and can be further processed under Fourier transform to obtain the frequency spectrum of the pulse.

1.1.2.1 *Photoconductive Antenna*

In our experimental setup the generation of THz waves is done by using a photoconductive antenna PCA. It is commonly used for THz setups, both in detection and generation. Upon irradiation of the antenna by ultrafast laser pulses, excited photocarriers are accelerated by an electric field generating a transient photocurrent pulse that emits THz waves. In the following Fig b.1 is demonstrated how a PCA works for a timescale of generating a THz pulse. It consists of two conductive contacts, usually made from metal like gold, spaced apart by few tenths or hundreds of micrometers, sitting on a semi-insulating semiconductor substrate like GaAs, as in our experiment. In the process of generating THz waves a voltage is applied between the contacts without causing electric current flow because the semiconductor is Semi-Insulating (SI). The ultrafast laser pulse is acting as a switch to release the energy stored in the gap between the contacts, as THz radiation. Since the THz photon is emitted with direction perpendicular to the transient current, the polarization of the pulse is parallel the the electric field in the gap. For the carriers to get excited the laser photon energy must be higher than the semiconductor band gap. For photons with energy lower than the band-gap there can be excitation through multiphoton absorption if the laser intensity on the semiconductor surface is high enough. The generated free carriers that are accelerated by the electric field of the applied bias on the electrodes, are not moving all with the same flow rate. Electrons, having higher mobility than holes, are accounted for the total transient current generation while the hole transient current contribution is much lower and can be neglected. The transient photocurrent has temporal variation, producing electromagnetic waves, THz pulses.

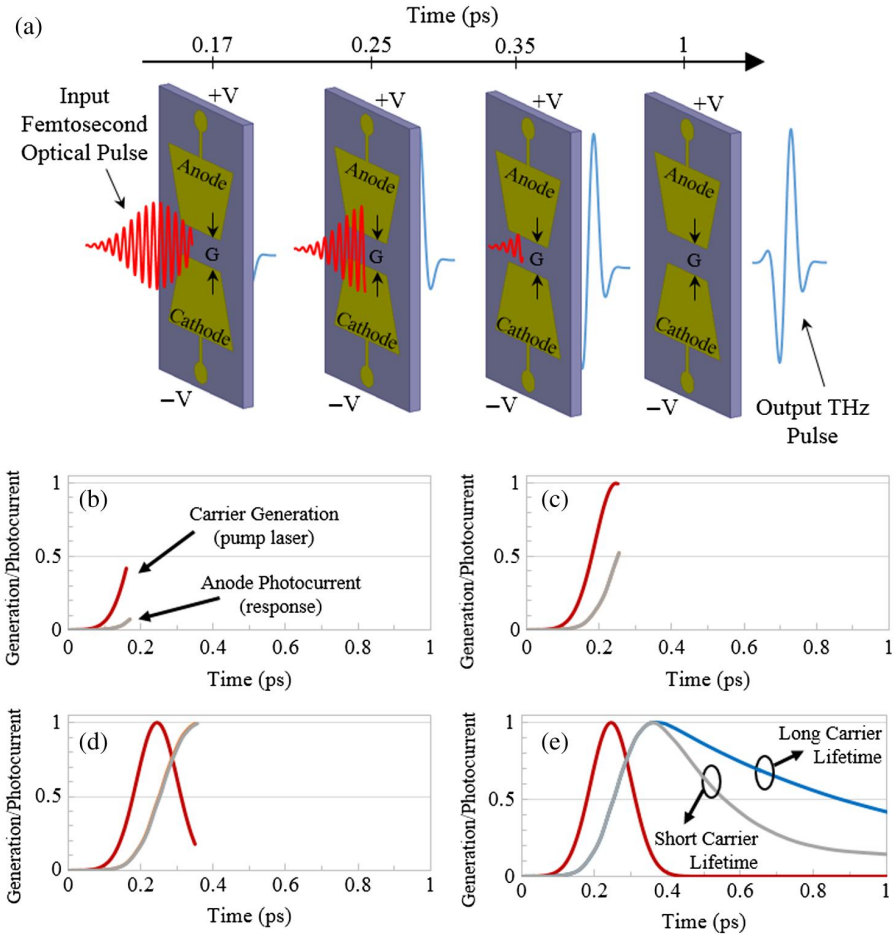

Figure 1.4: Illustrative example of pulsed THz generation in a PCA.(a)Femtosecond optical pulse propagates into the photoconductor, generates a transient photocurrent, which drives the antenna, and is re-emitted as a broadband THz pulse. (b–e) Time profile of the carrier generation (red trace) and photocurrent in the antenna gap for photoconductive material (gray trace) for short-carrier lifetime and (blue trace) for long carrier lifetime.[1]

The optical pulse energy is not responsible for the energy of the energy of the THz pulse but rather from the electric energy stored in the electrode gap. Since the pulse energy of excitation laser is not limiting the pulse energy of THz waves it can be accomplished larger than one in the quantum conversion efficiency of optical to THz radiation. Although, the excitation laser pulse energy has a direct effect on the pulse energy of THz radiation. The stored energy is released when the material is excited, in the form of THz radiation. The emitted THz radiation coming from the stored energy is analogous to the produced photocarrieres and for weak excitations the THz energy is proportional to the energy of the laser pulse. The relation of the external electric field and the THz field is linear, along with the laser pulse energy but only when the applied field is low. As soon as free carriers are generated during excitation the previous semi conductive substrate of the PCA becomes conductive. As a consequence the externally applied electric field is screened by the induced field. In the case of high laser excitation the THz field get saturated. To compensate the saturation, a higher bias could be applied but a threshold of dielectric breakdown of the substrate is a limiting the increase. There are two ways of a PCA can breakdown, thermal and field induced breakdown. The later happens when the bias field exceeds the breakdown limit of the substrate semiconductor, in our case GaAs at $400 kV/cm$. This happens immediately, triggering a field-induced avalanche. Thermal induced breakdown happens when the generated photocurrent increases the temperature of the substrate. The temperature has an inverse relation to the resistivity of the material, that causes further increase in the current flow. Contrary to field induced breakdown, thermal happens in much longer time timescale, of few tens of seconds. Thermal is the most common induced breakdown but field can occur when the gap is small or the bias very high. A PCA besides generating THz waves can be used to detect them, by reconnecting the electrodes from a voltage source to a current detector. In this case the laser pulse excites the material creating free carriers in the substrate. A THz pulse arrives before the electrons and holes recombine, applying an electric field equal to the temporal electric field of the THz pulse, accelerating the electrons towards the electrodes creating a transient current. By changing the temporal delay of the carrier exciting pulse and the THz pulse, a measurement of the intensity of the current at each time will give an equivalent measurement of the temporal profile of the THz electric field.

In Fig.1.5 is presented a typical THz pulse in the time domain. The period is close to $1 ps$ but usually have oscillation duration of under

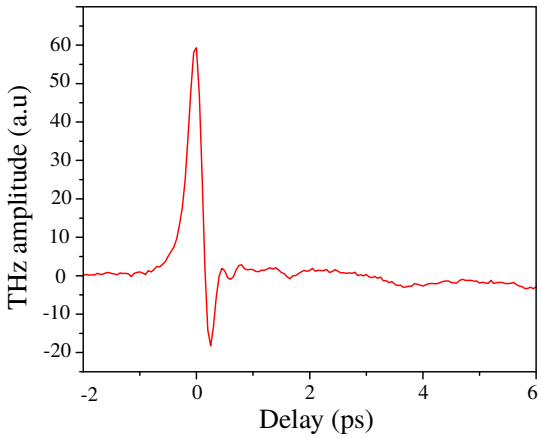

Figure 1.5: Temporal waveform of a THz pulse

one cycle or few cycles. In the measurement of THz pulses it is about the field and not the intensity. Along with the amplitude the phase is also measured, which is challenging in optics measurements. The main parameters that affect the performance of a PCA antenna are the semiconductor used for the substrate, properties of the excitation laser pulse, the geometry of the antenna and the active area. Short carrier lifetime is increasing the response speed of the PCA, therefore materials with such properties are chosen like Low Temperature (LT)-GaAs or doped silicon. In order to detect or generate THz waves with high frequency components, high response speed is required. Increased carrier mobility contributes to more efficient THz pulse generation. Between the electrodes is a gap, where the laser pulse is absorbed and it's the active region of the PCA where THz waves are generated and detected. The field distribution across the gap can be optimized to increase the field breakdown, for higher intensity THz pulse generation [2]. The focal position of the laser pulse can also have an impact of the THz efficiency. Closer to the anode electrode, the slope of the electric field has the highest value causing greater THz wave production [3], but may cause lower breakdown voltage. Using low power laser pulse on smaller gaps, PCA can become more sensitive. On the other hand high power laser pulse on a large gap that accepts higher bias field, can result in higher power THz pulse. By increasing the active area it might increase the screening reaction. Depending the desired frequency response of the antenna the correct shape should be selected. Divided in two groups, antenna shapes are resonant and non-resonant. This shape is defining the coupling of THz waves generated in the substrate and propagation in free space. Resonant antennas are designed to

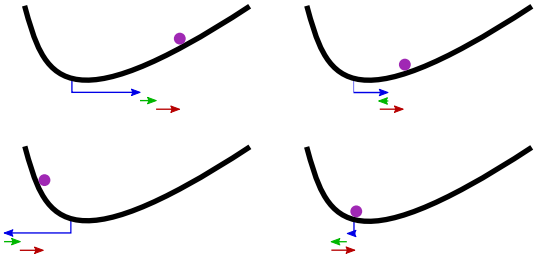

Figure 1.6: An electron (purple) is being pushed side-to-side by a sinusoidally-oscillating force, i.e. the light's electric field. But because the electron is in an anharmonic potential (black curve), the electron motion is not sinusoidal. The three arrows show the Fourier series of the motion: The blue arrow corresponds to ordinary (linear) susceptibility, the green arrow corresponds to second-harmonic generation, and the red arrow corresponds to optical rectification. (When there is no oscillating force, the electron sits at the potential minimum, but when there is an oscillating force, it is, on average, further to the right, by an amount shown by the red arrow.)

generate THz waves of a narrow region of frequencies, mostly shaped in a dipole form. Non-resonant antennas are designed having a width that varies, focusing on producing broadband frequency response. Few of the geometries used for these antennas are bowtie, as the one we are using, logarithmic periodic and spiral. For enhancing the coupling coefficient of THz waves, a silicon hemispheric lens can be mounted on the antenna.

1.1.2.2 *Optical Rectification*

Optical rectification can be intuitively explained in terms of the symmetry properties of the non-linear medium: in the presence of a preferred internal direction, the polarization will not reverse its sign at the same time as the driving field. If the latter is represented by a sinusoidal wave, then an average DC polarization will be generated. Optical rectification can turn a sinusoidal electric field into a DC polarization, but not a DC current. On the other hand, a changing polarization is a kind of current. Therefore, if the incident light is getting more and more intense, optical rectification causes a DC current, while if the light is getting less and less intense, optical rectification causes a DC current in the opposite direction. But again, if the light intensity is constant, optical rectification cannot cause a DC current. When the applied electric field is delivered by a femtosecond-pulse-width laser, the spectral bandwidth associated with such short pulses is very large.

The mixing of different frequency components produces a beating polarization, which results in the emission of electromagnetic waves in the terahertz region. The EOR effect is somewhat similar to a classical electrodynamic emission of radiation by an accelerating/decelerating charge, except that here the charges are in a bound dipole form and the THz generation depends on the second order susceptibility of the nonlinear optical medium. A popular material for generating radiation in the $0.5 - 3THz$ range ($1mm$ wavelength) is Zinc Telluride (ZnTe).

1.1.2.3 *Electro-optical Sampling*

The EO sampling is a method of measuring the THz pulse field by using a crystal. A probe laser beam passes through the crystal with spatiotemporal overlap with a THz pulse. The polarization ellipsoid of the refractive index of the EO crystal is altered by the electric field of the THz pulse, inducing a phase change of the probe beam. As the THz pulse propagates through the EO crystal, birefringence (Fig.1.7) is introduced, which alters the polarization of the probe beam, having a Pockels electro-optic effect Fig.1.8. The beam is split in two new beams, of S and P polarization, by an analyzer, for instance a Wollaston prism. In this way any polarization change is transformed in intensity change for the S and P polarization beams. The main methods used with EO sampling are two, with a balanced detector and the cross measurement.

The balanced detector uses two photodiodes and measures directly the electric field of the THz pulse while giving higher signal. Cross measurement uses a similar setup with the balanced but one photodiode. For our measurements we used a balanced detector Fig.**??**. For this measurement the linearly polarized probe beam, passes through the EO crystal, a zinc blende crystal which is a ZnTe crystal in our measurements, and is altered to elliptical polarization from the EO mechanism. Before entering the analyzer, a quarter-waveplate rotates the polarization of the probe beam. The probe beam is split into S and P polarization components in the analyzer. Intensity of both beams is measured by a pair of balanced photodiodes by measuring the photocurrent produced in the detector. When there is no THz field the photodiodes are set to measure the same intensity for S and P, thus the difference is zero. When the THz pulse acts on the EO crystal, polarization of the probe beam changes so does the the S and P difference on the photodetector. The measured signal is the direct measurement of the THz pulse field.

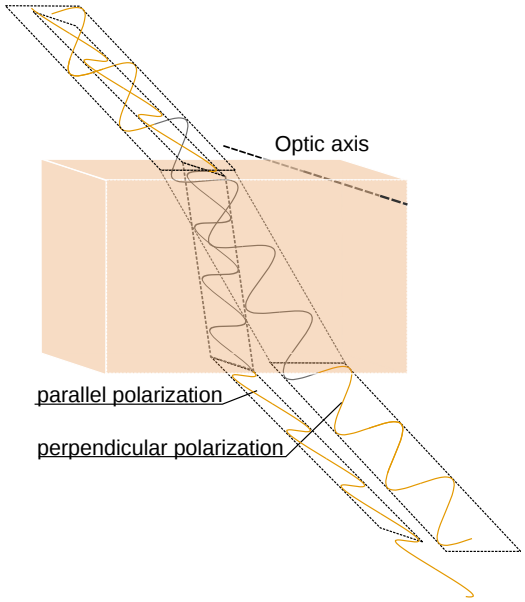

Figure 1.7: In Birefringence incoming light in the parallel (p) polarization sees a different effective index of refraction than light in the perpendicular (s) polarization, and is thus refracted at a different angle.

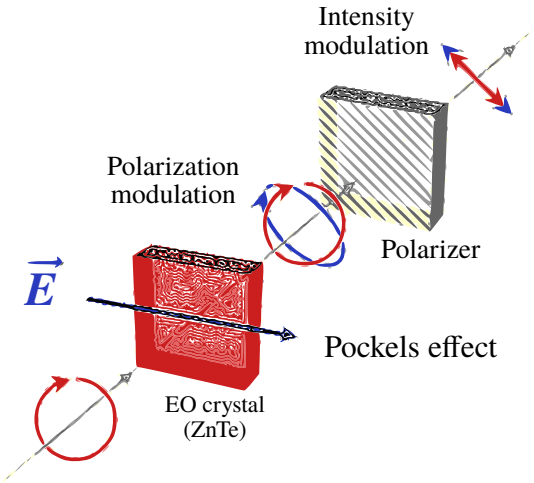

Figure 1.8: Basic elements in EO sampling

In the cross measurement the positions and the elements used are different from the balance method. The polarizer positioned before the EO crystal is set cross to the analyzer and a quarter-waveplate is not used. As the probe beam is biased with a polarization angle perpendicular to the analyzer and the EO crystal doesn't have any effect on it, it is screened on one polarization mode when passing through the analyzer and the measurement is zero on the single photodetector that is on the beam path of this polarization mode (S or P). When the THz pulse is present, the polarization of the probe beam changes, which permits the beam to pass through the analyzer and a signal is measured. This is proportional to the intensity of the THz pulse. In the aforementioned EO measurement it is assumed a constant electric field, but in THz pulses where the electric field is transient a phase matching condition should be applied.

1.1.3 *Spectroscopy*

Few decades of research and development have passed since the first THz antennas and detectors appeared. While they are still in an early stage, when they become affordable and available for wider use scientists will seek for new applications . Currently the applications are grouped in two main categories, THz spectroscopy and imaging. Since this research is focused on the primary we are not going to advance the lateral but focus in spectroscopy. In the following section we are going to discuss about the technique that is mainly employed in THz wave spectroscopy and that is the THz-TDS technique.

1.1.3.1 *THz Time-Domain Spectroscopy*

In a system that produces pulsed THz waves a pulsed laser probe beam is used to sample the THz waveform. An oscillator laser source is producing a train of pulses and this beam is split in two sub beams, the pump and the probe. The former has usually higher power and is used to generate THz waves while the later, with lower power is used for detecting and measuring the THz pulse. They have similar temporal waveform due to the same origin. The probe beam travels through a delay line, that varies the time of arrival on the THz detector between the two pulses, making it possible to record the electric field as a function of time. From the time domain $E(t)$ we can switch to

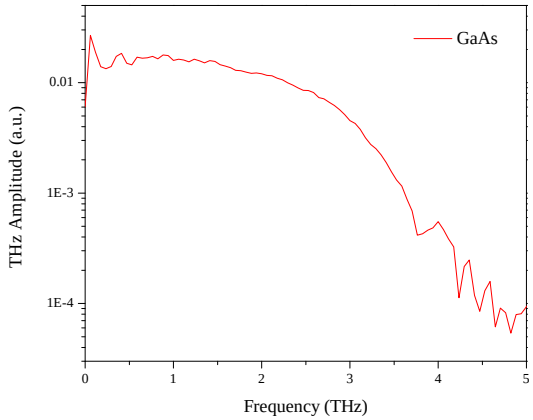

Figure 1.9: Basic elements in EO sampling

the frequency domain $E(\omega)$ through the Fourier transform, which provides access to the spectral properties of the THz waves.

$$\tilde{E}(\omega) \equiv A(\omega)e^{-i\phi(\omega)} = \int dt E(t)e^{-i\omega t} \tag{1.1}$$

The products of the Fourier transform is the THz field with a complex value, of amplitude and phase. The bandwidth varies from 0.1 THz to above 100 THz, which is the defined THz range and is dependent on the source of generation. We can obtain the frequency response of a material for a bandwidth range defined by the THz pulse, after measuring the waveform of the pulse and converting it to the spectrum through Eq.1.1. Considering that the measurements are taken in different time steps, it is expected that the given name of this technique is Time Domain Spectroscopy (TDS). After the Fourier transform to the frequency domain, the spectral response of the THz generating antenna is shown in Fig.1.9.

The delay temporal scanning range ΔT defines the spectral resolution $\delta\omega$ while the temporal scanning step size δt defines the spectral bandwidth $\Delta\Omega$ of the THz-TDS. The spectral values are explained by

$$\begin{aligned} \delta\omega &= \frac{2\pi}{T} \\ \Delta\Omega &= \frac{2\pi}{\delta t} \end{aligned} \tag{1.2}$$

A mathematical technique called zero padding is used in Fast Fourier Transform (FFT), in order to increase the smoothness of the

THz spectrum. In this method a large number of zeros is added to the end (or both sides) of the waveform of the THz pulse, therefore increasing the temporal scanning range and increasing the intensity of the data points. Since the added zeros do not provide any additional information the resulted spectral resolution is the same. In order to study the spectral response of a sample, the response of free space should be measured initially, which is the THz waveform without the sample. This is the reference waveform, while the waveform captured when THz interacts with the sample is the signal waveform and by applying FFT on those, we receive the reference and signal spectrum respectively. The real sample spectral response is given by the difference of the two signals. Both phase and amplitude of the electric field of the THz pulse are measured using this technique, which enables to acquire the absorption and refraction of the sample.

Some benefits of using THz-TDS is that it has coherent spectroscopic detection for a broad range of THz, that is difficult to acquire with other techniques. Due to the short duration of the THz pulse, on the *ps* scale, it gives access to high temporal resolution. Because a Lock-In amplifier is used it has high Signal to Noise Ratio (SNR).

Some of the drawbacks of the current technology THz-TDS are the slow measurements, because temporal sampling the THz wave requires some time for every stem of the delay line. Also the relatively short length of the delay line is limiting the temporal scanning range which is limiting the spectral resolution. Although we could increase the scanning range it would substantially increase the time required to complete the measurement. In a typical THz-TDS measurement the spectral bandwidth varies from 0.1 to 5 THz but can be increased up to 100 THz, by using much shorter laser excitation pulses and decreasing the thickness of the substrate of the THz generation or detection EO crystal. For a broad bandwidth THz-TDS measurement the dynamic range will be limited.

1.1.4 *Applications*

There are two main branches that THz applications are been separated: in communications and sensing. An advanced scientific technique to analyze a large variety of materials are THz-TDS and Frequency-Domain Spectroscopy (FDS). There is a broad field of applications of THz technology in telecommunications and information technology, including space communications, wireless communications and high-speed data processing. Furthermore THz sensing devices have

been developed providing exceptional efficiency in numerous research fields some of which are material science, physics, medical science, biology, medication evaluation, astronomy, environmental monitoring, body scan security and industrial non-intrusive defect detection. Plenty of cases can be found [4–6] in all areas of study: explosive analysis, carcinoma diagnosis, DNA microprocessors, Large-Scale Integration (LSI) microchip inspection and plenty more. An abundance of applications can be developed from the combination of the above research fields. For example, the use of a THz detector, large analyzer networks and selective communication to materialize recognition techniques established on physical and behavioural human features, in biometrics.

1.1.4.1 *Biological, medical and pharmaceutical sciences*

Numerous materials have been studied by THz-TDS since its invention, in the beginning of 90s [7–10], some of them are cancer cells, DNA, pharmaceutical-drugs, biomolecules, bacteria and proteins. Something that needs often clarification is the difference between the way information is given in THz spectroscopy and in infrared spectroscopy. The spatial scale of those measurements has few orders of magnitude difference, thus in infrared spectroscopy owning smaller wavelength is used to measure intramolecular mode vibrations, while THz spectroscopy owning larger wavelength has the ability to measure intermolecular vibrations of certain organic molecules and chemicals [11]. Extended research on intermolecular modes will probably explain in detail the greater bio-molecule dynamics, leading to better understanding of the processes in living organisms. Classification of polymorphs in pharmaceutics is an additional application [12]. Under heat processing a structure modification is observed in barbital (an ahypnotic drug),which can be seen in the THz absorption spectrum as shown in Fig. 1.10. In the Fourier-transform far infrared spectroscopy (FT-FIR) area any differences are barely visible, contrary to the TDS area where the differences are well defined. It is of great significance, employing research on different type of cancers, proteins, DNA and more biomolecules. Functional applications are expected to encounter challenges for the time being, albeit the disparity of denatured from hybridized DNA that has been published, which can lead in exploration of building label free DNA microchips. Research is done on the aforementioned and similar biomolecules. THz imaging and spectroscopy have been utilized in various research cases for the detection of cancer [5]. Since the energy of THz waves falls to the

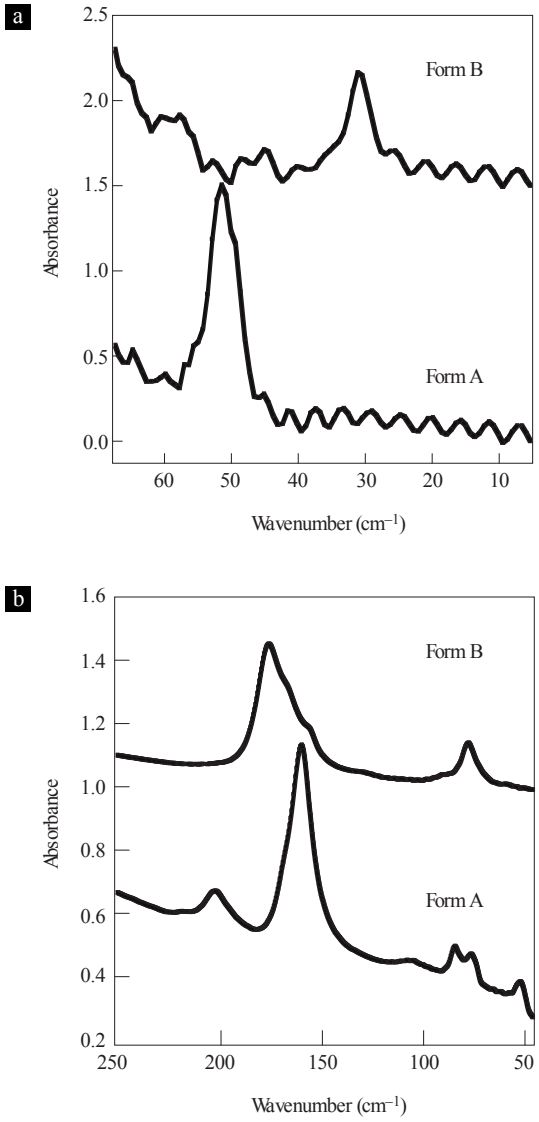

Figure 1.10: THz-absorption spectra of barbital. a, THz-TDS. b, FT-FIR. The polymorph sample (form B) was obtained by heating original barbital (form A)at 160°C for 30*minutes*. As seen in [13]

region of various molecular vibrations it is expected that they will be absorbed, with higher efficiency in polar molecules, like water. Cancer cells have other hydration concentrations than normal tissue cells and this difference produces unexpected reflections in the measurement, making them visible. The spatial resolution for this measurement is $40\mu m$ and $350\mu m$ for the depth and the surface plane respectively, with the ability to measure a depth of up to $1mm$ from the surface of the skin. Identification of cancer cells is possible inside frozen tissue, considering that ice has a THz transmission exceeding that of liquid or vapor water. Similarly to water that is able to absorb THz waves efficiently, other liquids with polar properties make it complicated to make THz measurements of bio-materials that have been dissolved in such liquids. Time-Domain Attenuated Total Reflection (TD-ATR) spectroscopy which was invented and demonstrated is a great advance in the field [14]. In this technique the THz waves are traversing through a Dove prism, exciting an evanescent field on the surface of the prism. The field will be affected by a presence of a sample on the surface of the prism and the measured TDS signal between having or not a sample, will provide a measurable phase and reflectivity difference. This will allow the investigation of molecules dissolved in liquids and their dynamics in accordance to various characteristics, like hydration dependence [15]. In a comparison of relaxation times the surface of biomolecules will bind with hydrated molecules for up to $10^{\tilde{}}7s$ while this time will be much longer in many picoseconds between bulk water and hydrated molecules. The solvation number can be considered by measuring the dielectric constant at the spectral range of THz waves, which can be demonstrated by the use of TD-ATR making it an important asset in the field of biomedical studies.

1.1.4.2 *Semiconductor and other industrial applications*

A great amount of studies has been performed on identifying material properties [16–19], that can be exploited for novel industrial applications, as for example examination of photovoltaic panels, dielectric/polymer films and nanocomposite. Further advances with THz techniques on semiconductor applications will promote the THz employment. Previous works on measuring different properties of semiconductor wafers, in particular carrier density, conductivity, plasma oscillations and mobility, with the use THz-TDS have been performed [20, 21].

A powerful characteristic is the capability of imaging. For instance, the degree of doping of ion-implanted wafers can be imaged. In

LSI microchip fabrication, a defect detection mechanism would be of utmost importance for advancing in next-generation devices. A potential method in evaluating the position of a defect spot and a great advance in technology would be Laser Terahertz Emission Microscopy (LTEM). The space shuttle insulation material was examined, with the use of THz imaging which was the superior choice for its non-intrusive measurements on the sample. In this study the results showed that the method has the ability to identify weakness points in the thermal-insulating plates, like structural gaps [22], and since has been standardized as the default inspection process. The characteristic property of water, being opaque in the THz waves, can be exploited in agriculture and food industry, for detecting spoiled food and tracking hydration levels in fresh products.

1.1.4.3 *Security*

Each material has a characteristic response to certain frequencies. Those frequencies fall in the THz region for narcotics and explosives enabling THz spectroscopy to be used in security and threat detection. Each characteristic signature found in the measured spectrum determines the presence of a chemical compound in the sample. Certainly explosives and illegal drugs can be identified and separated from harmless mixtures. Paper material in envelopes is transparent to frequencies lower than $3.0THz$ making it possible to "look" inside the mail without opening the envelope, by acquiring THz multispectral images and and component spatial-pattern analysis [22] (Fig. 1.11a). Another THz real time imaging mechanism is available from the use of Quantum Cascade Lasers (QCLs). Fingerprint imaging is displayed in Fig. 1.11b using a polyethylene wedge, owning ripple spatial periodicity of approximately $500\mu m$ from peak to peak. The same method could be applied for reading a note that is inside a paper cover. Extended studies in real-time monitoring are available in reference [23]. It has been of unprecedented technological significance the creation of a THz camera with focal-plane array. Samples could be imaged inside smoke and fog, independent of the background illumination, by the use of such camera. Applications in airport security has already been used by incorporating a heterodyne detection method with an SBD array with a silicon photonic-bandgap crystal, running at $0.5THz$, forming a passive THz camera. Bio-metrics could also be measured by utilizing an active THz camera that could be used in additional applications. Although there is a large range of applications that could use THz, there are few security applications that need detection from

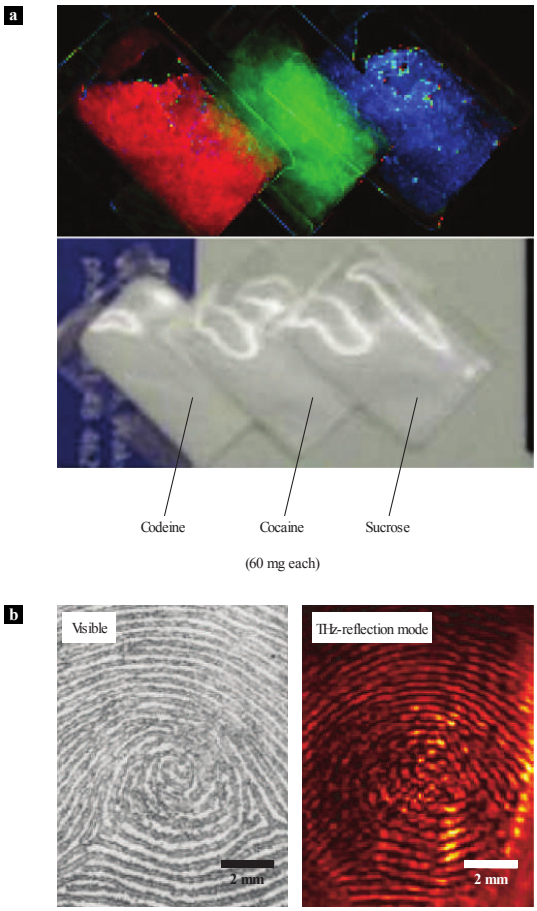

Figure 1.11: Terahertz narcotic detection a) THz image (upper) and photograph (lower) of specimens under inspection. Codeine, cocaine and sucrose are hidden in the envelope and can be identified using THz-TDS by their own THz signatures. Image courtesy of Kodo Kawase, RIKEN. b) Visible frequency thumb print and real-time THz reflection mode image of the print. The real-time THz images can be obtained by a $4.3THz$ and a 320×240 microbolometer focal-plane array at an acquisition rate of 20-frames per second. As seen in [13]

far away and due to the high absorption of THz by water, the signal is significantly attenuated, by traveling in air due to the presence of water molecules. A newly presented technique used air plasma for remote-controlled THz excitation. Next to the sample a high power femtosecond laser beam is focused, producing ambient plasma, which in turn excite THz pulses and like in the THz-TDS method, it detects the reflection of the sample [22]. THz sensing, utilized for identifying dangerous gases is predicted of getting more popular. An example is an application in fire sites with concrete walls where the already used IR gas detection methods are unable to penetrate the walls while in contrary THz could potentially perform such task.

1.1.4.4 *Information and communication technology*

THz applications have the capacity to progress in the Information and Communications Technology (ICT) market. The need for faster connections with greater data bandwidth has been in continuous growth in the last years. Along with the bandwidth, the carrier frequency of connections has been increasing as the the change dependency between them is analogous. In comparison the wired communications have been advanced from copper to fiber mediums, increasing the bandwidth many folds, but in contrary the wireless communications have been relatively static to using microwave frequencies. A step forward, towards THz-ICT could increase the speeds and bandwidth of one or two fold, matching speeds of single fibers and providing access to higher efficiency telecommunication applications. Some examples are high speed public access points in urban areas, telemedicine ultra high definition streaming connections, high bandwidth video transmission in motor-sports and other sports and the ability to cover the data rate demand with less transmission hardware. A step towards accomplishing such devices is done with the use of Uni-Traveling-Carrier Photodiodes (UTC-PDs) being able to generate waves with spectral response on the sub-THz region. An experimental setup has been demonstrated, with capabilities of over $10 Gbit/s$, operating at the frequency of $120 GHz$ (ref. [24]), offering speeds equal to transferring a ordinary sized movie in few seconds. It is expected that in the upcoming years the bandwidth will reach $40 Gbit/s$, effectively doubling the current maximum carrier frequency. With increasing attenuation at higher frequencies the technology will be limited to indoor, short range wireless connections. Quick advances are happening in THz-ICT essential components. An $8-bit$ shift register has been demonstrated by integrated single flux quantum circuits, with a cycle of $120 GHz$ (ref. [24]). At a higher frequency of $1 THz$, quantum wells made of coupled InGaAs–AlAs–AlAsSb perform all-optical switching (ref. [24]). While other accepted techniques are in development utilizing Heterojunction Bipolar Transistors (HBTs) and High-Electron-Mobility Transistors (HEMTs) [24]. This region is lacking essential components, needed for the THz advancement, such as, waveguides, modulators and mirrors. Although the later two have seen some progress by combining high-resistivity silicon with polypropylene to create omnidirectional mirrors and efforts in THz modulation [25]. Sensing applications and ICT can be equally benefited by the advances in transport of THz waves. Attempts for creating THz waveguides have been performed, using poly-carbonates and plastic fibres. Trans-

porting THz waves with low attenuation and nearly no dispersion was demonstrated on the surface of plain metal [25], which can be described, using the analogy of a propagating electromagnetic wave across the surface of a cylindrical conductor, as seen in Sommerfeld's research. This could enable the fabrication of beam splitters. A study has proven that cylindrical-wire waveguides could have a better coupling coefficient of THz pulses by the use of specific radially symmetric photoconductive antennas[25].

1.1.4.5 *Earth and space science*

Various approaches have been made to protect the Earth and one tool that could assist the monitoring of the environment could be THz technology. A NASA's satellite orbiting around the Earth since 2004 carries the Earth Observing System Microwave Limb Sounder (EOS-MLS). It is capable of taking a variety of measurements, like temperature, presence of ice, clouds and many different atmospheric chemical compounds [25]. The frequencies a heterodyne radiometer operates are between $118GHz$ and $2.5THz$, in order to evaluate the thermal emission. It is designed to examine situations of pollution in the upper troposphere, measure how the climate is influenced from the atmospheric composition and comprehend parameters of global warming by collecting data on the ozone composition. Sitting atop of the Atacama desert in south America, at an altitude of $5km$ the international astronomy center, Atacama Large Millimetre Array (ALMA) is being build. The extraordinary feature of this facility are the combined antennas of great accuracy, accounting 80 pieces in total with 64 of them having $12m$ diameter, that perform as a one antenna of extreme accuracy with a hypothetical diameter of $14km$. Its effective frequency range will be of $30 - 950GHz$ in sensing electromagnetic waves that pass through the atmosphere. The multipurpose of measuring those frequencies lies in the information they can reveal on the yet unknown cosmos, from the genesis of new stars, solar systems and galaxies to alien life form molecules. Another satellite orbiting the Earth since 2006 is AKARI and is a tool for infrared astronomical observations (refs [26, 27]). Its objective is the study of solar systems and evolution of galaxies. Data is captured by two detectors that cover a wavelength range, one camera in the IR from 1.7 to $14.1\mu m$ and the other in the far-IR, overlapping with the THz region from 50 to $180\mu m$, ref. [28].

1.1.4.6 *Basic science*

The characteristic energy of THz, few to many meV, falls in the region of low energy carrier dynamics of many materials, with one of them being superconductors, which can be accessed by combining THz spectroscopy with optical index analysis [29]. When photoexcited carriers in an electronic material undergo ultrafast modulation, THz pulses are generated, that can be examined to extract spectroscopic information. Using this method, THz emission spectroscopy, studies on several materials has been performed, like ferromagnetics, manganites and some superconductors [30–33]. Through those studies, it is visible that material characterization is one important field of THz-TDS. The high temporal resolution remains one of the most important advantages of THz-TDS, with values as low as the pulse duration of the laser source, that can usually reach $10fs$, enabling measurements of electron dynamics in a semiconductor [34]. Additionally with the use of pump/probe THz-TDS on a photo-excited semiconductor, the temporal evolution of the dielectric function can be obtained. An example is, an accumulated growth of electron-hole plasma in solids, lasting for $100fs$, that is exposed by a variation in the dielectric value. Potential applications of these techniques could include transient quantum physics, dynamic analysis of molecular reactions in biochemistry and othe ultrafast studies. The nature of light could potentially be investigated by using THz pulses. Some of the research on this field presents results of group-velocity anomaly, propagation in random media and multiple diffraction of light [35, 36]. Meta-materials with operating frequency in the THz region have been fabricated, attracting interest [37–39]. In semiconductors the cyclotron resonance can be investigated spectroscopically with the use of THz-QCLs [40]. Although THz research has few years of development, a lot of progress has been demonstrated already and the future prospects have excited the scientific community of the applications and advances to come.

1.2 LIGHT MATTER INTERACTION

Even in the beginning of lasers, it had been seen that the concentrated light energy could influence the illuminated material significantly: Damage to optical materials happened as a result of evaporation and extraction of material from the target surface. During the first observation of laser ablation, material was removed from a target upon laser irradiation. Quickly,this observation was used for material

processing in a more controlled way, e.g. in cutting without machinery, which became the most common used method in the industry today. Most of the early research and applications were performed utilizing CO_2 lasers, and comprehended regarding the classic thermodynamic processes, the laser being thought as source of high density heat. Around thirty years prior, UV-laser removal from natural polymers [1] was observed and it was proposed that laser ablation might be more complicated than had been thought up to that point, including quick melting and vaporization as well as electronic transitions. For the next years, the ablation using lasers started to draw attention in both applications but scientific study as well [2].Energy transfer when the applied energy on a target overcomes the solid's binding energy, the result is decomposition or material removal from the solid target. During a slow process of energy transfer to the material, that follows thermodynamic equilibrium, the energy input ΔE has a complete transform to temperature increase ΔT:

$$\Delta E = cm\Delta T \tag{1.3}$$

(c and m are heat capacity and mass of the irradiated material respectively). As can be seen in Fig. 1.12, a classical phase transition can be induced by internal energy increase and seldom part of the heated volume to get detached. Looking on an atomic scale, increase in temperature is defined by increase of kinetic energy of atoms. Energy input from classical heating where the atomic kinetic energy comes from momentum transfer, as in phonon bath and ion impact, is very different from laser heating: the laser photons interact with the electrons of the solid, while any other motion related to the nucleus of the atom is a process that follows. The processes are happening in a chronological order, beginning with photon absorption, followed by material extraction and lastly target relaxation. Since the timescale of material modification (removal or transient band-structure changes) happens after $150fs$ a shorter pulse can interact with an almost passive target, providing access to material properties unaffected by absorption. Longer pulses will interact with the ablation process and partially absorbed by the produced plasma plume.

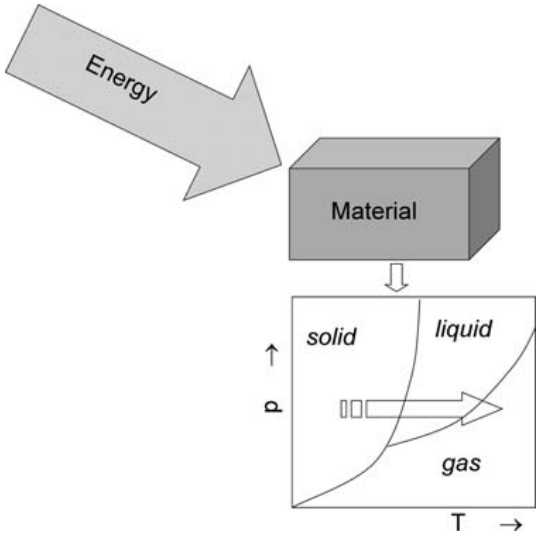

Figure 1.12: Energy input in material and phase transition.[41]

1.2.1 *Ion Emission: Ablation*

1.2.1.1 *Coulomb Explosion*

A large amount of electrons are emitted when a laser irradiates a target. It is estimated that this happens as soon as the laser pulse arrives, at a short depth of the surface leaving positive holes behind. The electrons from the bulk region, take about a picosecond to fill the holes, for semiconductors [14,15] or dielectrics. For this amount of time the surface area will stay positively charged. Under high irradiation, a high hole density will be generated in this area, causing electrostatic instability, leading to surface breaking apart and emission of positive particles. This phenomenon where the Coulomb force leads to massive electrostatic repulsion of charged particles on the surface of the irradiated material is called Coulomb explosion [16-18]. An electron bath could be generated after higher excitation is applied and the hot carrier absorption becomes significant. Through electron-phonon collisions the electron bath will quickly couple to the lattice, increasing the temperature of the bulk.

1.2.1.2 *Self-Organized Structure Formation and Transient Instability*

Periodic Ripples

During the study of the surface of the substrate after many ablation pulses, we observe a heavily altered morphology. Periodic parallel wavelike formations have appeared, having wavelength below the

excitation laser wavelength. Structures like these were first seen in the early 70s [28,29], on targets that have been irradiated with nanosecond laser pulses, named "ripples". This was explained with a model attributing the result to a modulated energy input, till the middle of 80s, that was credited to the interference of the surface scattered electromagnetic waves with the incident waves [30]. This model is not compatible with features on structures generated after irradiation with femtosecond pulses. Such structures include finer ripples with much shorter wavelengths than of the excitation laser, bifurcations and truncations and are not possible to be explained by plain interference structures. Rather, self-organization from instability produces interference structures that are visually comparable. In order to create a fitting model for self-organized structure formation it should be taken into account the principles of nonlinear dynamics, that have already been early approaches to design such models [6,32].

Polarization Dependence

The image we have on the ripple formation through self-organization looks to be coherent, a specific property of this phenomenon remains unexplained. Throughout the experiments it was observed a strong relation between the polarization of excitation laser and the orientation of the formed ripples. Also the type of polarization defines the shape of the structures, linear produces straight ripples perpendicular to the electric field of the laser, circular produces cones with a round base while elliptic polarization is a combination between the two. It is observed that the ripple direction is independent of the materials crystal structure and follows the rotation of the polarization, when rotated in respect to the target surface [5,32]. During this process the last polarization angle defines the orientation of the ripple formation. A surprising effect is the observed coherent continuity in the ripple formation, under repetitive slightly overlapping laser pulses [41].

1.2.1.3 *Overview*

A logical order in the formation of nanostructures under femtosecond laser irradiation, starts with a short duration laser pulse with high energy density, that perturbs the electronic structure of the material, initiating an instability phase which causes ablation/desorption. The surface is getting rougher from the particle emission, leading to further instability. At the same time the surface tension from the melted material is opposed to roughness, by smoothing the surface and further promoting instability. The time scale of this process is incredibly short, along a great order-gradient to the non-irradiated surrounding

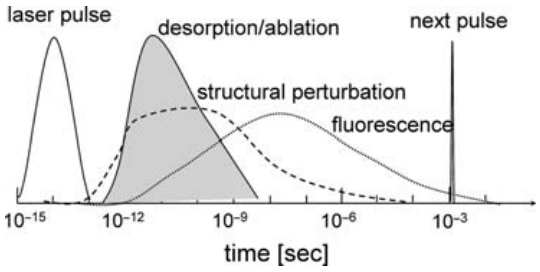

Figure 1.13: Time line of excitation processes: after the arrival of the laser pulse the ablation begins and almost at the same time the structural perturbation sets in [26,27,35–37]. (as seen in [42])

material, that demands extremely quick relaxation, in contrast to the much slower equilibrium progress. Thus leading to self-organized structure formation. Under a linear polarized laser source, the ripple orientation sets perpendicular to the laser electric field. After thoughtful examination of this hypothesis an inconsistency is exposed (see Fig. 1.13): the laser polarization effect is on a very different time scale that the structure formation. The process of structural perturbation starts after the the pulse has already been absorbed, thus the motion of atoms at the surface should not be affected by the electric field of the pulse. Since the approach of "polarization memory", lacks evidence for a complete explanation, it remains open. A suggested theory identifies surface plasmons excited by the incident pulse, which have a comparable lifetime as the nanostructure formation time scale and are oriented from the electric field. During the self-organized relaxation process the atom diffusion direction is assisted from surface plasmon.

1.3 SEMICONDUCTORS AND THE BAND-GAP

Metals, semiconductors and semimetals have different carrier concentrations which are given in Fig. 1.14. The electrical resistivity of semiconductors heavily depends on temperature and can range from 10^{-2} to $10^{9} ohm - cm$ at room temperature values. When temperature reaches $0K$ in a semiconductor and it has a perfect crystal lattice the resistivity will reach values above $10^{14} ohm - cm$, it will make a transition from semiconductor to insulator. Semiconductors are used for various devices such as diodes, photo-detectors, transistors, photovoltaic cells and switches. For their implementation, they can be installed as individual components in a circuit or as integrated circuit parts. Using a molecular notation AB, with A and B the trivalent and prevalent element respectfully, we describe semiconductor compounds

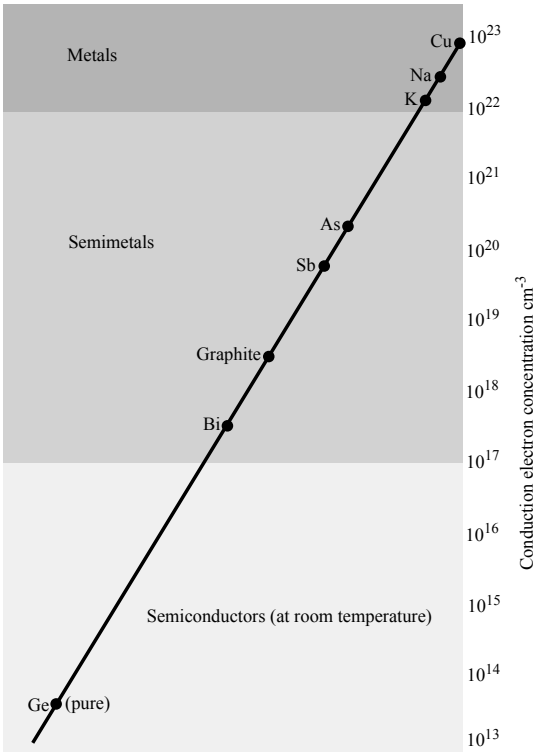

Figure 1.14: Carrier concentrations for metals, semimetals, and semiconductors. The semiconductor range may be extended upward by increasing the impurity concentration, and the range can be extended downward to merge eventually with the insulator range. As seen in [41]

as "three-five" (III-V) compounds. Prime examples are the Gallium Arsenide and the Indium Antimonide. In the case where A and B are divalent and hexavalent respectively they are named two-six (II-VI) compounds. Such semiconductors are Magnesium Oxide and Zinc Oxide. While there are semiconductors with diamond cubic crystal structure, like Germanium and Silicon, diamond by its nature is an insulator. Lastly there are the four-four (IV-IV) semiconductor compounds like Silicon Carbide. An intrinsic conductivity is observed in a semiconductor with increased purity, in contrast to the impurity conductivity in semiconductors with lower purity. Impurities in the crystal do not substantially alter the electrical properties of the semiconductor at the intrinsic temperature range. For temperature at $0K$ the valence band is filled in contrast to the conduction band that remains empty and the energy difference between the lowest and highest point in conduction and valence band respectively, is defined as the energy band gap E_g. The energy point where the bands stop, is

the edge of each band, highest point for valence and lowest point of conduction. Electrons from the valence band are thermally excited to the conduction band, during temperature rise. The generated holes in the valence band and the free electrons in the conduction band, are responsible for the resulting electrical conductivity.

1.3.1 *Band-gap*

The band gap to temperature ratio E_g/k_BT, is strongly affecting the intrinsic carrier concentrations and intrinsic conductivity. In reverse proportion are the ratio with the conductivity and the concentration of intrinsic carriers, with the increase of the first causing lowering in the two that follow. Optical absorption can be used to access the ideal values of the band gap. With frequency ω_g and using a direct absorption process, the band gap $E_g = \hbar\omega_g$ is measured by the threshold of continuous optical absorption as shown in Fig. 1.15a. An electron-hole pair is generated while a photon excites the crystal. In the case of Fig. 1.15b the absorption is indirect and for the electron and the hole in the position of minimum band gap energy, they are apart by a wavevector k_c. For the energy range of interest the photon wave vectors are insignificant, thus the condition of conservation of wavevector cannot be fulfilled by a direct photon transition at the energy of the minimum gap. Although if there is a creation of a phonon with wavevector K and frequency Ω, the following equation becomes true

$$\begin{aligned} k(photon) = k_c + K \cong 0; \\ \hbar\omega = E_g + \hbar\Omega \end{aligned} \tag{1.4}$$

Significantly smaller from E_g will be the phonon energy $\hbar\Omega$. In relation to the energy band gap the phonon energy is much smaller, typically in the range of ~ 0.01 to $0.03eV$ thus making easily the excitation of even a high wavevector phonon from the crystal momentum. During a photon absorption process a phonon could be absorbed simultaneously if the temperature of the crystal is raised sufficiently so the phonon has reached thermal excitation. Using the carrier concentration at the intrinsic range or temperature dependence of conductivity it is possible to extract the band gap. From Hall voltage, the carrier concentration can be deducted which can be complimented by measuring conductivity as well. In order to characterize if the band gap is direct or indirect an optical measurement is used. For semiconductors like Silicon and Germanium the band edges have an indirect transition. In contrary other semiconductors have a direct transition like Gallium

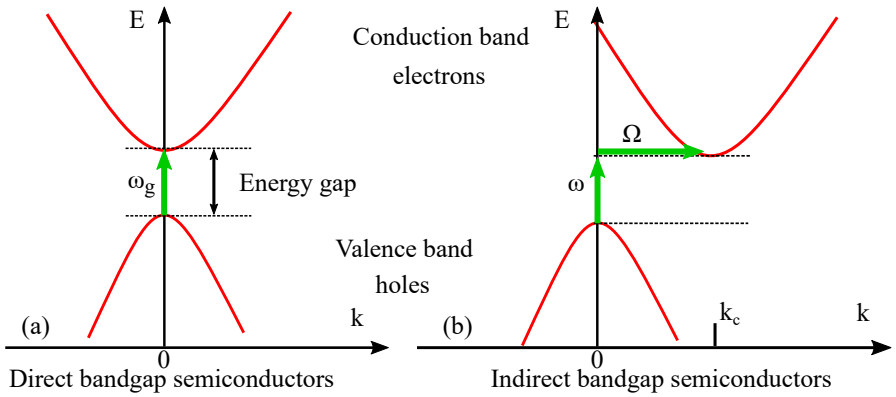

Figure 1.15: In (a) the lowest point of the conduction band occurs at the same value of k as the highest point of the valence band. A direct optical transition is drawn vertically with no significant change of k, because the absorbed photon has a very small wavevector. The threshold frequency ω_g for absorption by the direct transition determines the energy gap $E_g = \hbar\omega_g$. The indirect transition in (b) involves both a photon and a phonon because the band edges of the conduction and valence bands are widely separated in k space. The threshold energy for the indirect process in (b) is greater than the true band gap. The absorption threshold for the indirect transition between the band edges is at $\hbar\omega = E_g - \hbar\Omega$, where Ω is the frequency of an emitted phonon of wavevector $K \cong -k_g$. At higher temperatures phonons are already present; if a phonon is absorbed along with a photon, the threshold energy is $\hbar\omega = E_g - \hbar\Omega$. Note: The figure shows only the threshold transitions. Transitions occur generally between almost all points of the two bands for which the wave vectors and energy can be conserved. As seen in [41]

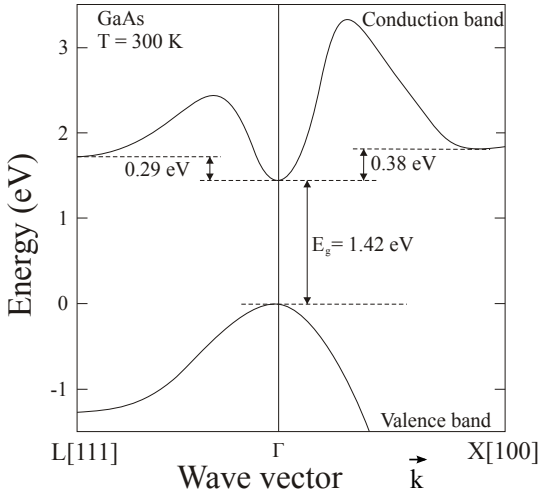

Figure 1.16: The direct band-gap of GaAs

Arsenide and Indium Antimonide. A direct band with zero value is owned by αSn. Lastly when the band gaps overlap their values become negative and are characterized as semimetals such as Mercury Selenide and Mercury Telluride.

1.3.2 *GaAs*

The choice of material and the femtosecond pulse duration are two factors that define the conversion efficiency and frequency response in THz generation with photoconductive antennas. The generated THz wave that travels into free space is in analogy with the second derivative of the photo-induced transient current in the semiconductor. The applied electric bias on the electrodes, the laser ablation pulse duration and the material intrinsic carrier rise time are responsible for the rise time of the transient current. The choice of the semiconducting material should be made so the laser ablation photon energy is sufficient to excite an electron from the valence to the conduction band, thus the photon energy is larger than the energy band-gap. A common laser source for THz-TDS experiments is a Titanium Sapphire (TiSapph) laser, with photon energy of $1.55eV$ and a semiconductor that fits these requirements is GaAs, with energy band-gap of $1.42eV$. This is a great semiconductor for high-efficiency photoconductive antennas because of its high electron mobility and quick carrier rise time.

GaAs is a semiconductor compound used in diodes, Field-Effect Transistors (FETs), and Integrated Circuits (ICs). The charge carriers, which are mostly electrons, move at high speed among the atoms.

Material	$d_{eff}\,(pmV^{-1})$	n^{g}_{800nm}	n_{THz}	$\alpha_{THz}\,(cm^{-1})$	$FOM(pm^2cm^2V^{-2})$
CdTe	81.8		3.24	4.8	11.0
GaAs	65.6	4.18	3.59	0.5	4.21
GaP	24.8	3.67	3.34	0.2	0.72
ZnTe	68.5	3.13	3.17	1.3	7.27
GaSe	28.0	3.13	3.27	0.5	1.18
sLiNbO	168	2.25	4.96	17	18.2

Table 1.2: Properties of a few materials suitable for OR. With the d_{eff} the effective nonlinear coefficient, n^{gr}_{800nm} the index at $800nm$, The THz index n_{THz} and absorption coefficient α_{THz} are given for $1THz$ and FOM. All values are for room temperature.[43]

This makes GaAs components useful at ultra-high radio frequencies, and in fast electronic switching applications. GaAs devices generate less noise than most other types of semiconductor components. This is important in weak-signal amplification.

A common material for detectors and emitters is LT-grown GaAs. The name identifies the low temperature ($\sim 200^{\circ}C$) conditions during the GaAs growth in the Molecular-Beam Epitaxy (MBE) chamber, which produce an excess of Arsenic in the material. Clusters of Arsenic are formed during the annealing [44], where the photo-induced carriers are trapped efficiently. Under these conditions it has been demonstrated fabrication of materials with carrier lifetimes shorter than $500fs$ [45–47]. The majority of photoconductive terahertz emitters use short-carrier lifetime semiconductors to suppress the excess Direct Current (DC) current by forcing the charge carriers with long transport times to recombine before reaching the contact electrodes. A compromise exists between optimally short carrier lifetimes and increased parasitic dark current that can cause premature breakdown of the material. Material absorption and excitation laser pulse duration are the top parameters to shape the THz frequency spectrum of emitters, and it is important for the frequency response of the THz detectors to have very short carrier lifetimes. Antennas generating THz that are fabricated from LT-GaAs and compensated semi-insulating GaAs with nanosecond carrier lifetime have a comparable conversion efficiency overall [48].

The THz absorption and dispersion in the substrate is limiting the THz bandwidth, in all photoconductive antennas. The THz wave is transmitted to any direction from the generation antenna, one half through the substrate and the other in free space. By using the later

half of the THz pulse, we are eliminating the absorption and dispersion effects from having the pulse propagate through the substrate [49].

1.4 PULSED AND ULTRAFAST LASERS

Several techniques have been developed in the past thirty years to generate ultrashort pulses. Ideally one would like to have ultrashort laser pulses of desired pulse width and pulse shape, wavelength, pulse energy, and repetition rate. A single laser source obviously cannot cover the entire range of desired parameters, and different approaches have been developed. Development of ultrafast lasers is an area of continued intense activity. Research on the generation of ultrashort laser pulses started almost immediately after the first demonstration of lasers. Techniques for switching the quality factor (Q) of the laser cavity typically generated nanosecond pulses. A laser oscillates in many longitudinal modes supported by the cavity and the gain spectrum. The technique of mode-locking, in which these modes are locked in phase, was developed by using a saturable absorber in the laser cavity. This and many other mode-locking techniques are now being used to generate ultrashort pulses.

Enormous progress has been made in the generation of ultrashort pulses since the first solid-state mode-locked lasers which did not provide tunability. Organic dye lasers, with wide gain spectra and the potential for femtosecond pulses, were invented in the late 1960s, and rapidly developed into versatile tools for spectroscopy because of their ultrashort pulse widths and tunability in the visible and the near-IR range. Techniques have also been developed to amplify and compress these short pulses, to generate different frequencies using nonlinear second harmonic generation and nonlinear mixing, and to generate ultrashort pulses of white-light continuum by passing an intense ultrashort pulse through a liquid. New solid state materials with wide gain spectra have been developed and have been used to generate pulses shorter than 5 fs directly from the laser oscillators without having to resort to pulse amplification and compression. Optical Parametric Oscillators (OPO) pumped by such solid-state lasers have increased the tunability range. These solid-state lasers have practically replaced the dye lasers as the basic ultrafast spectroscopy tool, and pumping these lasers with semiconductor diode lasers has made it possible to think of compact ultrafast sources. The availability of ultrafast lasers with a wide range of pulse widths, wavelengths, pulse energy, and pulse repetition rate makes it possible not only

to investigate a broad range of physical phenomena using ultrafast optical spectroscopy, but also investigate practical applications of ultrafast technology.

1.4.1 *Oscillator laser*

Ti:sapphire lasers (also known as $Ti : Al_2O_3$ lasers, titanium-sapphire lasers, or Ti:sapph) are tunable lasers which emit red and near-infrared light in the range from 650 to 1100 nanometers. These lasers are mainly used in scientific research because of their tunability and their ability to generate ultrashort pulses. Titanium-sapphire refers to the lasing medium, a crystal of sapphire (Al_2O_3) that is doped with titanium ions. A Ti:sapphire laser is usually pumped with another laser with a wavelength of 514 to $532nm$, for which argon-ion lasers ($514.5nm$) and frequency-doubled $Nd : YAG$, $Nd : YLF$, and $Nd : YVO$ lasers ($527 - 532nm$) are used. Ti:sapphire lasers operate most efficiently at wavelengths near $800nm$.

For low concentrations of Ti_2O_3 ($\sim 0,05\%$ mass proportion)in a melting charge of sapphire (Al_2O_3) the Ti^{3+} ions substitute the Al^{3+} in random positions of the forming crystal lattice, the electrical and optical properties of the crystal being dominated by the singular 3d electrons belonging to the external energetic levels of the Ti^{3+} ions. The internal electric field determines the splitting of the external electronic shell, the Cubical of this interaction characterizing the splitting of the energetic levels in excited state ^2E (double degenerated) and ground state $^2T_2$ which themselves are split by the spin–orbit coupling and a Jahn–Teller distortion. The absorption spectra of the doped crystal indicates the presence of a large excited state band, accessible from ground state corresponding to a spectral range from 450 to $600nm$ which matches the ionized Ar laser emission (Fig. 1.17).

The fluorescence spectrum of the crystal is shifted to longer wavelengths from 650 to $1,050nm$ because of phonon emission from the accepted charge carriers the corresponding lifetime being about $3\mu s$. Because the laser operation is based on the overlapping of two beams narrow focused in the case of cylindrical cross sections the system is very sensitive to the alignment of the optical devices and the mirrors which guides the pumping beam and must be mounted on rigid supports (Fig. 1.18).

The focus of the pumping beam is realized using a $10cm$ focusing lens with anti-reflective coating, placed eccentric to the beam in order to compensate the astigmatism of the pump radiation with

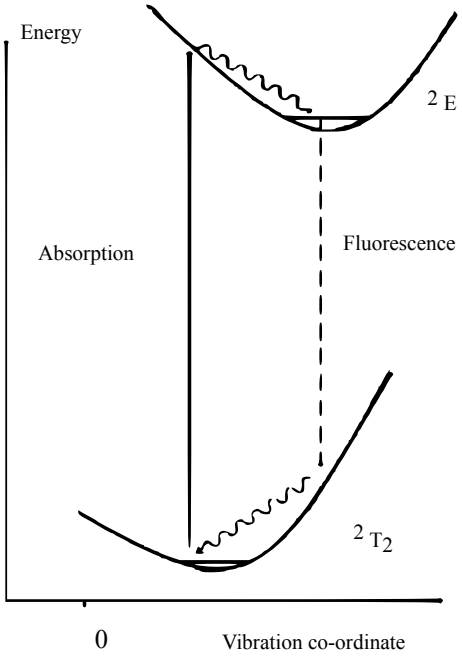

Figure 1.17: Energetic bands of Ti^{3+} ions in the Al_2O_3 crystal lattice. [50]

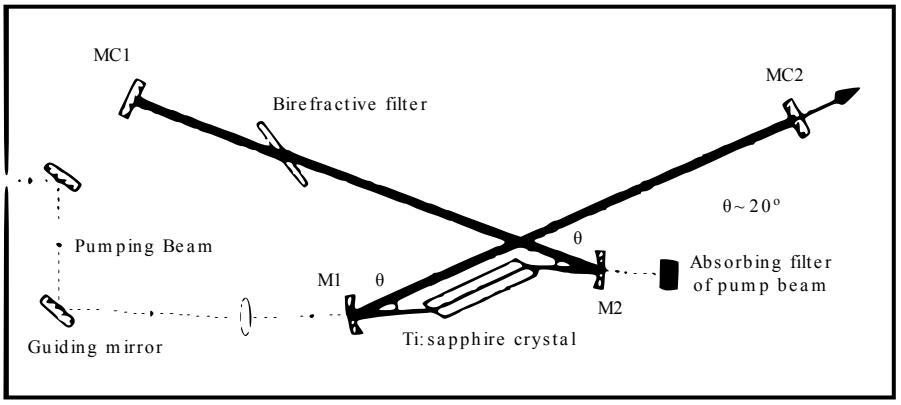

Figure 1.18: Laser cavity of continuous operating Ti-sapphire laser. [50]

that imposed by the Ti-sapphire crystal geometry. The Ti-sapphire crystal is placed between two mirrors (M1 and M2) characterized by 85% transparency for pump radiation and high reflectivity for fluorescence radiation of Ti-sapphire. The cooling of the crystal is realized by mounting it on a copper support and using a water flow at $\sim 8^{\circ}C$ temperature. In the case of 5 W pumping power and 3% transmission of the mirror MC2 one can obtain $750mW$ in continuous-wave (CW) operation mode of the Ti-sapphire laser. Mode-locked oscillators generate ultra short pulses with a typical duration between $10fs$ and a few ps. The pulse repetition frequency is in most cases is $\sim 70 - 90MHz$. The Ti-sapphire oscillators are normally pumped with a Continuous Wave (CW) laser beam from an argon or frequency-doubled $Nd - YVO_4$ laser, such an oscillator having an average output power of $0.5 - 1.5W$.

1.4.2 *Mode-locked oscillators*

A type of Ti:sapphire laser is the Mode-locked oscillators, that generate ultrashort pulses with a typical duration between a few picoseconds and 10 femtoseconds, in special cases even around 5 femtoseconds. The pulse repetition frequency is in most cases around 70 to $90MHz$. $Ti : sapphire$ oscillators are normally pumped with a continuous-wave laser beam from an argon or frequency-doubled $Nd : YVO4$ laser. Typically, such an oscillator has an average output power of 0.4 to 2.5 watts.

All lasers produce light over some natural bandwidth or range of frequencies. A laser's bandwidth of operation is determined primarily by the gain medium from which the laser is constructed, and the range of frequencies over which a laser may operate is known as the gain bandwidth. For example, a typical helium–neon laser has a gain bandwidth of about $1.5GHz$ (a wavelength range of about $0.002nm$ at a central wavelength of $633nm$), whereas a titanium-doped sapphire (Ti:sapphire) solid-state laser has a bandwidth of about 128 THz (a $300 - nm$ wavelength range centered at $800nm$).

The second factor to determine a laser's emission frequencies is the optical cavity (or resonant cavity) of the laser. In the simplest case, this consists of two plane (flat) mirrors facing each other, surrounding the gain medium of the laser (this arrangement is known as a Fabry–Pérot cavity). Since light is a wave, when bouncing between the mirrors of the cavity, the light will constructively and destructively interfere with

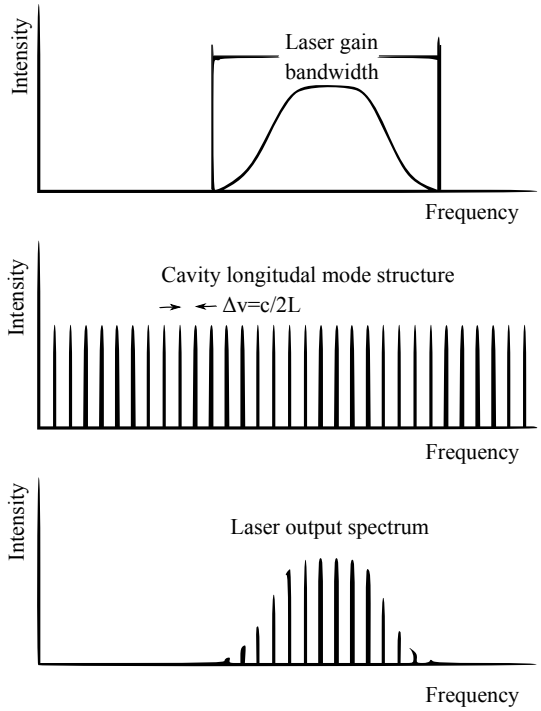

Figure 1.19: Laser mode structure

itself, leading to the formation of standing waves or modes between the mirrors. These standing waves form a discrete set of frequencies, known as the longitudinal modes of the cavity. These modes are the only frequencies of light which are self-regenerating and allowed to oscillate by the resonant cavity; all other frequencies of light are suppressed by destructive interference. For a simple plane-mirror cavity, the allowed modes are those for which the separation distance of the mirrors L is an exact multiple of half the wavelength of the light λ, such that $L = q\lambda/2$, where q is an integer known as the mode order.

In practice, L is usually much greater than λ, so the relevant values of q are large (around 105 to 106). Of more interest is the frequency separation between any two adjacent modes q and $q + 1$; this is given (for an empty linear resonator of length L) by Δv:

$$\Delta\nu = \frac{c}{2L}$$

where c is the speed of light ($3 \times 10^8 m/s$).

Using the above equation, a small laser with a mirror separation of 30 cm has a frequency separation between longitudinal modes of $0.5GHz$. Thus for the two lasers referenced above, with a $30 - cm$ cavity, the $1.5GHz$ bandwidth of the HeNe laser would support up to 3

longitudinal modes, whereas the $128 THz$ bandwidth of the Ti:sapphire laser could support approximately $250,000$ modes. When more than one longitudinal mode is excited, the laser is said to be in "multi-mode" operation. When only one longitudinal mode is excited, the laser is said to be in "single-mode" operation.

Each individual longitudinal mode has some bandwidth or narrow range of frequencies over which it operates, but typically this bandwidth, determined by the Q factor (see Inductor) of the cavity (see Fabry–Pérot interferometer), is much smaller than the intermode frequency separation.

2 EXPERIMENTAL SETUP

In this chapter I will give some insights to the elements that are used to perform the THz-TDS measurements. Most of them are shown in Figure 2.1.

2.1 LASER

As mentioned above for the THz-TDS measurements I used a Ti:Sa oscillator system delivering 45fs pulses centered at 800nm at a 4MHz repetition rate and 650nJ energy per pulse.

2.2 DELAY STAGE AND RETROREFLECTOR

A delay stage is utilized to lengthen one of the two beam paths. A delay stage is typically equipped with a retroreflector. A retroreflector is a mirror set that sends an outgoing beam parallel to the incoming beam. Two standard, adjustable mirrors can be used, as can special retroreflectors made for this purpose (for example, a corner cube reflector). A step of the delay stage in space corresponds to a step in time, since I sweep through our pulse in time by coinciding new parts of it with the gating pulse at the detector.

2.3 PARABOLIC MIRRORS

Off-axis parabolic mirrors are commonly used to collimate and focus THz light. Light emitting from an effective point source, such as from an LT-GaAs antenna (active region $5\mu m$) incident on an off-axis parabolic mirror becomes collimated, and collimated light incident on a parabolic mirror becomes focused. The sequential use of parabolic mirrors can focus light emitted from a point source. Samples for spectroscopy are commonly placed at such a focal point, where the spatial frequency distribution is nearly uniform. In our setup only two parabolic mirrors could be used to measure the performance of a photoconductor antenna. The first would "capture" the generated THz pulse, that has the shape of a temporally expanding shell of a sphere with a center at the active area of laser excitation , collimating

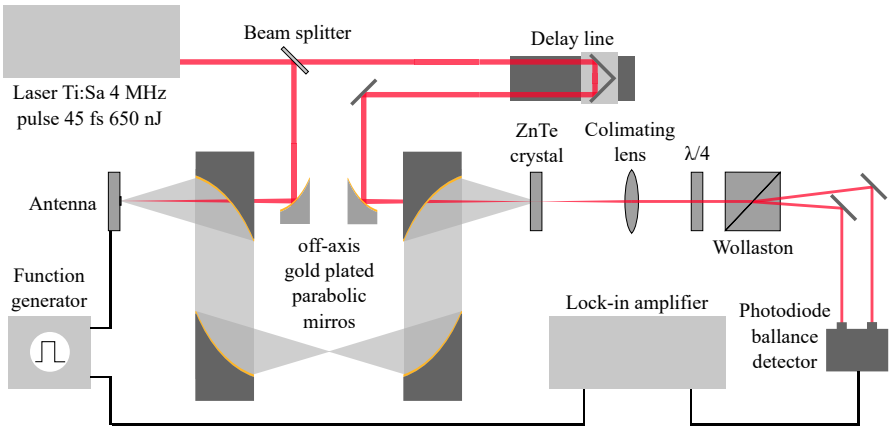

Figure 2.1: My TDS-TDS setup

the THz beam. The second one would focus the collimated beam, onto the active area of ZnTe crystal, spatio-temporal overlapping with the probe laser pulse. Rather than two mirrors, the setup has been initially designed, accommodating two more, 2*inch* in diameter, gold parabolic mirrors, which became useful for unexpected needed measurements. As seen in Fig. 2.1, the bottom parabolic mirrors intervene of the THz pulse path, focusing it and collimating again. At that focal point a sample was placed and characterized using an OPTP technique at room temperatures with capability at very low temperatures as well, by using a cryostat. All the measurements explained in the following chapters were performed in the four parabolic mirror arrangement.

2.4 NITROGEN PURGE

A purge box is typically used so that absorption of THz radiation by gaseous water molecules does not occur. Water is known to have many discrete absorptions in the THz region, which are rotational modes of the water molecules. Nitrogen, as a diatomic molecule, has no electric dipole moment, and does not (for the purposes of typical THz-TDS) absorb THz radiation. Thus, a purge box can be filled with nitrogen so that unintended discrete absorptions in the THz frequency range do not occur. In Figure 2.1 the box is including the antenna, all the parabolic mirrors, the ZnTe crystal up to Wollaston. it has two entrance and two exit holes for the beams.

2.5 LOCK-IN AMPLIFIER

A lock-in amplifier is a type of amplifier that can extract a signal with a known carrier wave from an extremely noisy environment. The device is often used to measure phase shift, even when the signals are large and of high signal-to-noise ratio and do not need further improvement.

Recovering signals at low signal-to-noise ratios requires a strong, clean reference signal with the same frequency as the received signal. This is not the case in many experiments, so the instrument can recover signals buried in the noise only in a limited set of circumstances.

The operation of a lock-in amplifier relies on the orthogonality of sinusoidal functions. Specifically, when a sinusoidal function of frequency f1 is multiplied by another sinusoidal function of frequency f2 not equal to f1 and integrated over a time much longer than the period of the two functions, the result is zero. Instead, when f1 is equal to f2 and the two functions are in phase, the average value is equal to half of the product of the amplitudes.

In essence, a lock-in amplifier takes the input signal, multiplies it by the reference signal (either provided from the internal oscillator or an external source), and integrates it over a specified time, usually on the order of milliseconds to a few seconds. The resulting signal is a DC signal, where the contribution from any signal that is not at the same frequency as the reference signal is attenuated close to zero. The out-of-phase component of the signal that has the same frequency as the reference signal is also attenuated (because sine functions are orthogonal to the cosine functions of the same frequency), making a lock-in a phase-sensitive detector.

The model I used is an SRS SR830 Lock-In Amplifier.

Part II

THE STUDY

3

ANTENNA PERFORMANCE

3.1 INTRO

In recent years, it has been demonstrated that irradiation by intense ultrashort laser pulses leads to the enhancement of material optical and electronic properties [51–53].This technique allows the realization of new electronic surface states a swell as a broad variety of micro- and nano-structured texturization [54, 55] depending on the femtosecond pulse-train characteristics or the presence of specific gas compounds. For example, hyperdoping of silicon has been achieved with nonequilibrium concentration of dopants in combination with controlled surface texturing allowing close to 100% absorption over a wider spectral range than the intrinsic material [56, 57]. Similar results on GaAs have recently been reported, where femtosecond laser ablation has shown strong absorption extended below the bandgap under low-light, broadband, continuous-wave illumination [58]. For the latter, the enhanced properties arise from the creation of micrometer-scale periodic ripples, with the creation of Surface Plasmon Polaritons (SPPs) as a possible explanation for this surface patterning [59, 60]. This periodic pattern acts as an antireflection layer, thus leading to enhanced photoabsorption [58, 61]. The ability to manipulate doping, photoabsorption, or carrier lifetimes in materials via this ultrafast ablation technique provides a new approach to engineering optoelectronic devices with enhanced performance, e.g., photovoltaics or THz devices.

Currently, the development of cost-effective radiation sources and detectors in the THz range is an active field of research. For example, photoconductive devices have allowed THz TDS to become a very powerful tool to investigate materials or chemical compounds as well as for pharmaceutical and security applications [13, 62–64]. With the emergence of a compact commercial THz-TDS system, one focus is the realization of photoconductive emitters and detectors based on low-cost and high-efficiency substrates. For this purpose, methods improving the photoabsorption, emitted THz spectral bandwidth, or reducing the carrier lifetime of GaAs have been investigated, such as implantation of ions [65], chemical passivation [66], or epitaxial growth techniques [67]. However, most of these methods are not time or cost efficient. Alternately, the femtosecond-laser-ablation technique

provides a fast and cheaper alternative for the realization of materials with engineered optoelectronic properties for THz applications.

Below, is studied and demonstrated a THz photoconductive antenna device processed on femtosecond-laser-ablated GaAs and compared with an antenna fabricated on the same SI-GaAs, without laser ablation. Counter-intuitive phenomena are observed; namely, for high optical excitation, the ablated device generates more efficient THz, despite exhibiting a lower photocurrent and lower carrier mobility. On the other hand, for low optical excitation, the ablated device shows poorer THz emission. To understand this behavior, the I–V characteristics are studied in conjunction with the emission properties, as well as the lifetime and photoconductivity of the carriers in the two devices using an OPTP [68]. The increase in photoabsorption and doped carrier concentrations are also measured in the two devices, resulting from the ablation process. For the high-photoexcitation regime, it is observed that increased photoabsorption in the ablated device results in greater emission,but the very short carrier lifetimes result in lowered photocurrent measurements. In the low-photoexcitation regime, it is observed that the presence of doped carriers arising from the ablation process diminishes the THz generation due to free carrier absorption.

3.2 EXPERIMENTAL SETUP

Figure3.1(a) is a photo of a fabricated photoconductive bow tie antenna composed of two gold electrodes with a 50μm gap. The surface of a second identical antenna is irradiated with a femtosecond pulse laser in order to ablate the surface as shown in Figure3.1(b). The laser system used for ablation delivers 120fs pulses centered at 800 nm at a 1kHz repetition rate. The surface ablation is realized with an average power of 5mW, and the beam scans the surface at 800$\mu m/s$ [58].The ablated pattern presents 20μm-large grooves defined by the scanning step of the translation stage as seen in Figure3.1(c).The mean depth of the grooves is 2.35μm.The ablated pattern alternates grooves with 3μm-diameter grains and periodic ripples owing to the SPP formation [shown in Figure3.1(d)]. The ripples are perpendicular to the grooves and laser polarization. Their length is 5.2μm, and their width 0.5μm. The period of the SPP pattern is 740nm, close to the ablation laser wavelength [69].

The performance of the femtosecond laser ablated SI-GaAs is compared with the nonablated SI-GaAs, when used as THz photoconductive emitters for THz-TDS. The setup is based on a Ti:Sa oscillator system

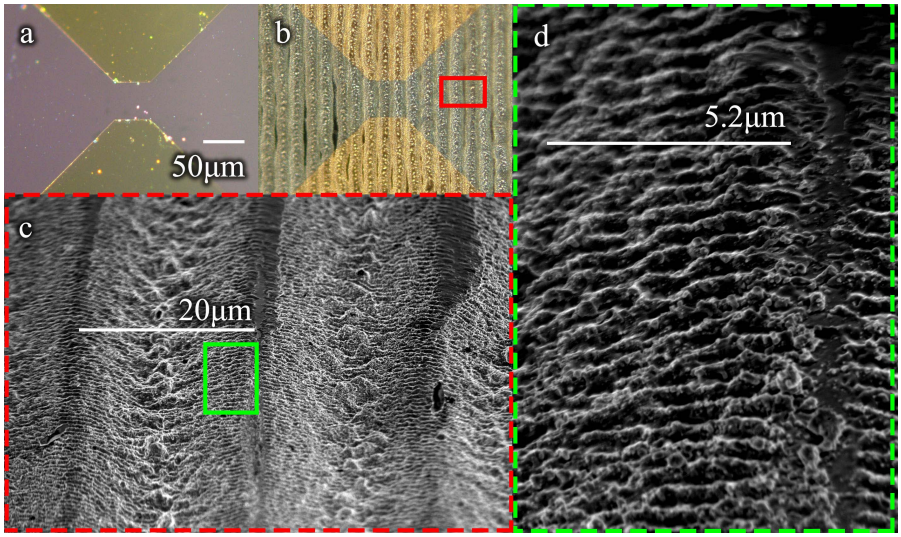

Figure 3.1: Optical microscope images of (a) nonablated GaAs and (b) femtosecond laser ablated photoconductive antennas. (c) Scanning electron microscope picture of the area within the red rectangle of (b) showing $20\mu m$ wide grooves. (d) Zoom within the green rectangle of (c) showing the formation of ripples

delivering $45fs$ pulses centered at $800nm$ at a $4MHz$ repetition rate. The emission from the antennas is collected through a set of off-axis parabolic mirrors. Electro-optic detection based on a $1mm$-thick ZnTe crystal is used. Both antennas were biased with a $10V_{pp}$ (V_{pp} stands for Volts peak to peak) square modulation at $10kHz$. Figure3.2(a) presents a comparison between the THz-detected transients generated by the ablated and nonablated GaAs-based photoconductive antennas for three different characteristic optical fluences ($10mJ/cm^2$, $200\mu J/cm^2$, and $2.2\mu J/cm^2$) exciting the $50\mu m$ antenna gaps. For high fluence ($10mJ/cm^2$), the ablated antenna shows the best performance and 65% improved efficiency. For intermediate fluence $(200\mu J/cm^2)$, ablated and nonablated devices exhibit similar performances. For low fluence $(2.2\mu J/cm^2)$, better emission is observed from the antenna based on regular SI-GaAs.

3.3 OPTICAL FLUENCE DEPENDENCE

In Fig. 3.3, we present the time-domain waveforms measured from the two devices for an excitation pulse of $6nJ$ ($25mW$) and a bias voltage of $7V_{pp}$ (Fig. 3.3a) and an excitation pulse of $24nJ$ ($96mW$) with a $20V_{pp}$ bias (Fig. 3.3b). Whereas the THz pulse duration is similar for

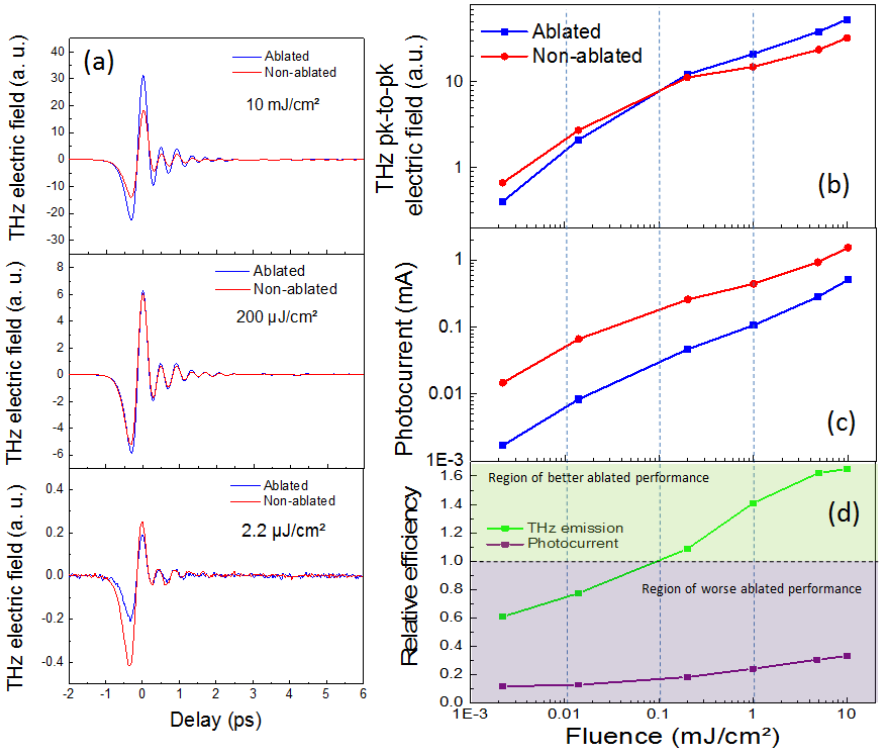

Figure 3.2: (a) THz-generated transients obtained for three different optical excitations ($2.2\mu J/cm^2$, $200\mu J/cm^2$ and $10mJ/cm^2$) from the ablated device (blue) and the non ablated device (red). (b)THz peak-to-peak electric field amplitude extracted from (a). (c) Photocurrent versus optical fluence. (d) Comparison of the THz emission (green) and photocurrent (purple) relative efficiency calculated as the ratio between the ablated and nonablated devices from (b) and (c).

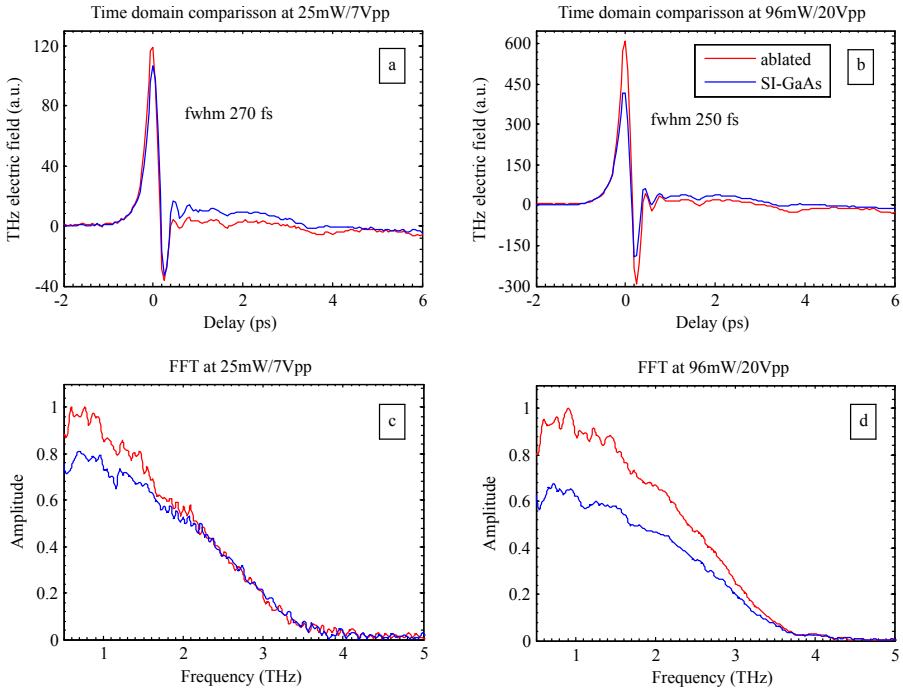

Figure 3.3: (a) Comparison of the measured THz time-domain waveforms of the laser ablated device (red) and untreated device (blue) at low excitation power ($25mW$) and low bias ($7V_{pp}$)(b) at higher power ($96mW$) and bias ($20V_{pp}$). (c) Associated FFT spectra at low excitation power and bias and (d) at higher power and bias.

both devices, we measure a higher peak electric field from the ablated device. In Fig. 3.3b, we observe 55% enhancement in the peak THz signal, in good agreement with previous results on femtosecond-laser-ablated GaAs photo-absorption [58]. Figs. 3.3c and (d) present the spectra obtained by FFT of the temporal waveforms for the low and high-power measurements, respectively. For the low power and low bias spectra, we observe an enhanced emission for frequencies below $2THz$. In the case of higher power and higher bias, the emission is improved up to $3.5THz$ of the bandwidth of the antenna. Fig. 3.4a shows the measured peak THz electric field as a function of the incident optical power for the two studied samples. To achieve these measurements, the applied bias is kept constant at $7V_{pp}$ and the power of the gating beam is fixed. More power is emitted from the ablated antenna and an improvement of the overall efficiency of 54% is estimated. This better efficiency is attributed to enhanced absorption. As absorption of the pump beam is enhanced, more photocarriers are generated using the same excitation power thus leading to a higher

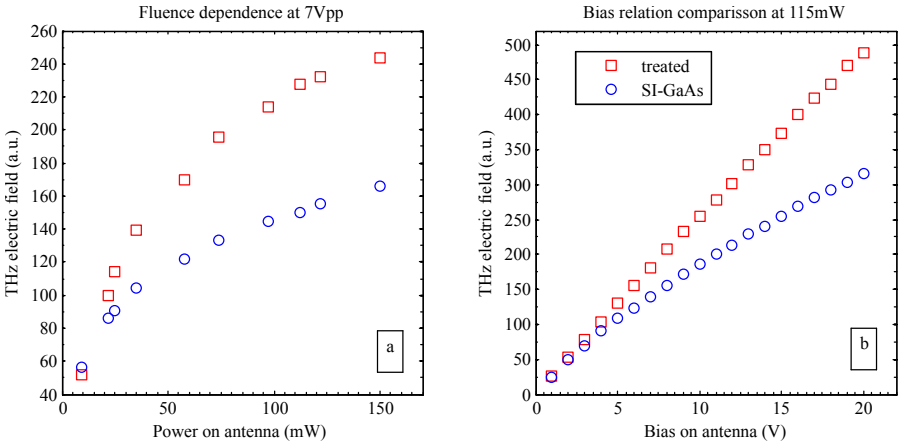

Figure 3.4: (a) Comparison of the measured peak THz electric field versus excitation power between ablated device (red) and untreated device (blue) and (b) versus applied bias on the antennas.

number of oscillating dipoles, i.e. more THz power. Fig. 3.4b presents the peak electric field as a function of the applied bias for both laser ablated and untreated antennas. As the power and bias is increased, the ablated antenna also shows the best performance. The ablated antenna exhibits no saturation in the applied bias range used for this study. Indeed, the ablated surface presents a larger effective area due to the grooves and ripples formation. This provides a larger contact area with the air which leads to a better thermal dissipation than the untreated device leading to 61% increased efficiency. Increase of the temperature results in increase of the disorder where less and less carriers participate to the oscillation of the dipoles.

Figure3.2(b) summarizes the measured peak-to-peak THz field as a function of the pump fluence illuminating the two devices. Two regimes are clearly identified —a low photoexcitation regime, where the ablated antenna results in weaker emission compared to the non-ablated one, and a high photo excitation regime, where the ablated antenna shows enhanced emission over the nonablated one.It also shows that the ablated device exhibits a lower saturation effect that is known to occur for optical fluences above $200\mu J/cm^2$ [70]. Figure3.2(c) presents a comparison of the photocurrent in the same conditions of optical excitation and applied bias, i.e., with the same $45fs$, $800nm$, $4MHz$ repetition rate laser system and $10V$ bias. In contrast with the THz emission measurements, the regime of high-optical excitation shows a significantly weaker photocurrent for the ablated antenna as compared to the nonablated one. Indeed, one generally expects that the material showing the higher photocurrent would give the best THz

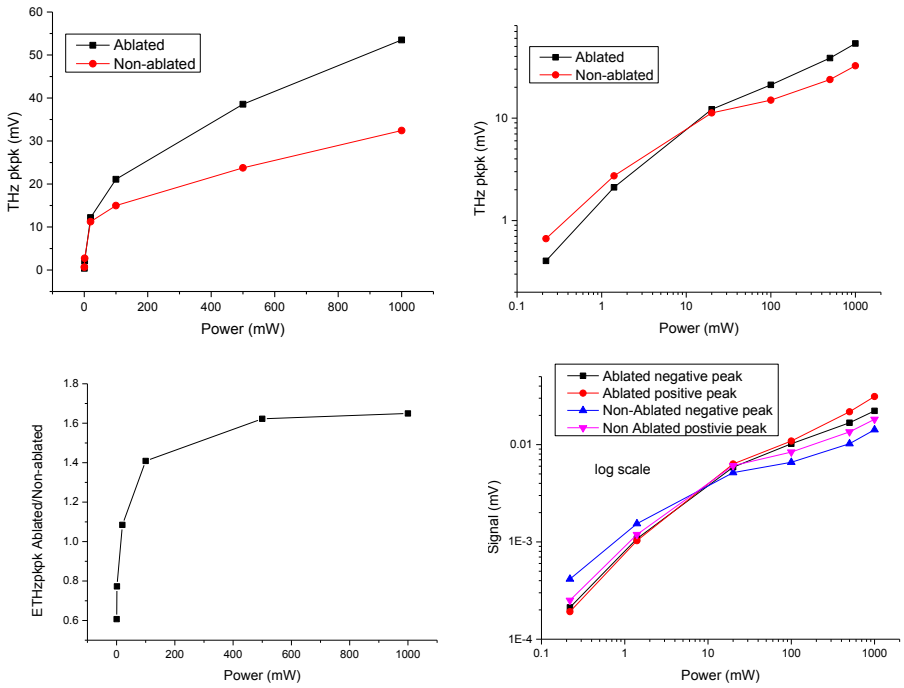

Figure 3.5: THz electric field, peak to peak value dependence on laser excitation power, for both antennas, in linear and log scale top. The ratio of ablated/non-ablated bottom left. The absolute values of positive/negative THz field peak values.

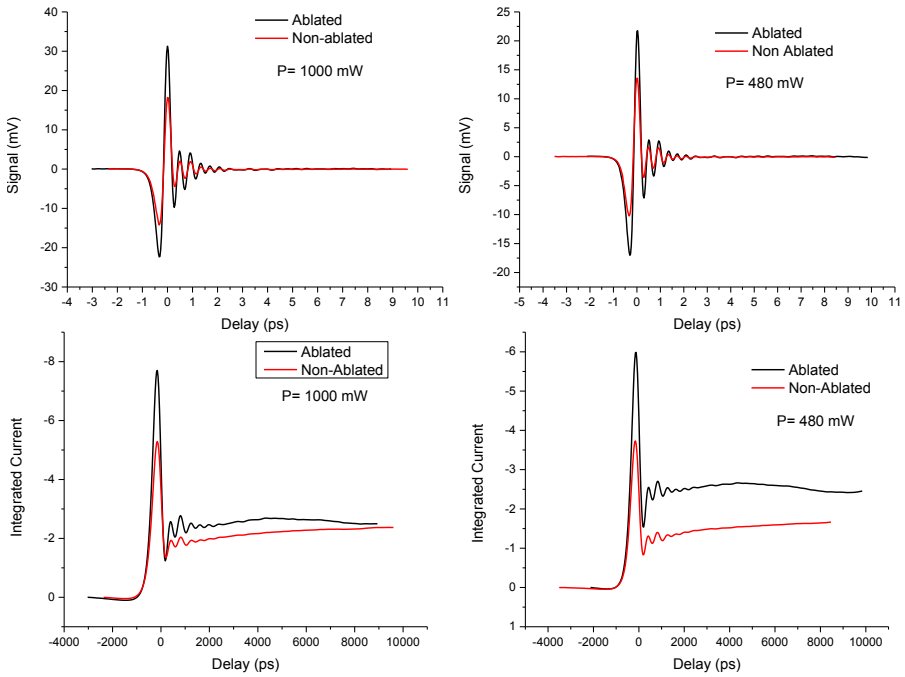

Figure 3.6: THz-TDS measurements for both antennas at 1000mW,480mW and their integrated current temporal profile.

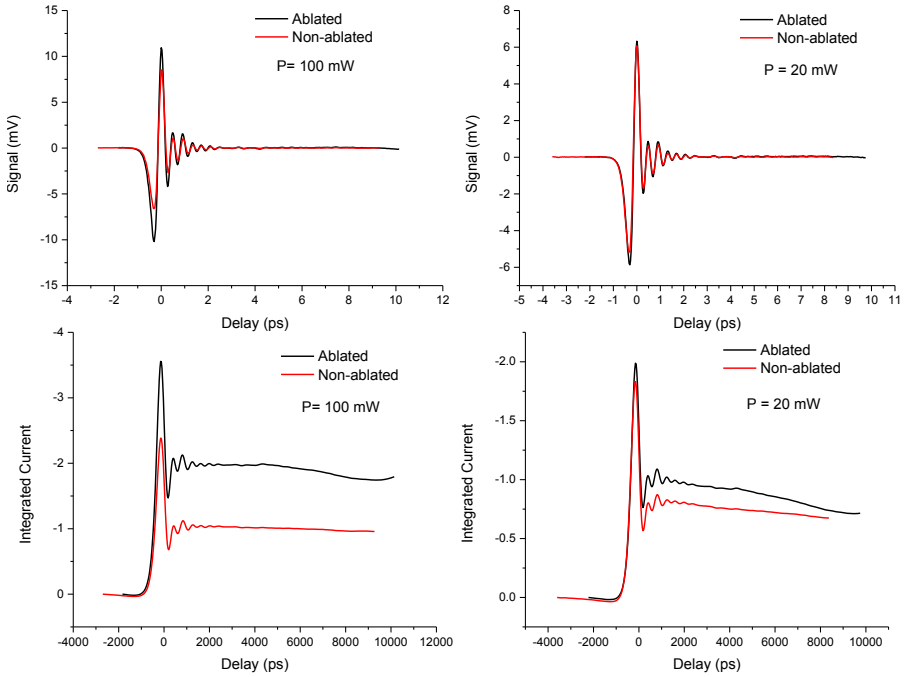

Figure 3.7: THz-TDS measurements for both antennas at 100mW,20mW and their integrated current temporal profile.

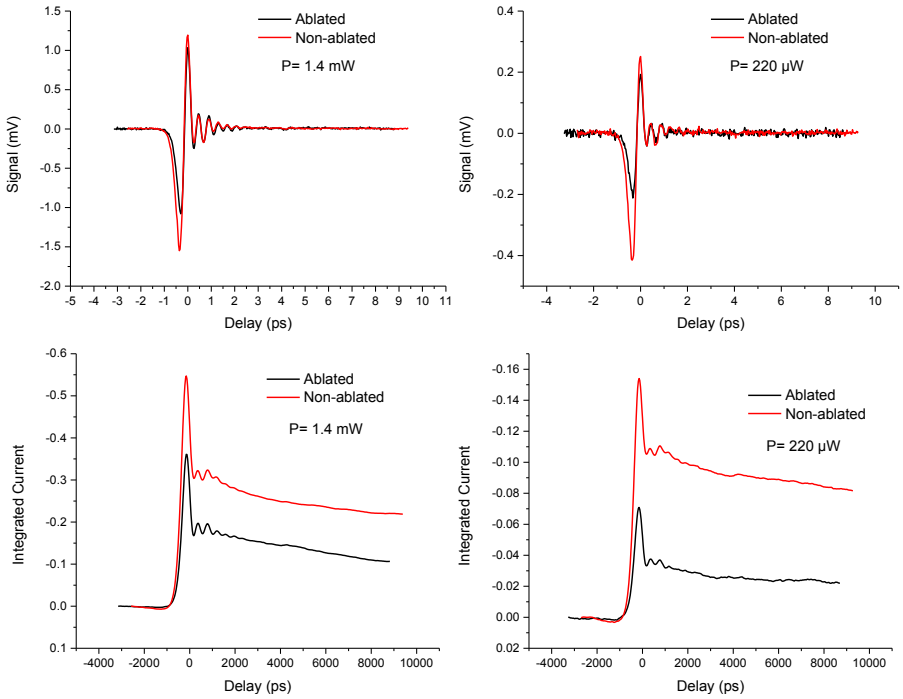

Figure 3.8: THz-TDS measurements for both antennas at $1.4mW$,$220\mu W$ and their integrated current temporal profile.

emitter. This is summarized in Figure3.2(d), which depicts the relative efficiency obtained from Figure3.2(b) and 3.2(c), i.e., the ratio of the ablated over the nonablated, showing up to 65% enhancement of the THz emission,despite exhibiting only a third of the photocurrent compared to the nonablated material. To investigate this discrepancy, OPTP measurements were performed on both the samples to measure the lifetime and photoconductivity of the excited carriers. On Figure3.12(a) and 3.12(b) are plotted the OPTP differential transmission signals for the (a) ablated GaAs and (b) nonablated GaAs for optical fluence varied from $1.6\mu J/cm^2$ to $2.2mJ/cm^2$. In order to cover three orders of magnitude for the optical pump exciting the samples, two different setups based on two different laser systems were used to perform the OPTP measurements. From 1.6 to $12\mu J/cm^2$, the source laser that is used has properties of $4MHz$, $650nJ$, $45fs$, $800nm$, thus allowing for a high signal-to-noise ratio even at low optical fluence. In this case, a THz probe is generated via an interdigitated photoconductive antenna as described in Ref.[71] biased with a $10kHz$ modulation and $20V_{pp}$ applied voltage. For high fluence, a $1kHz$ Ti:Sa $(100fs, 800nm)$ amplifier system is employed allowing us to reach up to $2.2mJ/cm^2$. The THz probe is generated via optical rectification in a $1mm$ thick

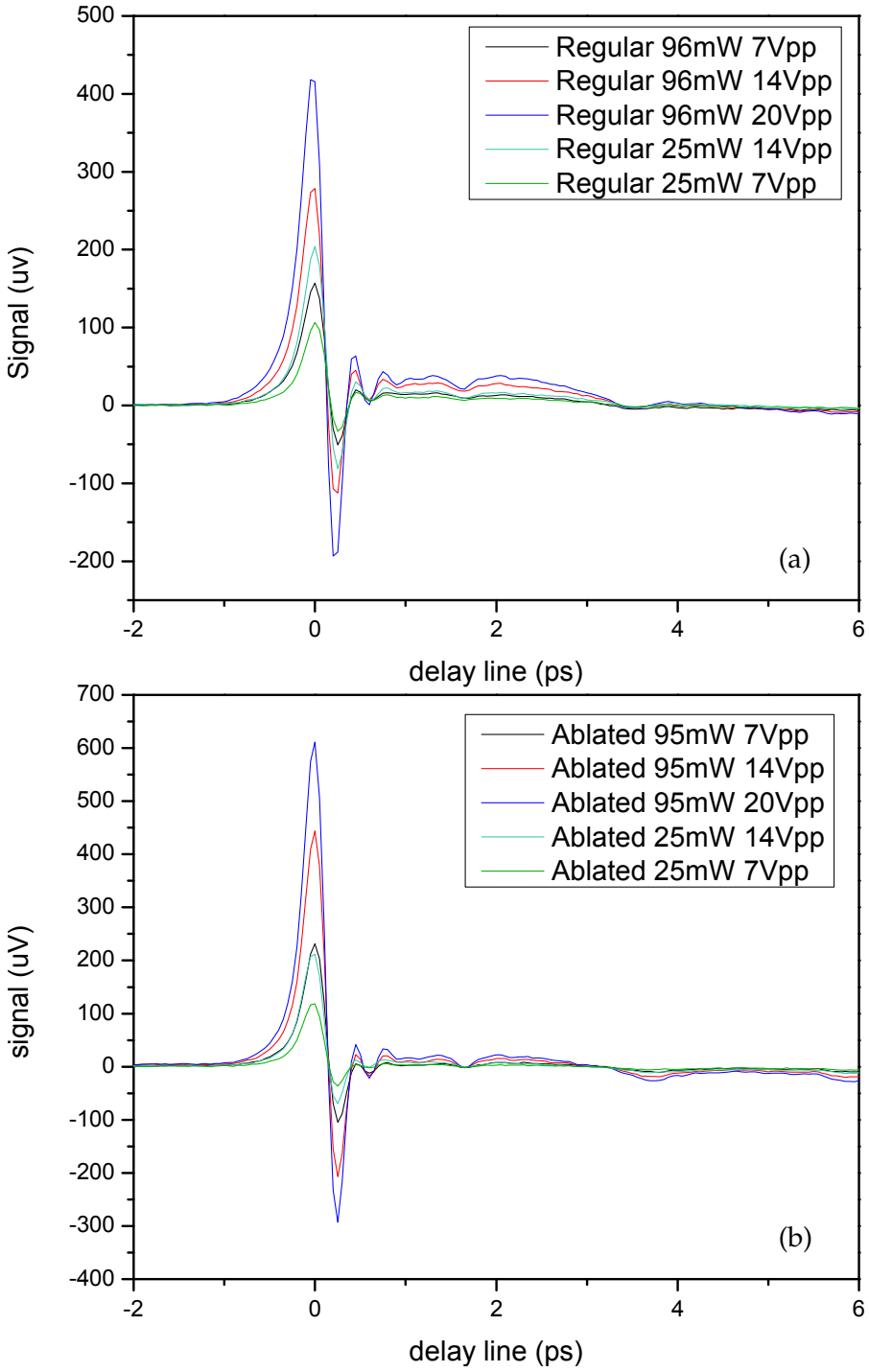

Figure 3.9: THz electric field of (a) non-ablated and (b) ablated antenna for different applied bias and excitation power.

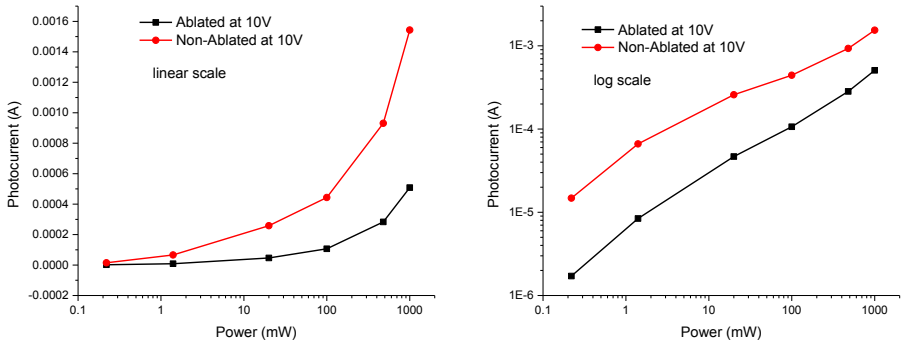

Figure 3.10: Photocurrent dependence on excitation power for both antennas at 10V bias.

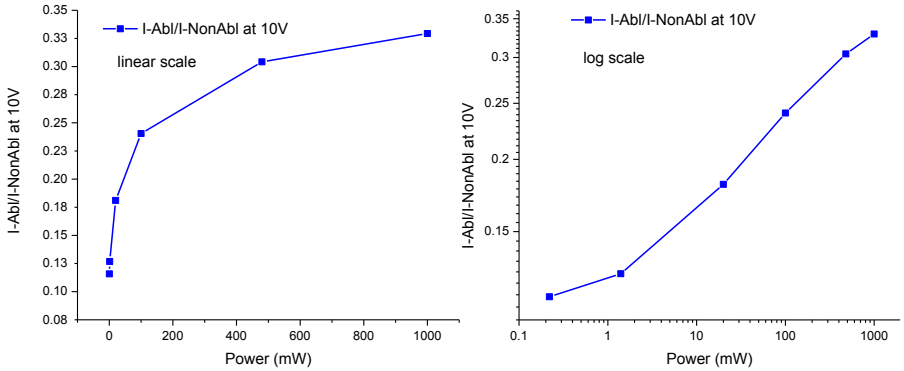

Figure 3.11: Normalized Photocurrent dependence on excitation power of the ablated antenna in respect to the non-ablated at 10V bias.

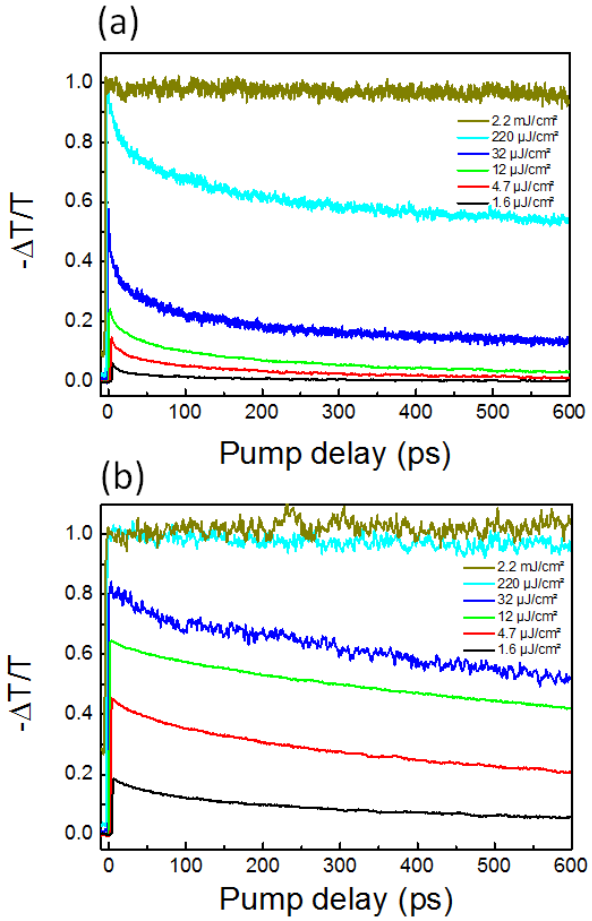

Figure 3.12: OPTP negative differential transmission of (a) ablated GaAs and (b) nonablated GaAs for pump fluences varied from $1.6\mu J/cm^2$ to $2.2mJ/cm^2$.

ZnTe crystal. Figure3.12(b) shows the expected response from regular SI-GaAs, i.e., a long carrier lifetime extending above $600ps$. For fluence higher than $200\mu J/cm^2$, a saturated response is observed, resulting in a complete screening of the THz probe by the photoexcited carriers. Figure3.12(a) shows the differential THz transmission response from the ablated material measured for the same pump fluences as the nonablated antenna. For low pump fluences, the negative differential transmission of the THz probe is lower in the ablated material, which rapidly becomes comparable to that in the nonablated material at pump fluences of $200\mu J/cm^2$ and higher, showing similar saturation effects as the nonablated material. Figure3.13(a) conveys this point by plotting the amplitude of the OPTP differential signal versus pump fluence at zero delay for fluences up to $200\mu J/cm^2$. These results are consistent with the generation of THz transients from the two antennas as discussed in Figure3.2(a)—at low fluences, the OPTP signals and the THz emission are weaker in the ablated antennas, while at higher fluences, the OPTP signals and THz emission are comparable or stronger in the ablated antennas. It also shows that the enhancement of THz emission does not originate from the ablation of the electrodes, as OPTP measurements were performed on non-patterned materials. These measurements suggest that at high pump fluences, the ablated material exhibits higher photoconductivity, which we attribute to the higher photoabsorption in the ablated materials acting as an antireflection layer as previously reported in Ref.[58]. This is also confirmed by Fourier-transform infrared spectroscopy (FTIR) measurements in these specific samples. Figures3.13(c) and 3.13(d) present the transmittance in the mid-Infrared (IR) range (0.1-0.8eV) and NIR (from 1.1 to 1.4eV), respectively. Whereas the nonablated GaAs shows a below bandgap flat transmission of about 50%, the ablated material presents significantly lower transmission (for all energies ranging from 0.2 to 1.4eV), as well as a prominent transmission dip in the mid-IR, indicating the previously reported presence of below bandgap states and higher photoabsorption originating from the ablation process [58, 72, 73]. In Figure3.12(a) is observed, that the dynamics of the photocarriers is given by a bi-exponential decay rate, and the ablated material exhibits much shorter carrier lifetime than the nonablated one. Figure3.13(b) presents the fast component of the decay time obtained by fitting the OPTP differential signals of Figure3.12(a) with a bi-exponential decay function. It demonstrates that the decay is shorter as the pump fluence increases, with the decay time decreasing from 12 to $3ps$ as the pump fluence varies from 1.6 to $32\mu J/cm^2$. For higher fluence, as saturation occurs owing to complete screening of the THz probe,

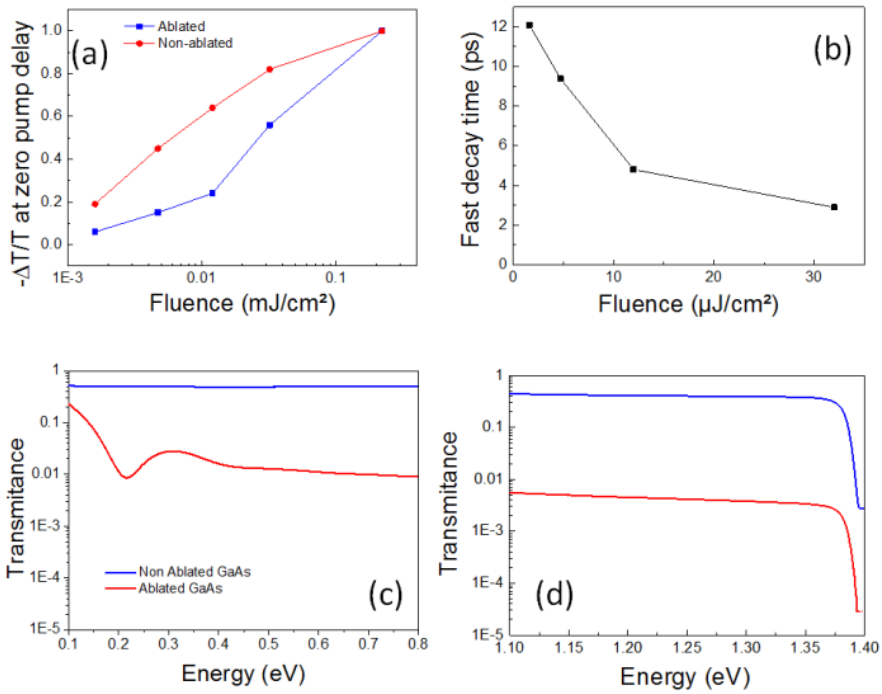

Figure 3.13: (a) OPTP negative differential transmission at zero delay versus pump fluence extracted from Figure3.12 for the ablated (blue) and non-ablated GaAs (red). (b) Fast decay time component obtained from bi-exponential decay function fit of the OPTP signals for the ablated GaAs. (c) Comparison of the transmittance between the ablated and non ablated GaAs in the mid-IR range and (d) in the NIR range.

fitting is not reliable. At high pump fluences, the short carrier lifetimes in the ablated materials explain the perceived contradiction between the THz-generation properties and the photocurrent measurements for the two antennas (although shorter carrier lifetime does not affect the generated THz amplitude). Indeed, as it is a DC measurement, one can access only the average photocurrent. Therefore, with a long lifetime, photocarriers in nonablated GaAs will contribute more, whereas with a sub-10ps lifetime, photocarriers in ablated GaAs will show very little contribution. It should be noted that our observation of lower photocurrent in the ablated device with 50fs, 800nm pulses does not contradict previous observations [58], which were done under different experimental conditions CW, broadband excitation.

The low-fluence behavior of the THz emission properties of the two antennas can be understood by noting that the ablation process typically results in an n-doped material. Hall effect measurements on the ablated material indicate n-doping with a sheet concentration of $1.2 \times 10^{12} cm^{-2}$ and a low carrier mobility of $5 cm^2/Vs$. Thus at low fluences, despite the increased photoconductivity of the ablated material due to greater photoabsorption, the emitted THz transients are absorbed via the native n-doped carriers resulting from the ablation process. As one gets to higher pump fluences, with photocarrier densities significantly larger than the doped carrier concentration, one begins to observe the effects of improved photoabsorption via enhanced THz generation in the ablated antennas.

3.4 RESULTS

In conclusion, the first THz photoconductive antenna based on femtosecond laser-ablated GaAs is demonstrated, with up to 65% improved THz-generation efficiency compared to SI-GaAs antennas. Our results are explained by measuring and understanding the impact of femtosecond-laser-ablation on the optoelectronic properties of SI-GaAs. Further optimization and directions of study involve the orientation of the ablated grooves with respect to the electrodes, the polarization of the optical excitation, or other parameters involved in the ablation process. The surface structure of the ablated device determined by ablation parameters such as wavelength, power, pulse duration, and scanning speed can also be optimized [59, 60]. The ripples seen in our device correspond to the wavelength of 800-nm ablating pulses, and are subwavelength compared to THz wavelengths. Thus, we estimate that variations in wavelength of the ablating laser over the visible and

NIR will not significantly alter the performance of the device from this perspective. Overall, it is demonstrated that the femtosecond-laser-ablation process provides a powerful tool to engineer material properties such as doping, photoabsorption, and carrier lifetime, thus allowing for a new route toward cost-effective, efficient THz devices and optoelectronic materials.

4

OPTIMIZING THE ANTENNA

In the previous chapter it is demonstrated increased efficiency in terahertz emission from a laser ablated antenna. The first antenna that was used, has been fabricated from a SI-GaAs substrate, with deposited gold electrodes and laser ablated surface between the electrodes gap. To further investigate how the performance of the device can be improved, we performed a parametric analysis on the laser ablation process.

4.1 FABRICATION

An SI-GaAs wafer was prepared, by cutting it in square pieces, with side size of $1cm$. Cleaned it with distilled water and detergent, apply Isopropanol (IPA), acetone in ultrasonic bath and finally dry it with a jet of nitrogen gas at room temperature, to agitate and remove dirt particles from the surface. The sample is placed and fixed on a disk that later rotates at $2000rpm$ to spin-coat the photoresist, a liquid polymeric material, with even layer thickness across the entire surface. The used photoresist was PMMA and is the material that the image will be transferred to, during the photolithography process. Once the substrate has been coated with photoresist, the substrate is then exposed on an exposure device. E-beam photolithography technique was used to expose individual areas of the photoresist in the bow-tie shape of our antenna. Once exposed, the substrate is then immersed in a developer solution, to dissolve away areas of the photoresist, that were exposed to light. Leaving the negative design pattern of the mask. After development, the resist pattern is observed on the substrate. In the next step the sample is placed in a vacuum chamber for thermal deposition of a thin $5nm$ adhesion titanium layer, to assist the $20nm$ gold layer that follows to stick better on the semiconductor surface. Finally the sample is bathed in acetone, to remove the leftover photoresist and rinse with IPA because acetone contaminated with resist forms streaks when it evaporates.

By the end of this process, a gold bow shaped electrode antenna is fabricated, on a GaAs substrate that is able to produce THz pulses when used on a THz-TDS setup. Our next step is to perform laser

ablation on the surface between the electrodes, but previously, the parameters that can optimize the performance of laser ablation should be investigated.

4.2 LASER ABLATION

In the following steps, parametric analysis was performed, to determine the values for the parameters to be used for the laser ablation of our device. We examine how the ripples from laser ablation are affected. The ripple shape and characteristics are having an important role in THz efficiency because of the relation between the surface semiconductor reflectivity and the IR laser to THz translation ratio. As mentioned in the previous chapter lower reflectivity is increasing the optical absorption, which in turn increases the photoexcited carriers, the photocurrent and as a result the electric field amplitude of the THz pulse. Ripples are assisting light to get absorbed easier due to the increased surface area of the semiconductor as well as the shape of the ripples that traps photons by internal multi-reflections on the sides of them.

The experimental optical setup consisted of an amplifier system Spectra Physics Spitfire Ace ($800nm$, $1kHz$, $5mJ$, $70fs$), an optical microscope and a translation stage. The laser beam was guided to the entrance of the optical microscope, reflected on a dichroic mirror at $800nm$ wavelength and onto the semiconductor substrate. The substrate was moving perpendicular and on-axis to the beam by a high precision three axis translation stage. The process was monitored by a camera in real-time, giving minor feedback for the results of the ablation process but rather for aligning the ablation patterns.

The threshold for the lowest fluence needed on the surface was investigated , in order to have laser ablation , which stands below the limit of surface melting and mass removal. By adjusting scan velocity of the translation stage, the number of laser pulses applied on the same area were varied. The number of pulses are acting cumulative, increasing the ripple depth. Polarization of the initial laser beam, linear polarized in this case, defines the ripple direction. Finally the step size in one scanning direction was measured, which causes difference in spatial overlap of ablation. Post the ablation process Scanning Electron Microscope (SEM) images where acquired to visualize and quantify the results.

In this measurement, the optical power of the laser ablation beam was altered by introducing Neutral Density (ND) filters. A pyroelectric

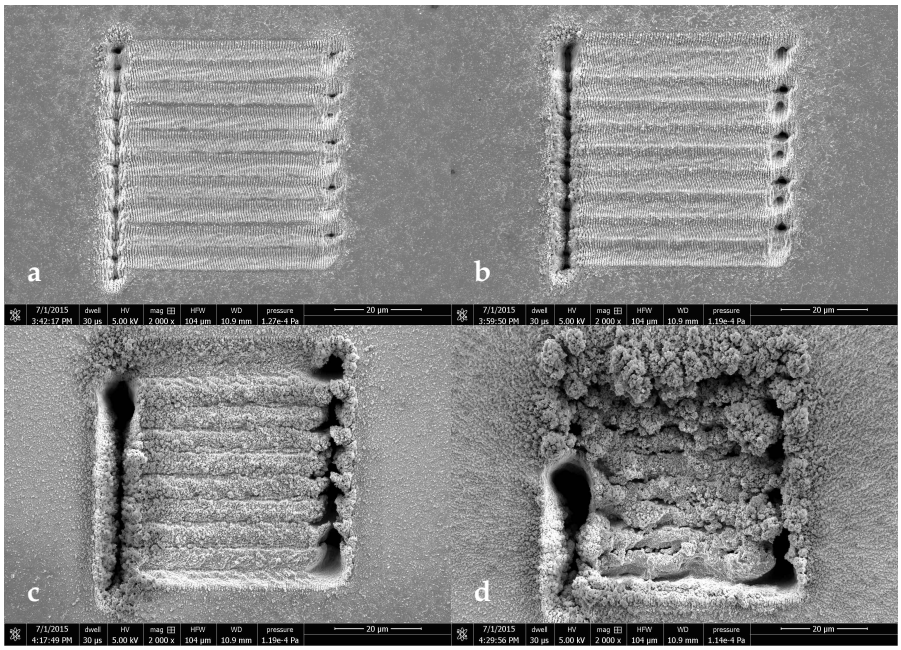

Figure 4.1: Dependence of ripple formation on laser optical power at (a) $50\mu W$, (b) $90\mu W$, (c) $545\mu W$, (d) $1340\mu W$.

detector was used to measure the optical power close to the semiconductor surface, but being cautious not to enter the focal area where the beam has enough intensity to cause damage to the detector. On the surface of the semiconductor the beam spot size was measured at $20\mu m^2$. At low power of $50\mu W$ ripple formation is visible Fig.4.1a, as well as with power at $90\mu W$ Fig.4.1b. At $545\mu W$ a critical threshold is surpassed causing mass removal and melting with resolidification, as seen from the patterns on the surface. At even higher optical power severe damage to surface cause irregular shapes and unpredicted topography. In this case we didn't go to lower power since the ripples are well defined for $50\mu W$ already.

By modifying the scanning velocity of the laser beam, the number of pulses that ablate each spot on the sample were defined. The repetition rate of the laser as mentioned earlier is $1KHz$ causing irradiation of 14 pulses per spot at $300\mu m/s$ scan velocity (Fig.4.2b) for a spot size of $4.24\mu m$ wide. Increasing the number or pulses per spot causes cumulative contribution causing areas with higher intensity, such as the center of the beam to have deeper grooves Fig.4.2a. When the scan velocity is increased to $3mm/s$ the number of pulses per spot is decreased to 1.4, being under the ablation threshold and not causing any ripples but rather small local deformations Fig.4.2c. Another

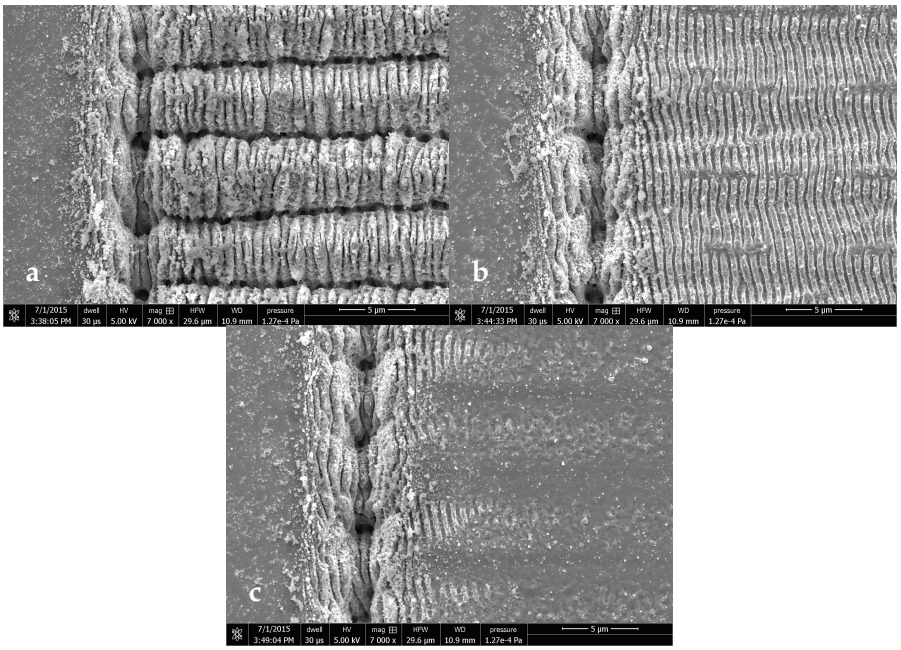

Figure 4.2: Dependence of ripple formation on scanning velocity for (a) $30\mu m/s$, (b) $300\mu m/s$ and (c) $3000\mu m/s$.

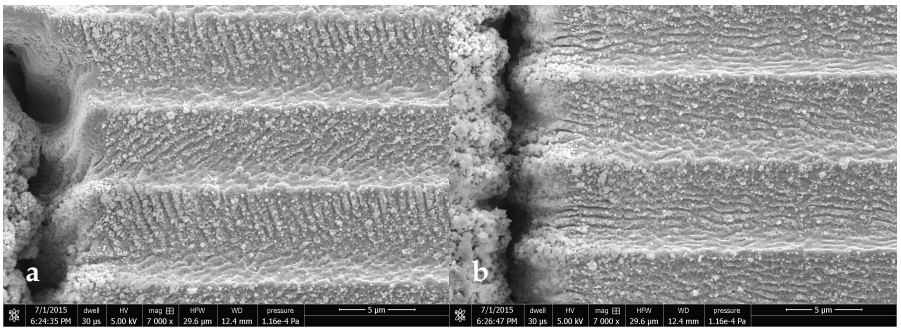

Figure 4.3: Ripple angle direction dependence for laser polarization of (a) 60 and (b) 90 degrees.

parameter to increase the roughness of the surface was to alter the ripples direction. By inserting a quarter-waveplate ($\lambda/4$) in the path of the beam before the microscope, the polarization angle was defined. For different angles of 60 and 90 degrees, deeper ripples were not observed, neither rougher surface structures Fig.4.3. Since deeper grooves on the path of the scanning were observed, it could be due to high intensity or number of pulses that caused mass removal, melting and destroying the finer ripples. The laser pulse profile has a Gaussian energy distribution causing a greater ablation effect in

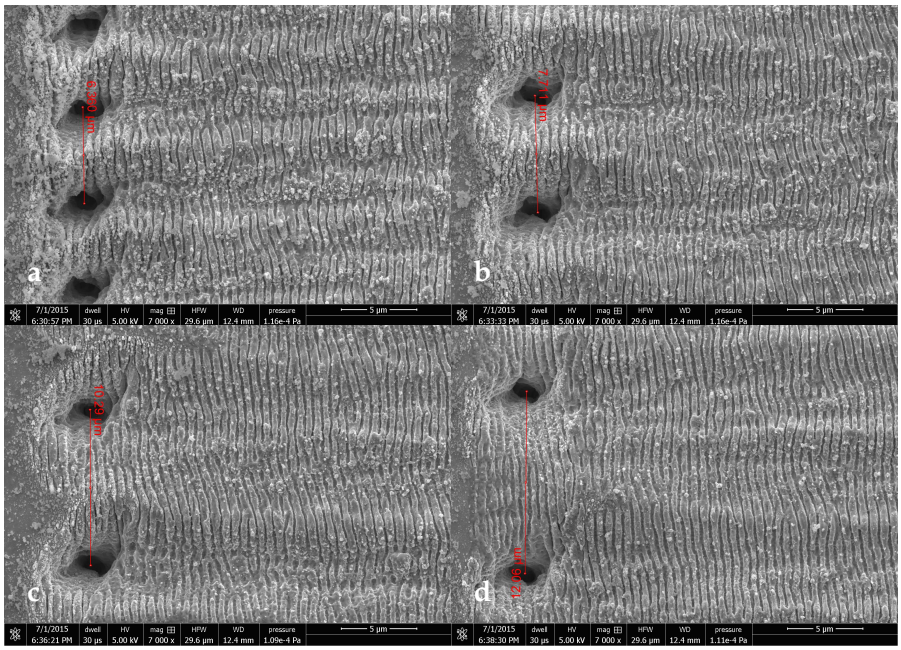

Figure 4.4: Different overlap of laser ablation spot, for y-step value of (a) $6.3\mu m$, (b) $7.7\mu m$, (c) $10.3\mu m$ and (d) $12\mu m$.

a shorter radius of the beam center. By changing the beam overlap area during the scanning, a higher uniformity in ripple formation was proposed. Choosing different scan steps in the Y axis, caused variations in the overlap of the beam. From the acquired SEM images Fig.4.4 for lower step size, ripples seem to have irregularities, while as the step size increases, ripples are becoming more homogeneous. The optimal step size is dependent on beam intensity and number of pulses per spot.

4.3 PREPARATION FOR THE THZ SETUP

Since the optimal parameters of ablation have been defined in the previous measurements, they were applied on the fabricated antenna. The square substrate that holds the antenna needs to be mounted on a base so it can be placed in the THz-TDS setup. Using a *wire bonding* device, the antenna electrodes were connected to larger contacts so the wires that will be connected to the function generator can be soldered, for creating the electric field across the electrodes gap Fig.4.5a. A cyan tint is visible coming from the ablated area caused by the subwavelength ripple dimensions that act as a diffraction pattern. The bow tie shape is duplicated and rotated 90 degrees so the shape forms a cross

around the gap. This design enables to apply the electric field both parallel and perpendicular to the ripple direction, in order to measure if THz pulse properties are dependent on the way ripples are aligned and the polarization of the laser pulse that generates THz. With grey color is the GaAs substrate, in gold color are the Gold electrodes and between them the laser ablated gap with ripples creating a grating effect, reflecting different colors at different viewing angles Fig.4.5b.

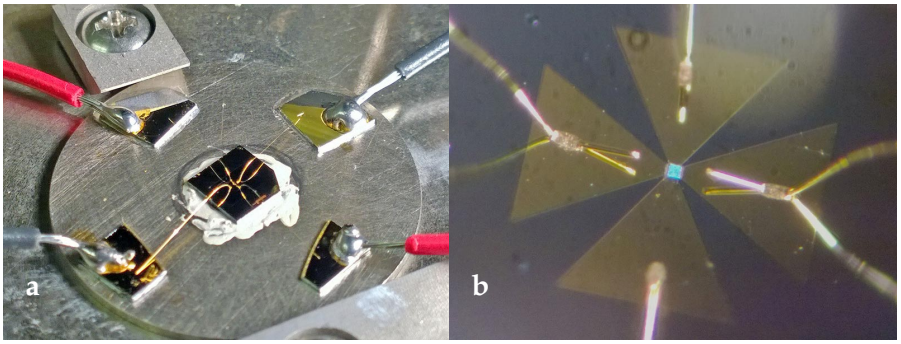

Figure 4.5: Photograph of the fabricated antenna (a) mounted on a metallic disk and wire-bonded to the contacts that connect to the function generator and (b) under the microscope the ablated area between the electrode gap.

5

THEORETICAL MODEL OF GAAS ULTRAFAST DYNAMICS

5.1 INTRO

Over the past decades, laser-based material processing with ultrashort pulsed laser sources has received considerable attention due to its important technological applications, in particular in industry and medicine [74–82]. Rapid energy delivery and reduction of the heat-affected areas are the most pronounced advantages of the technique compared to effects induced by longer pulses [83], which reflect the merit of the method as a potential tool for laser-assisted fabrication at micro- and nano-scales. One type of surface modification, the so-called Laser Induced Periodic Surface Structures (LIPSS) on solids have been studied extensively for linearly polarized beams. In recent works, it was also shown that it is possible to produce even more functional surfaces by using more complex polarization states. It turns out that the morphological features of structures provide unique optomechanical properties that can be used in many applications [84–87].

Previous theoretical approaches or experimental observations related to the understanding of the underlying physical mechanism for the formation of these structures were performed in a variety of conditions [88–100]. The most representative types of LIPSS that have been explored are the usually termed Low Spatial Frequency LIPSS (LSFL), High Spatial Frequency LIPSS (HSFL) ripples, grooves and spikes. In case of metallic and semiconducting materials, ripples are formed at low, microgrooves at intermediate [101] and quasi-periodic arrays of microspikes [102, 103] at high number of pulses (NP) or fluence. LSFL have spatial periods of the order of the laser wavelength λ_L. In most materials, they are oriented perpendicularly to the laser beam polarization. In dielectrics, LSFL were observed either perpendicular or (for very large band gap materials) parallel to the beam polarization. By contrast, grooves are supra-wavelength structures and are orientated parallel to the polarization of the laser beam [84, 94, 96] .

To explain the underlying physical origin of LIPSS formation, it is important to note that following irradiation with ultrashort pulses, a series of multiphysical phenomena take place [104–108]. With respect

to the formation of ripples, various mechanisms have been proposed to account for the production of periodic structures: interference of the incident wave with an induced scattered wave [89, 91, 94], or with a SP wave [90, 93, 109–112], or due to self-organization mechanisms [113].

While the precise physical mechanism for the origin of LIPSS is still debatable, one process that undoubtedly occurs is a phase transition that eventually leads to a surface modification. Physical mechanisms that lead to surface modification have been explored both theoretically and experimentally [82, 84, 90, 93, 94, 107, 112, 114–119] and it is evident that a precise determination of the morphological changes upon irradiation requires a thorough investigation of phase transitions and re-solidification process.

On the other hand, femtosecond laser interaction involves several complex phenomena, including energy absorption, photon-ionization processes, electron excitation, electron-relaxation processes, phase transitions and/or thermomechanical effects, re-solidification and mass ejection. In principle, the laser beam parameters (wavelength, pulse duration, fluence, number of pulses, angle of incidence and beam polarization state) determine the onset of the surface modification as energy absorption, electrodynamical effects and relaxation processes are critical to the material heating. The complexity of the processes and ionization mechanisms is material dependent as the laser source is used to excite, firstly, electrons/carriers from the valence to the conduction band before the energy is transferred into the lattice system [120]. One characteristic, though, that influences the thermal response of the material is the amount of the absorbed energy which is also closely related the electron excitation level (i.e. reflectivity) and dynamics.

To fully understand the ultrafast dynamics of the excited carriers upon irradiation with ultrashort pulses, it is important to perform a thorough analysis of the influence of the laser parameters on the thermal response of the material. Theoretical models that describe the fundamentals of laser-matter interaction for various types of materials (i.e. metals, semiconductors, dielectrics) and experimental studies successfully provide a detailed analysis of the physical mechanisms behind a plethora of structural effects (i.e. production of craters, evaluation of damage thresholds, LIPSS formation) [93, 120–124].

Nevertheless, although for many semiconducting materials, the physical mechanism that describes ultrafast dynamics is well-established and the theoretical model works efficiently in various conditions (that lead to high excited carrier densities, $10^{20} - 10^{22} cm^{-3}$), there is still a missing picture for some types of semiconductors such as GaAs [105,

125–128]. More specifically, GaAs is characterized by a higher electron mobility and higher thermal stability than Si, and it has a direct band gap which makes it more efficient in absorbing and emitting light. Thus, this material has a better performance in solar-harvesting energy-related applications [129] or terahertz antennas [130]. A complete understanding of the ultrafast electron and lattice dynamics for large number of excited carriers ($> 10^{20} cm^{-3}$), close and beyond the damage threshold (i.e. associated to the fluence that induces melting) of GaAs, will allow the identification of the dominant processes in this regime. Furthermore, behaviour of the material in conditions that lead to highly excited carrier densities is expected to allow an optimization of laser-based micromachining of GaAs and produce morphologies (such as LIPSS) with impressive properties for the aforementioned applications. The elucidation of these issues is of paramount importance not only to understand further the underlying physical mechanisms of laser-matter interactions and ultrafast electron dynamics but also to associate the resulting thermal effects with the surface response. Therefore, there is a growing interest to reveal the physics of the underlying processes from both a fundamental and application point of view.

To this end, we present an extension of the well established theoretical model that describes ultrafast dynamics in semiconductors [93, 104, 110, 131–133], to account firstly, for excitation and electron-phonon relaxation upon heating GaAs with ultrashort pulsed lasers (Section II). To the best of our knowledge, a theoretical investigation of the fundamental multiscale processes has not been performed for GaAs. The theoretical framework is coupled to a module that accounts for the formation of SP-generated LSFL ripples by predicting the laser conditions for the production of sufficiently high density of excited carriers. As the laser conditions of the simulations lead to a phase transition, the role of fluid dynamics in the modulation of the surface profile is briefly explored. Section III explains the details of the numerical algorithm used and the adaptation of the model to GaAs. The details of an experimental protocol that has been developed are given in Section IV while a systematic analysis of results and validation of the theoretical model are presented in Section V by estimating the damage threshold and ripple periodicities. Concluding remarks follow in Section VI.

5.2 THEORETICAL MODEL

5.2.1 *Energy and Particle Balance equations*

During laser irradiation of a semiconducting material, various physical processes occur on a femtosecond timescale. As excitation of GaAs is performed through a laser beam of $\lambda_L = 800nm$ corresponding to photon energy equal to $1.55eV$ that is higher than the band gap of the material ($1.42eV$, at $300K$), it is assumed that one- and two-photon absorption mechanisms are sufficient to excite carriers from the valence to the conduction band while higher order photon processes are less likely to occur. On the other hand, (linear) free carrier photon absorption can increase the electron energy (but not the number of the excited carriers) while Auger recombination and impact ionization processes lead to decrease or increase of the carriers in the conduction band, respectively.

To describe the carrier excitation and relaxation processes, the relaxation time approximation to Boltzmann's transport equation [93, 104, 110, 131–133] is employed to determine the spatial $(\vec{r} = (x, y, z))$ and temporal dependence (t) of the carrier density number, carrier energy and lattice energy; based on this picture the following set of coupled (nonlinear) energy and particle balance equations are used to derived the evolution of the carrier density number N_e, carrier temperature T_c and lattice temperature T_L

$$
\begin{aligned}
C_c \frac{\partial T_c}{\partial t} &= \vec{\nabla} \bullet \left((k_e + k_h) \vec{\nabla} T_c \right) - \frac{C_c}{\tau_e} (T_c - T_L) + S(\vec{r}, t) \\
C_L \frac{\partial T_L}{\partial t} &= \vec{\nabla} \bullet \left(K_L \vec{\nabla} T_L \right) + \frac{C_c}{\tau_e} (T_c - T_L) \\
\frac{\partial N_e}{\partial t} &= \frac{\alpha_{SPA}}{\hbar \omega_L} I(\vec{r}, t) + \frac{\beta_{TPA}}{2 \hbar \omega_L} I^2(\vec{r}, t) - \gamma N_e^3 + \theta N - \vec{\nabla} \bullet \vec{J}
\end{aligned}
\tag{5.1}
$$

where C_c (C_L) is the carrier (lattice) heat capacity, k_e (k_h) is the heat conductivities of the electron (holes), $\hbar\omega_L$ stands for the photon energy ($1.55eV$ for $\lambda_L = 800nm$), α_{SPA} and β_{TPA} correspond to the single and two-photon absorption coefficients, respectively, γ is the coefficient for Auger recombination, θ is the impact ionization coefficient, and τ_e is the carrier-phonon energy relaxation time $\tau_e = \tau_{e0} \left[1 + \left(\frac{N_e}{N_{th}} \right)^2 \right]$,

where $N_{th} = 2 \times 10^{21} cm^{-3}$ and $\tau_{e0} = 500 fs$ [134]. It is noted, that the expression for Si was used to approximately estimate τ_e as there is not any reported relevant value. Through this expression, the significance of carrier density dependence of the relaxation time is recognized. Other quantities that need to be evaluated are the carrier current density $\vec{J}$ and the heat current density $\vec{W}$

$$
\begin{aligned}
S(\vec{r},t) =& (\alpha_{SPA} + \alpha_{FCA}) I(\vec{r},t) + \beta_{TPA} I^2(\vec{r},t) - \vec{\nabla} \bullet \vec{W} \\
& - \frac{\partial N_e}{\partial t}\left(E_g + 3k_B T_e\right) - N_e \left(\frac{\partial E_g}{\partial T_L}\frac{\partial T_L}{\partial t} + \frac{\partial E_g}{\partial N_e}\frac{\partial N_e}{\partial t} \right) \\
\vec{W} =& \left(E_g + 4k_B T_e\right)\vec{J} - (k_e + k_h)\vec{\nabla} T_e \\
\vec{J} =& - D\left(\vec{\nabla} N_e + \frac{N_e}{2k_B T_e}\vec{\nabla} E_g + \frac{N_e}{2T_e}\vec{\nabla} T_e \right) \\
D =& \frac{2k_B T_e}{e}\frac{\mu_e^0 \mu_h^0}{\mu_e^0 + \mu_h^0} \\
C_c =& 3N_e k_B + N_e \frac{\partial E_g}{\partial T_e}
\end{aligned}
\tag{5.2}
$$

where D stands for the ambipolar carrier diffusivity, μ_e^0 and μ_h^0 are the electron/hole mobilities ($8500 cm^2/Vs$ and $400 cm^2/Vs$, respectively, for GaAs [135]) and e is the electron charge (all values of all parameters and coefficients used in this work are presented in Table 5.1). It needs to be emphasized that it was assumed that the carrier system is non-degenerate (it follows a Maxwell-Boltzmann distribution) [131]. Previous reports (for Si) showed that estimation of damage thresholds or carrier density values do not differ significantly if this simplification is ignored [132]. Heat conductivity of the carriers (de-

noted with 'c', where it is 'e' ('h'), for electrons (holes), respectively) is provided by the following expressions

$$\begin{aligned} k_c =& \frac{4k_B^2 T_c \sigma_c}{e} \\ \sigma_c =& eN_c \mu_c^0 \\ N_c =& 2\left[\frac{m^*_{c-cond} k_B T_c}{2\pi\hbar^2}\right]^{3/2} F_{1/2}(\eta_c) \end{aligned} \tag{5.3}$$

where $F_{1/2}(\eta_c)$ are Fermi-Dirac integrals of order ½ (**??**). The approximating values for the first two equations are due to the fact that a Maxell-Boltzmann distribution for the carriers is assumed (non-degeneracy). To compare the electron (hole) conductivity for Silicon and GaAs, we take into account the carrier mobilities μ_c^0 and their optical effective masses for the two materials: $\mu_e^0(GaAs) = 8500cm^2/Vs$, $\mu_h^0(GaAs) = 400cm^2/Vs$, $\mu_e^0(Si) = 1400cm^2/Vs$, $\mu_h^0(Si) = 450cm^2/Vs$, $\mu^*_{e-cond}(GaAs) = 0.067m_e0$, $\mu^*_{h-cond}(GaAs) = 0.34m_e0$, $\mu^*_{e-cond}(Si) = 0.33m_e0$, $\mu^*_{h-cond}(Si) = 0.81m_e0$ [132, 135]. These values yield the following ratios $\frac{k_e(GaAs)}{k_e(Si)} = 0.55$ and $\frac{k_h(GaAs)}{k_h(Si)} = 0.24$ which suggests that the carrier conductivity for GaAs is smaller (or at least of the order) than that of the Si. These results indicate that carrier diffusion does not have a substantial impact on the electron-hole creation as in Si [132]. Thus, the influence of the carrier heat conductivity is ignored (we set, for simplicity $k_e = k_h = 0$) as carrier diffusion has in general, little impact on the creation of electron-hole carriers [131, 132]. This approximation is valid for Silicon and it can be assumed that it holds true for GaAs ([131, 132], given the computed values of k_e, k_h are also smaller than those of Si [136]).

The laser intensity $I(\vec{r}, t)$ in Eqs.(5.1,5.2) is obtained by considering the propagation loss due to one-, two-photon and free carrier absorption, respectively [104]

$$\frac{\partial I(\vec{r}, t)}{\partial z} = -(\alpha_{spa} + \alpha_{FCA}) I(\vec{r}, t) - \beta_{TPA} I^2(\vec{r}, t) \tag{5.4}$$

assuming that the laser beam is Gaussian both temporally and spatially and the transmitted laser intensity at the incident surface is expressed in the following form

$$I(x,y,z=0,t) = \frac{2\sqrt{ln2}E_p(1-R(z=0,t))}{\sqrt{\pi}\tau_p} e^{-\left(\frac{2(x^2+y^2)}{R_0^2}\right)} e^{-4ln2\left(\frac{t-t_0}{\tau_p}\right)^2} \tag{5.5}$$

where E_p is the fluence of the laser beam and τ_p is the pulse duration (i.e. full width at half maximum), R_0 is the irradiation spot-radius (distance from the centre at which the intensity drops to $1/e^2$ of the maximum intensity, and R is the reflectivity while irradiation under normal incidence was assumed.

The computation of the free carrier absorption coefficient and the reflectivity are derived from the dielectric constant of the material (assuming also corrections due to band and state filling [137]), ε',

$$\begin{aligned}\varepsilon' =& 1 + (\varepsilon_{um} - 1)\left(1 - \frac{N_e}{N_v}\right) - \frac{e^2 N_e}{\varepsilon_0 \omega_L^2} \\ &\times \left[\frac{1}{m^*_{e-cond}\left(1 + i\frac{1}{\omega_L \tau_{col}}\right)} + \frac{1}{m^*_{h-cond}\left(1 + i\frac{1}{\omega_L \tau_{col}}\right)}\right]\end{aligned} \tag{5.6}$$

where ε_{un} is the dielectric constant of the unexcited material at $\lambda L = 800nm$ ($\varepsilon_{un} = 13.561 + 0.63105i$) [138], $m^*_{e-cond} = 0.067 m_{e0}$, $m^*_{h-cond} = 0.34 m_{e0}$ are the optical effective masses of the carriers [139] for conductivity calculations, m_{e0} is the electron mass, ε_0 is the permittivity of vacuum, N_v corresponds to the valence band carrier density ($5 \times 10^{22} cm^{-3}$) and $\tau_c ol$ stands for the carriers (electron-hole) collision time. It is noted that optical effective masses are taken to be constant for GaAs and the excitation conditions do not alter them. Similar assumptions were made for Silicon or Germanium that demonstrate that constant values yielded an adequate description of dynamics and morphological effects [93, 104, 108, 131, 132]. The Drude collision time for carriers was assumed to be equal for the two particles (electron and holes), while contribution from only the electron-phonon, hole-phonon and electron-hole collision was considered in the calculation of the total collision frequency of the particles. While the electron-phonon and hole-phonon collision frequencies are assumed to be identical and computed through the empirical expression $A_{eh} T_L$ ($A_{eh} = 1 \times 10^{11} s^{-1} K^{-1}$), the electron-hole collision time is estimated

through the expression (that is valid for a non-degenerate carrier system) [132]

$$1/\tau_{e-h} = \frac{\sqrt{3}\varepsilon_0\pi(k_B T_e)^{3/2}}{2e^2}\left[\frac{1}{m^*_{e-DOS}} + \frac{1}{m^*_{h-DOS}}\right]^{1/2} \tag{5.7}$$

where $m^*_{e-DOS} = 0.067m_{e0}$ and $m^*_{h-DOS} = 0.47m_{e0}$ [139]. In previous reports, it was shown that a transient change of the collision frequency leads to different damage thresholds and therefore influences the thermal response of the material due to produced different energy absorption [132].

Despite estimates in other reports that assume a dynamical variation of τ_{col}[132], for the sake of simplicity, a constant value, $\tau_{col} \sim 10fs$ is assumed in the simulations as for Si [108]. The reflectivity and free carrier absorption coefficients are given by the following expressions (i.e. for a flat surface)

$$\begin{aligned} \alpha_{FCA}(x,y,z,t) =& \frac{2\omega_L k}{c} \\ R(x,y,z=0,t) =& \frac{(1-n)^2+k^2}{(1+n)^2+k^2} \end{aligned} \tag{5.8}$$

where c stands for the speed of light while n and k are the refractive index and extinction coefficient of the material, respectively. By contrast, reflectivity for a non-flat profile depends on the corrugation of the morphology and it denoted by $R(x,y,surface,t)$ (computation of $R(x,y,surface,t)$ is described in Section III) while Eq.5.5 is replaced with

$$I(x,y,surface,t) = \frac{2\sqrt{ln2}E_p\left(1-R(x,y,surface,t)\right)}{\sqrt{\pi}\tau_p} \\ e^{-\left(\frac{2(x^2+y^2)}{R_0^2}\right)} e^{-4ln2(\frac{t-t_0}{\tau_p})^2} \tag{5.9}$$

5.2.2 *Surface Plasmon Excitation*

As explained in the Introductory section, the excitation of SP and its interference with the incident beam constitute one of the dominant mechanisms that aim to explain the formation of LSFL [93, 107, 108, 140, 141]. Nevertheless, coupling of the incident beam with SP modes

is possible only if there is an initial corrugation (for example, surface defects [93]) or via index matching [140] and grating coupling [142]. Due to an inhomogeneous deposition of the laser energy on the semiconductor as a result of the exposure to a linearly polarized Gaussian-shape beam, the surface of material is not expected to be perfectly smooth after resolidification following irradiation with $NP = 1$ (crater [93]); hence, further irradiation of the non-planar profile will give rise to a SP which is capable to couple with the incident beam yielding a resultant periodically modulated intensity ($\sim exp(i\vec{k}_s \bullet \vec{r})$) [93] $I_{total}(\vec{r}, t) = \left\langle \left| \vec{E}_{incident} + \vec{E}_{SP} \right|^2 \right\rangle$ [93, 143].Thus, form this expression, it is evident that the interference of the incident and the surface waves (SP) leads to a periodically modulated intensity profile.

According to theoretical predictions and experimental studies, the interference of the incident and the surface wave results in the development of periodic ripples (LSFL) with orientation *perpendicular* to the electric field of the laser beam [88–100]; this is generated, firstly, by the development of the aforementioned spatially periodic energy distribution that yields a periodic distribution of the electron temperature field. Upon relaxation due to electron-phonon scattering, the characteristic spatial modulation will be projected on the lattice system and fluid dynamics (when the material undergoes a phase transition) leading eventually to a rippled profile when the resolidification process ends.

The dispersion relation for the excitation of SP is derived by the boundary conditions (continuity of the electric and magnetic fields at the interface between a metallic and dielectric material) ($\varepsilon_d = 1$)for a flat surface ($NP = 1$). Therefore, a requirement for a semiconductor to obey the above relation and conditions [93, 140] is that $Re(\varepsilon') < -1$ and the computed SP wavelength λ_S is given by

$$\lambda_S = \frac{\lambda_L}{Re\sqrt{\left(\frac{\varepsilon'\varepsilon_d}{\varepsilon'+\varepsilon_d}\right)}} \tag{5.10}$$

The condition $Re(\varepsilon') < -1$ and Eqs.(5.6,5.10) can be used to derive the range of values of the excited carrier densities that lead to SP excitation. It is evident that carrier densities larger than $\sim 1.5 \times 10^{21} cm^{-3}$ lead to excitation of SP (Fig.5.1). Although, Eq.(5.10) can be used to calculate the SP and, eventually, the ripple periodicity, there exists a discrepancy between the experimental observations and theoretical prediction. More specifically, special attention is required

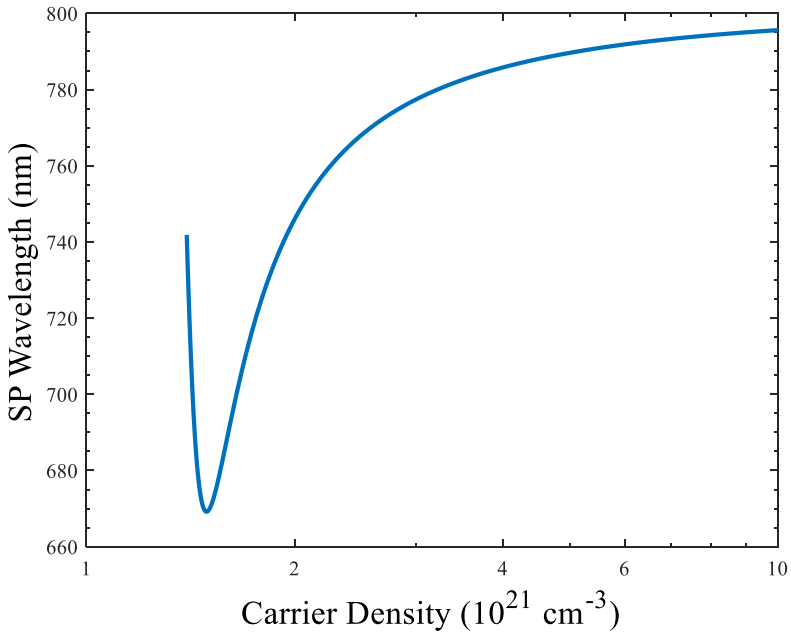

Figure 5.1: Surface plasmon wavelength as a function of the excited carrier densities when the SP excitation condition is satisfied.

when the surface profile changes from a flat to a periodically corrugated one. Previous studies reported that a systematic analysis of the distribution of the electric field of the laser beam shows that there exists a correlation of the SP wavelength with the depth of the periodic structure that leads to the best SP-laser coupling and therefore Eq.5.10 is no longer valid [90, 97, 144](see discussion in Sections III, V).

As pointed out above, although Eq.8 indicates the SP excitation condition for NP=1, a coupling of the SP with the incident beam requires a corrugation/defect on the surface; given that for NP=1, a corrugation is not present, an interference between a SP and the incident beam is not possible and therefore ripples cannot be produced. By contrast, the modified profile (following surface modification after NP=1) produces the initial corrugation required to both excite SP and induce coupling with the incident beam [145]. This will lead to the required inhomogeneous energy deposition that eventually leads to a periodic structure formation [91, 93, 109] through a periodic modulation of the intensity (Sections III, V).

5.2.3 *Fluid Dynamics and material removal*

Due to the evident need for the introduction of a phase transition for the description of an induced morphological change, fluid dynamics is introduced. The material that undergoes melting is assumed to be an incompressible Newtonian fluid and its dynamics is described by the following equations [93]:

(i). for the mass conservation (incompressible fluid):

$$\vec{\nabla} \bullet \vec{u} = 0 \tag{5.11}$$

(ii). for the energy conservation:

$$C_L^{(m)} \left[\frac{\partial T_L^{(m)}}{\partial t} + \vec{\nabla} \bullet \left(\vec{u} T_L^{(m)} \right) \right] = \vec{\nabla} \bullet \left(K_L^{(m)} \vec{\nabla} T_L^{(m)} \right) \tag{5.12}$$

where $(K_L^{(m)})$ is the thermal conductivity of the molten material. The presence of a liquid phase requires a modification of the second of Eq.5.1 to incorporate heat convection. This means that while the second equation in Eq.5.1 that describes the lattice temperature evolution still holds for material which is in the solid phase, an appropriate modification is required to account for the transport/convection of the fluid [93]. Furthermore, an additional term with a δ-function is presented in the equation to describe a smooth transition from the liquid to solid phase

$$C_L^{(m)} \left[\frac{\partial T_L^{(m)}}{\partial t} + \vec{\nabla} \bullet \left(\vec{u} T_L^{(m)} \right) \right] - L_m \delta \left(T_L^{(m)} - T_m \right) \frac{\partial T_L^{(m)}}{\partial t} = \vec{\nabla} \bullet \left(K_L^{(m)} \vec{\nabla} T_L^{(m)} \right) \tag{5.13}$$

(iii). for the momentum conservation:

$$\rho_L^{(m)} \left(\frac{\partial \vec{u}}{\partial t} + \vec{u} \bullet \vec{\nabla} \vec{u} \right) = \vec{\nabla} \bullet \left(-P + \mu \left(\vec{\nabla} \vec{u} \right) + \mu \left(\vec{\nabla} \vec{u} \right)^T \right) \tag{5.14}$$

where $\vec{u}$ is the velocity of the fluid, μ is the liquid viscosity, P is the total pressure (hydrodynamical and recoil) and $C_L^{(m)}$ stands for the heat capacity of the liquid phase. Vapour ejected creates a back (recoil) pressure on the liquid free surface which in turn pushes the

melt away in the radial direction. The recoil pressure and the surface temperature are usually related according to the equation [146, 147]

$$P_r = 0.54 P_0 exp\left(L_v \frac{T_L^S - T_b}{R T_L^S T_b} \right) \tag{5.15}$$

where P_0 is the atmospheric pressure ($\sim 10^5 Pa$), L_v is the latent heat of evaporation (of the order of $10^7 kJ/m^3$ as for Silicon and Germanium [148]), T_b stands for the boiling temperature, R is the universal gas constant, and T_L^S corresponds to the surface temperature. The surface tension in pure molten GaAs decreases with growing melt temperature (Table 5.1), which causes an additional depression of the surface of the liquid closer to the maximum value of the beam while it rises elsewhere. Hence, spatial surface tension variation induces stresses on the free surface and therefore a capillary fluid convection is produced. Thus, a surface tension related pressure is derived, P_σ which is expressed as $P_\sigma \sim \sigma$.

(iv) shallow water equations:

Due to the phase transition, the dynamics of the molten material will determine the surface profile when solidification terminates. Thus, the generated ripple height is calculated from the Saint-Venant's shallow water equation [149]

$$\frac{\partial H(\vec{r},t)}{\partial t} + \vec{\nabla}\left(H(\vec{r},t)\vec{u}\right) = 0 \tag{5.16}$$

where $H(\vec{r},t)$ stands for the melt thickness which evolves and provides the final surface morphology upon resoldification.

The presence of an intermediate zone that contains material in both phases when the solid undergoes a phase transition will complicate the description of flow dynamics (presence of a mushy zone [150]). Nevertheless, to avoid complexity of the solution of the problem and given the small width of the two phase region with respect to the size of the affected zone a different approach will be pursued where a mushy zone is neglected and transition from to solid-to-liquid is indicated by a smoothened step function of the thermophysical quantities. In previous reports, the role of the recoil pressure and critical temperatures were also taken into account to model ablation (material removal) conditions [93] (i.e. boiling [98] or critical point

of the material [93] yielding a lattice temperature of the order of $\sim (2.5-3) \times T_{melt}$ or equivalently $\sim 0.90\ T_{critical}$ (see [93, 151–153] and [136]). However, in the current work, due to the lack of knowledge of relevant parameters and for the sake of simplicity, a lattice temperature of the material equal to approximately $3 \times T_{melt}$ is assumed to lead to the onset of mass removal. Furthermore, T_b is taken to be equal to $\sim 2.5 \times Tmelt$ (approximately similar to the experimentally confirmed relation for Silicon or Germanium).

5.3 NUMERICAL SOLUTION

Due to the inherent complexity and highly nonlinear character of the equations in Section II, an analytical solution is not feasible and therefore, a numerical approach is pursued. Numerical simulations have been performed using a finite difference method while the discretization of time and space has been chosen to satisfy the Neumann stability criterion. Furthermore, it is assumed that on the boundaries, von Neumann boundary conditions are satisfied and heat losses at the front and back surfaces of the material are negligible. The initial conditions are $T_e(t=0) = T_L(t=0) = 300K$, and $N_e = 10^{12} cm^{-3}$ at $t = 0$. The parameters for GaAs used in the simulation are summarized in Table 5.1.

The values of the laser beam used in the simulation are: The (peak) fluence is $E_p\Big(\equiv \sqrt{\pi}\tau_p I_0 / \left(2\sqrt{ln2}\right)\Big)$, where I_0 stands for the peak value of the intensity while R_0 in Eq.5.5 is taken to be equal to $20\mu m$. The wavelength of the beam is $\lambda_L = 800nm$. A common approach followed to solve similar problems is the employment of a staggered grid finite difference method which is found to be effective in suppressing numerical oscillations. Unlike the conventional finite difference method, temperatures (T_c and T_L), carrier densities (N_e), pressure (P) are computed at the centre of each element while time derivatives of the displacements and first-order spatial derivative terms are evaluated at locations midway between consecutive grid points. Similarly, the carrier density $\vec{J}(x,y,z,t)$ and the heat carrier density $\vec{W}(x,y,z,t)$ are evaluated at the above locations rather than at the centres of each element. On the other hand, the horizontal and vertical velocities are defined in the centres of the horizontal and vertical cells faces, respectively (for a more detailed analysis of the numerical simulation conditions and the methodology towards the description of fluid dynamics, see Ref.[93]). It is also assumed that, for $NP = 1$, $\vec{J}(z=0,t)$ and $\vec{W}(z,t)$ at the front ($z = 0$) or the other end of the irradiated region

($z = 10\mu m$) vanish. By contrast, for $NP > 1$ (for which the surface profile is modified), some modification is required: For irradiation with $NP > 1$, the incident beam is not always perpendicular to the modified profile, therefore the surface geometry influences the spatial distribution of the deposited laser energy. For example, the laser irradiation reflected from the profile slopes can lead to light entrapment between the formed structures. Similarly, energy absorption is altered if incident beam irradiates at zero or different angle and therefore energy absorption varies on the slopes. Typical Fresnel equations are used to describe the reflection and transmission of the incident light. Due to a potential multiple reflection, absorption of the laser beam is also modified [154] and thereby a ray tracing method is employed to compute the absorbed power density while a similar methodology is ensued to estimate the proportion of the refraction by applying Snell's law. With respect to the numerical scheme used to simulate dynamics of velocity and pressure fields, a similar procedure is ensued in the event of subsequent pulses, however in this case the interaction with the modified surface profile induced by the first pulse due to the hydrodynamic motion of the molten material and its subsequent resolidification, should be taken into account. While second order finite difference schemes appear to be accurate for $NP = 1$ where the surface profile has not been modified substantially, finer meshes and higher order methodologies are performed for more complex and profiles [155, 156]. By taking into account the above, in corrugated surfaces Eq.5.9 instead of Eq.5.5 is used.

Regarding the boundary conditions for the fluid dynamics, the following constraints are imposed:

1. $\vec{u} = 0$, on the solid-liquid interface (non-slipping conditions),
2. $\mu \dfrac{\partial \vec{u}}{\partial z} = \dfrac{\partial \sigma}{\partial T_s} \dfrac{\partial T_s}{\partial \vec{r}}\Big|_{\vec{r}\ on\ surface}$, on the top surface ($T_s$ is the surface temperature and σ stands for the surface tension),). Its gradient along the tangential direction is balanced by shear stress (the position vector, $\vec{r}$,is taken on the surface of the molten profile),
3. $P = 0$, on the top surface.

Numerical integration is allowed to move to the next time step provided that all variables at every element satisfy a predefined convergence tolerance of $\pm 0.1\%$. To simplify the solution procedure, it is noted that hydrodynamic equations are solved in regions that contain either solid or molten material. To include the 'hydrodynamic'

effect of the solid domain, material in the solid phase is modelled as an extremely viscous liquid ($\mu_{solid} = 10^5\mu$), which will result into velocity fields that are infinitesimally small. An apparent viscosity is then defined with a smooth switch function similar [93] to emulate the step of viscosity at the melting temperature. Resolidification is considered when the lattice temperature of the molten material drops below T_{melt}. With respect to the material removal part of the simulation, lattice and carrier temperatures are computed over time and if lattice temperature reaches $\sim T_{rem}$, mass removal is assumed [93, 153]. In that case, the associated nodes on the mesh are eliminated and new boundary conditions of the aforementioned form on the new surface are enforced. In order to preserve the smoothness of the surface that has been removed and allow an accurate and non-fluctuating value of the computed curvature and surface tension pressure, a fitting methodology is pursued.

5.4 EXPERIMENTAL PROTOCOL

A TiSapph regenerative amplifier laser was used with central wavelength at $800nm$, at $1kHz$ repetition rate, of $100fs$ pulse duration and $5mJ$ pulse energy. The laser beam was guided through an optical microscope setup onto a SI-GaAs substrate. A pyroelectric sensor was used to measure the power at the sample surface ($\sim 200mJ/cm^2$). The irradiation took place in room conditions at $101.325kPa$ ($1atm$). A two dimensional high precision translation stage was used to move the sample with spatial resolution of $1\mu m$. The sample was fixed on a two axis translation stage that was set to move at a constant velocity equal to $300\mu m/s$ perpendicularly to the laser beam direction. By setting the repetition rate of the laser at $1kHz$ and the beam spot size of $4.24\mu m$ on the focal plane of the surface, each point of the material was irradiated by 14 pulses (on average). The beam moved relatively to the sample in a zig-zag motion scanning a square area of $50\mu m \times 50\mu m$. On the sample shown in Fig.5.2, the laser beam is scanning along the x- direction but making small steps on the y-direction. The y-step length is selected to match the ablation spot diameter velocity with a constant pulse repetition rate of $1KHz$, causing overlap of each ablation spot. From shot to shot the overlap is calculated to 93%. The time scale of dynamics investigated in these experiments ($> 50ps$) is much shorter than the delay between consecutive pulses ($1ms$ for $1KHz$ lase amplifier system). For every repetition, the fluence for each pulse has an isolated effect and is not influenced by the next pulse but instead

Solid phase

Quantity	Symbol (units)	Value
Initial temperature	$T_0(K)$	300
Electron-hole pair heat capacity[157]	$C_c(J/m^3K)$	$3 \times 10^{18} N_e k_B$
Lattice heat capacity[158]	$C_l(J/m^3K)$	$(3.235 \times 10^5 + 52.81 T_L - 1.48 \times 10^9 T_L^{-2})\rho_L$
Lattice heat conductivity[159]	$K_l(W/mK)$	$7.1 \times 10^4 \times T_L^{-1.25}$
Band-gap energy[160]	$E_g(J)$	$2.4337 \times 10^{-19} - 8.6646 \times 10^{-23} T_L^2/(T_L + 204)$
Interband absorption (800 nm)[161]	$\alpha_{SPA}(m^{-1})$	$2.91 \times 10^6 \times \exp\left[3.22(1.184 - Eg(T_L))\right]$
Two-photon absorption (800 nm)[162]	$\beta_{TPA}(m/W)$	1×10^{-9}
Auger recombination coefficient[163]	$\gamma(m^6/sec)$	1.1×10^{-43}
Impact ionization coefficient[104]	$\delta(sec^{-1})$	$3.6 \times 10^{10} \exp(-1.5 E_g/k_B T_e)$
Energy relaxation time[134]	$\tau_e(sec)$	$\tau_{e0}\left[1 + \left(\frac{N_e}{N_{cr}}\right)^2\right]$, $\tau_{e0} = 0.5ps$, $N_{cr} = 2 \times 10^{27} m^{-3}$
Complex dielectric function[164]	ε	$13.561 + 0.63105i$
Free electron rest mass[165]	$m_0(gr)$	9.11×10^{-28}
Effective mass for density of states[165]		
Electrons	$m^*_{e,DOS}/m_0$	0.067
Holes	$m^*_{h,DOS}/m_0$	0.47
Effective mass for conductivity[165]		
Electrons	$m^*_{e,cond}/m_0$	0.067
Holes	$m^*_{h,cond}/m_0$	0.34

Molten phase

Quantity	Symbol (units)	Value
Lattice heat capacity[166]	$C_L(J/m^3K)$	$0.46\rho_L$
Lattice heat conductivity [167]	$K_l(W/mK)$	$7.54 \times 10^4 \left(T_L^{(m)}\right)^{-1.29}$
Density[167]	$\rho_L(gr/m^3)$	$-8.2917 \times 10^{-3}\left(T_L^{(m)}\right)^2 - 85.624\left(T_L^{(m)}\right) + 5.3429 \times 10^6$
Dynamic viscosity[168]	$\mu(gr/msec)$	$f(T_L^{(m)}) = p1\left(T_L^{(m)}\right)^3 + p2\left(T_L^{(m)}\right)^2 + p3\left(T_L^{(m)}\right) + p4$ $p1 = -3.717 \times 10^{-17}$ $p2 = 1.569 \times 10^{-3}$ $p3 = -2.208, p4 = 1036$
Surface tension[169]	$\sigma(N/m)$	$0.401 - 0.18 \times 10^{-3}(T_L^{(m)} - T_{melt})$, for $T_L < 1610K$[169] $0.5821\left(T_L^{(m)}\right)^3 - 6.8871 \times 10^{-5}\left(T_L^{(m)}\right)^2$ $-4.7281 \times 10^{-8} T_L^{(m)}$ $+7.5591 \times 10^{-12}$, for $1610K < T_L < 3T_{melt}$ [136, 169]
Energy relaxation time[104]	$\tau_E(sec)$	10^{-12}
Melting temperature	$T_{melt}(K)$	1511
Latent heat of melting (fusion)[167]	$L_{melt}(J/m^3)$	3.783×10^9

Table 5.1: Optical and material parameters of GaAs

the sum of pulses has an accumulative effect on the reshaping of the geometry of the surface.

A parametric analysis was performed by varying the scanning velocity, the beam overlapping area of ablation and fluence relative to the scanning direction. Since comparison of results as a function of scanning velocity is not convenient, the scanning velocity is converted to the number of pulses per spot through the relation with the laser repetition rate (hence only the NP is used in this work and not the scanning velocity). To characterize the produced surface profiles, a SEM was used (Fig.5.2a). A Two-Dimensional Fourier Transform (2DFT) was applied, to measure the spatial frequency of the ripples in a zoomed area of dashed box on the ablated sample (Fig.5.2b). It is illustrated that the ripples are orientated perpendicularly to the linear polarization of the laser beam for a linearly polarized (p-polarized) beam. In the 2DFT plot Fig.5.2c, three spatial frequencies are identified. The lowest frequencies around zero in the middle of the graph, correspond to patterns with low to no periodicity or noise. By contrast, the frequencies around $\pm 1.6 \mu m^{-1}$ correspond to periodic structures related to LIPSS. Finally, the highest frequencies are related with the side edges, two in each ripple, thus the double spatial frequency compared to the main body and image noise patterns ([136]). Those frequencies are not predicted by the SP model. The areas containing the spatial frequencies of the LIPSS are plotted by performing in inverse Fourier transform to identify the ripple formation position (Fig.5.2d). The 2DFT analysis and the bandwidth of the spatial frequencies of LIPSS yield a dispersion of the ripple periodicities in a range between $550nm$ and $680nm$. In this Fig.5.3, a 2DFT was applied as in Fig.5.2 in the main manuscript . However, instead of plotting the spatial frequency at $\pm 1.6 \mu m^{-1}$, an inverse Fourier transform was applied at $\sim \pm 3.2 \mu m^{-1}$ to verify that the area with double the frequency of the ripples belongs to the edges of the ripples. More specifically, in (a) the area where 2DFT is applied is illustrated in (b) is the Fourier transform and the power spectrum taken from the area in the white dashed box. In (c) is the inverse Fourier transform from the red dashed box in (b). In (d) we have overlapped (c) in red color on top of (a), to make clear the distinction of the points that define spatial frequencies of the 2DFT are at $\sim \pm 3.2 \mu m^{-1}$.

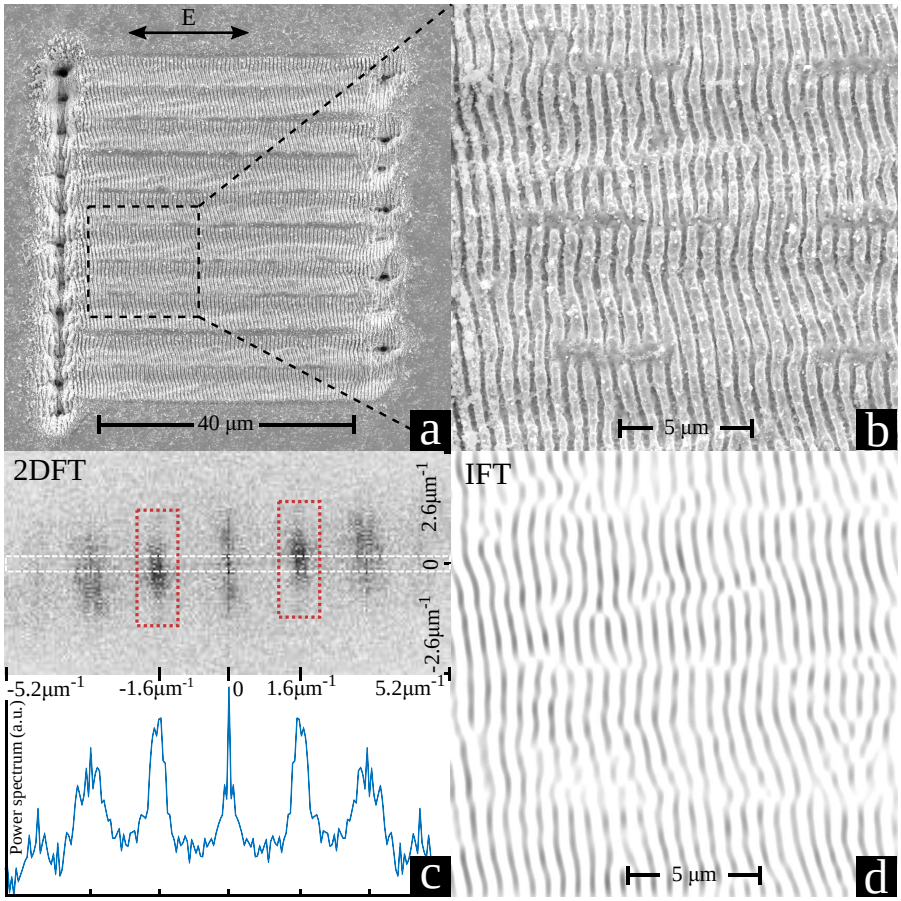

Figure 5.2: SEM image of the laser ablated surface of GaAs sample and analysis: (a) complete view of the scanned area($\vec{E}$ stands for the laser beam polarization), (b) zoomed area of (a),(c) 2D Fourier transform of the area in (b), (d) inverse Fourier transform from the areas in (c) red boxes at $\pm 1.6 \mu m^{-1}$ generating a rippled region with periodicities in a range between $550nm$ and $680nm$. ($E_p = 200mJ/cm^2$, $\tau_p = 100fs$, $NP = 14$).

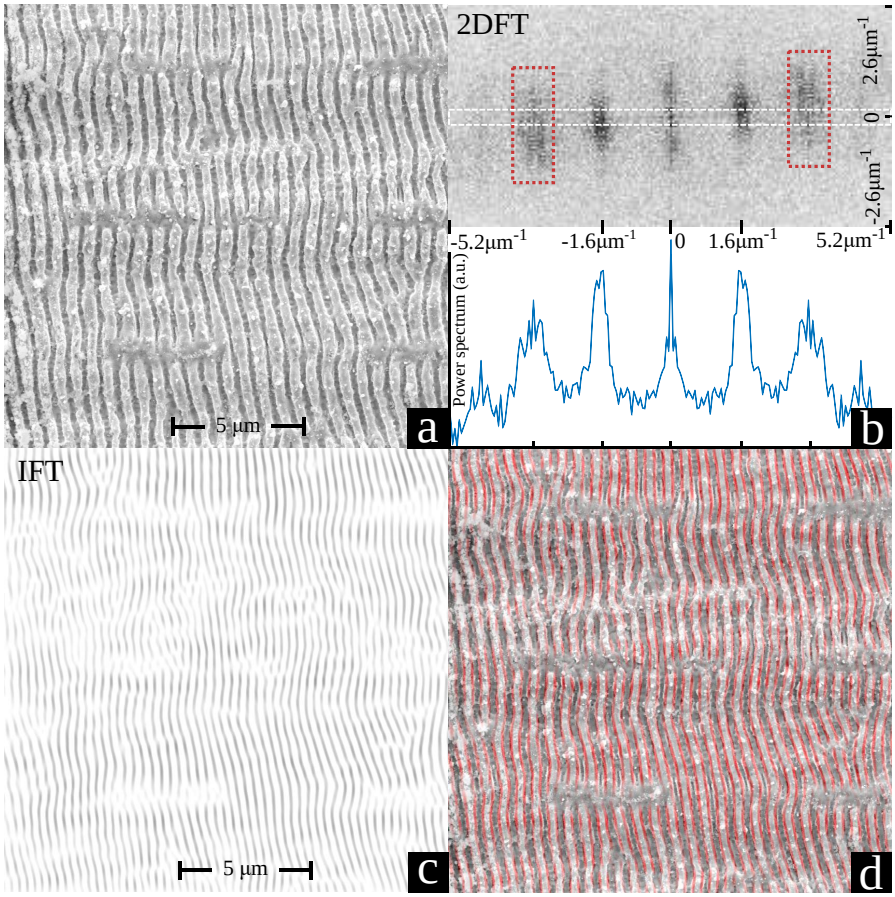

Figure 5.3: SEM image and analysis of the inverse Fourier transform on the $\sim \pm 3.2 \mu m^{-1}$ frequencies to verify that the area with double the frequency of the ripples belongs to the edges of the ripples.

5.5 RESULTS AND DISCUSSION

5.5.1 *Ultrafast Dynamics and SP excitation*

The ultrafast dynamics and the thermal response of the heated material are investigated to take into consideration the role of fluence and the pulse duration. Firstly, laser conditions for irradiation of GaAs with a single pulse of fluence $E_p = 70mJ/cm^2$ and pulse duration $\tau_p = 100fs$ are assumed. The evolution of the carrier density and the carrier and lattice temperatures are illustrated in Fig.5.4. Similar to results for Si, the behaviour in the nonequilibrium regime is due to the difference between the temporal scales of the pulse duration and the electron-phonon relaxation times [93, 103, 108, 131, 132]. The carrier temperature remarkably increases during the first moments of irradiation (see inset in Fig.5.4) due to the fact that the heat capacity of the carrier system is several orders of magnitude larger than that of the lattice. The main processes of energy gain of the electron system through a (linear) one-photon and free carrier energy absorption. Following a short period when the carrier system does not further increase its energy, Tc rises rapidly as the available pulse energy increases. To explain the initial increase followed by a slightly decreasing carrier temperature (*clamped region*) that occurs before the amount of the absorbed energy becomes significant which, subsequently, leads to a rapid rise of Te, one has to examine the contribution of the competing mechanisms indicated by the various components in the '*source term*' (Eq.5.2). As demonstrated for Silicon [93, 104, 131, 132], fluence plays a very significant role in the shape of the T_e curve. More specifically, at lower fluences (Fig.2a in Ref [136]), there is initially, a small amount of electron-hole pairs that leads to a small carrier heat capacity. As a result, Eq.5.2 yields a noticeable increase of T_e which continues until (i) the energy absorption is large enough to generate a sufficient amount of carriers, and (ii) the energy loss due to a pronounced thermal transfer from the carriers to the lattice. The increase of these two factors lead to a decrease of the thermal energy of the carriers that is also reflected from the decrease of T_e (i.e. due to the increase of the relevant terms in Eq.5.2). On the other hand, larger fluences produce larger amounts of carriers and (given the fact that one photon-absorption and Auger recombination are the two predominant factors that alter carrier density), Auger recombination becomes significantly important as it varies as N_e^3. Hence, the enhanced Auger recombination (Fig.2b in Ref [136]) converts carrier ionization energy into kinetic energy that results into an increase of the carrier temperature before it starts

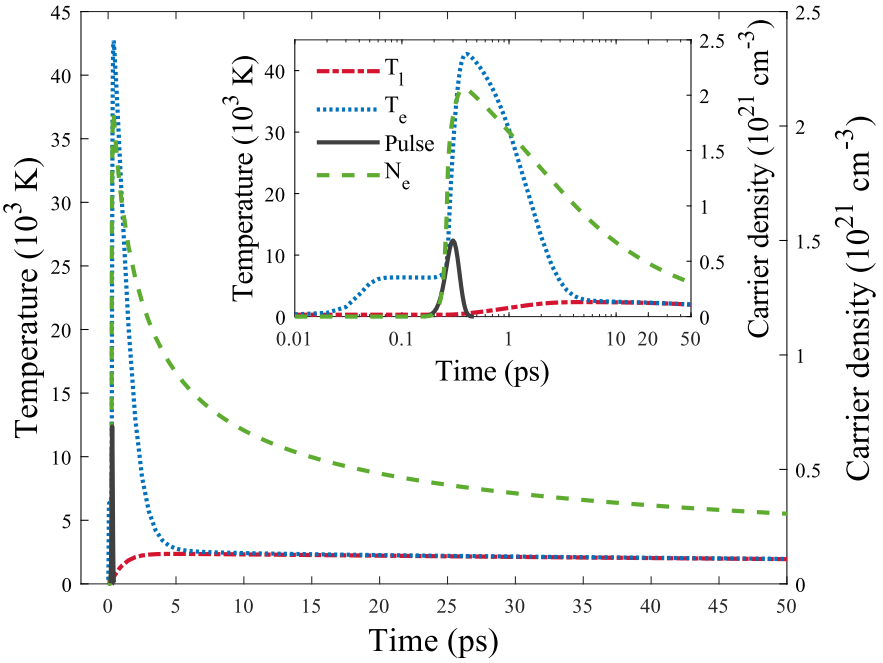

Figure 5.4: Evolution of the carrier density, electron and lattice temperatures at $x = y = z = 0$ ($E_p = 70mJ/cm^2$, $\tau_p = 100fs$).

falling again. Therefore, for moderate values of fluence, a two peak structure of T_e is shown. Finally, at even larger fluences (used in these simulations), the first peak almost disappears yielding a slow decrease (*clamped region*) before a much higher peak is produced that occurs after the carrier density has reached its peak (Fig.5.4).

It is evident around the time the pulse yields the peak intensity, the carriers acquire their highest energy and in that case, two-photon and free carrier absorption processes have a significant influence. The increase of the carrier energy even after the time at which their density has reached its maximum is due to the free carrier absorption.

After the carriers reach the highest energy, their temperature start to decrease mainly because of their interaction with the lattice while Auger recombination delays the heating of the lattice. On the other hand, the decrease of the carrier density is caused by the Auger recombination effect (Fig.5.4). It is noted that Te attains very high values and this could potentially influence the energy band gap response. Nevertheless, the adequate description of carrier dynamics and thermal response of Silicon [93, 104, 131, 132] by ignoring a dramatic change in the band gap for large T_e indicates that the influence of very energetic carriers is insignificant to E_g. Therefore, even for GaAs, a T_L-

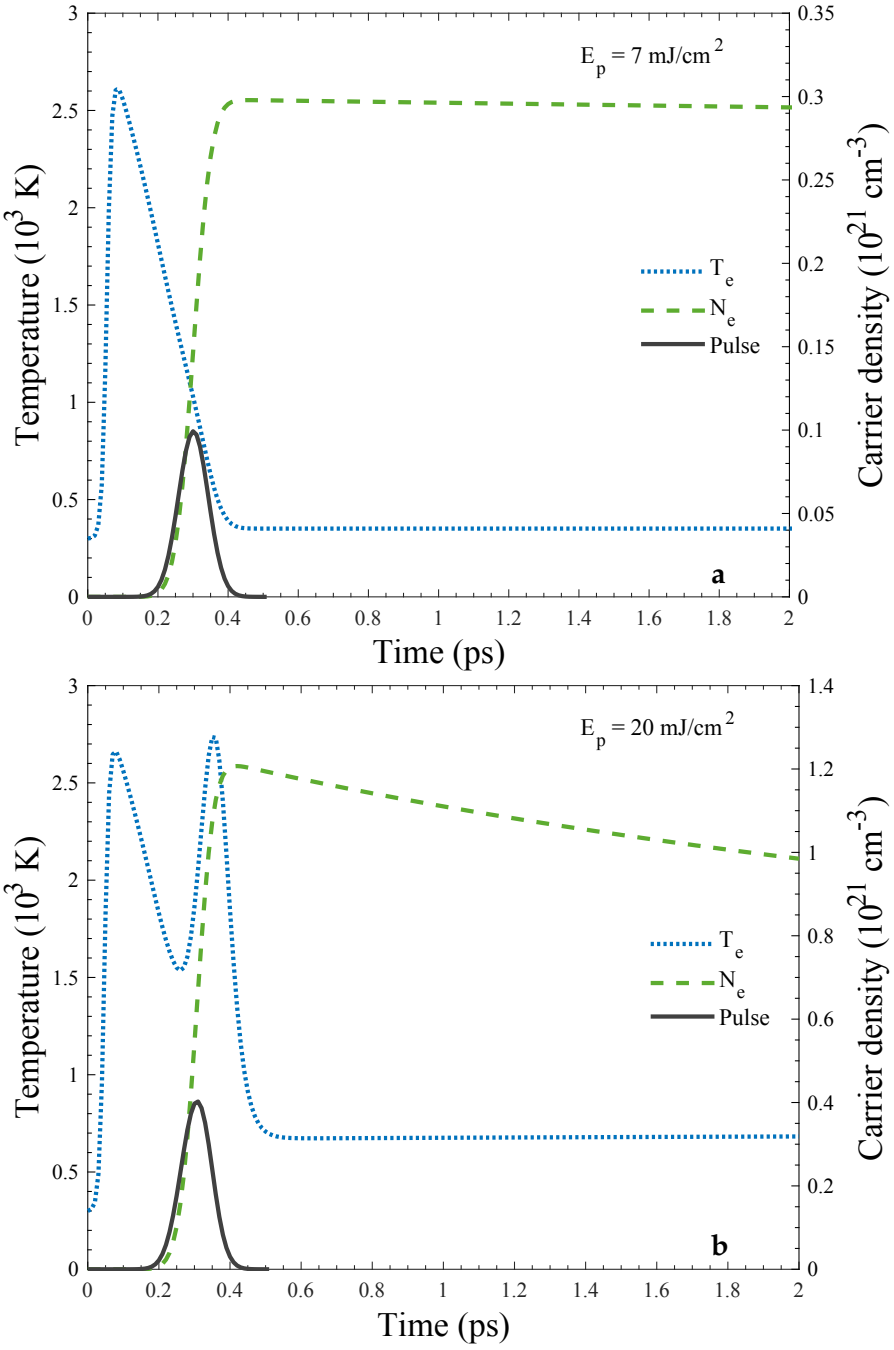

Figure 5.5: Evolution of the carrier density and electron and lattice temperatures at $x = y = z = 0$ for (a) $E_p = 7mJ/cm^2$ and (b) $E_p = 20mJ/cm^2$ ($\tau_p = 100fs$). The black curve indicates the temporal shape of the pulse.

dependence is assumed regardless of the magnitude of T_e. Certainly, a more rigorous approach (e.g. based on first principles) should also be considered to estimate a possible E_g variation for large T_e.

The reflectivity of the irradiated material drops rapidly within the pulse duration to a minimum value that corresponds to $Re(\varepsilon) = 1$ (Fig.5.6) (see also Ref. [137]) before it starts rising as the density of the excited carriers increases sharply. The Auger recombination related decrease of Ne leads to a gradually relaxation of reflectivity towards the initial value of the unexcited material. On the other hand, Fig.5.6 shows that the density becomes large enough to satisfy the criterion for excitation of SP (i.e. $Re(\varepsilon) < -1$). Furthermore, the steep increase of the reflectivity around the 'metallisation' of the material (i.e. $Re(\varepsilon) = 0$) is demonstrated in Fig.5.6. The metallic behavior is also followed by a phase transition the material undergoes (i.e. melting).

To illustrate the effect of fluence on the optical properties of the irradiated material and the induced energy absorption that is expected also to influence the thermal response of the system (and equilibration process) as well its surface morphology, the evolution of reflectivity is investigated for various values of E_p. Simulation results indicate that there exists a faster acquisition of the minimum value (shift of the minimum to smaller times in Fig.5.7a) which is attributed to the generation of an increased number of carriers at higher fluences. Unlike the behavior for small values, at larger fluences the reflectivity increases abruptly (around $Re(\varepsilon) = 0$ as seen in Fig.5.7a demonstrating a metallic behaviour). The variation of fluence not only

influences the temporal evolution of the reflectivity but also its absolute maximum change from the initial value at $t = 0$, $\mathbb{R}$. It is shown (Fig.5.7b) that $\mathbb{R}$ which is taken to be around the moment of phase transition ($t \sim 350fs$) decreases for small values of the laser fluence while it increases at larger E_p (where the metallic behaviour is more pronounced.

On the other hand, the role of both the fluence and the pulse duration in the response of the dielectric constant is illustrated in Fig.5.8. More specifically, it is evident that the real part of the dielectric constant drops at increasing fluence for a specific τ_p. To interpret the results, it is noted that when the semiconductor is in an unexcited state, the condition $Re(\varepsilon) > 0$ holds (despite the dielectric constant is dependent on the laser wavelength, this condition is always valid). As the carrier density increases, the material moves to the 'metallic' regime. Therefore, higher energies are expected to allow the resonance condition (i.e. $Re(\varepsilon) = 0$) to be met easier as unlike a small absorption efficiency at small intensities, energy absorption is more pronounced

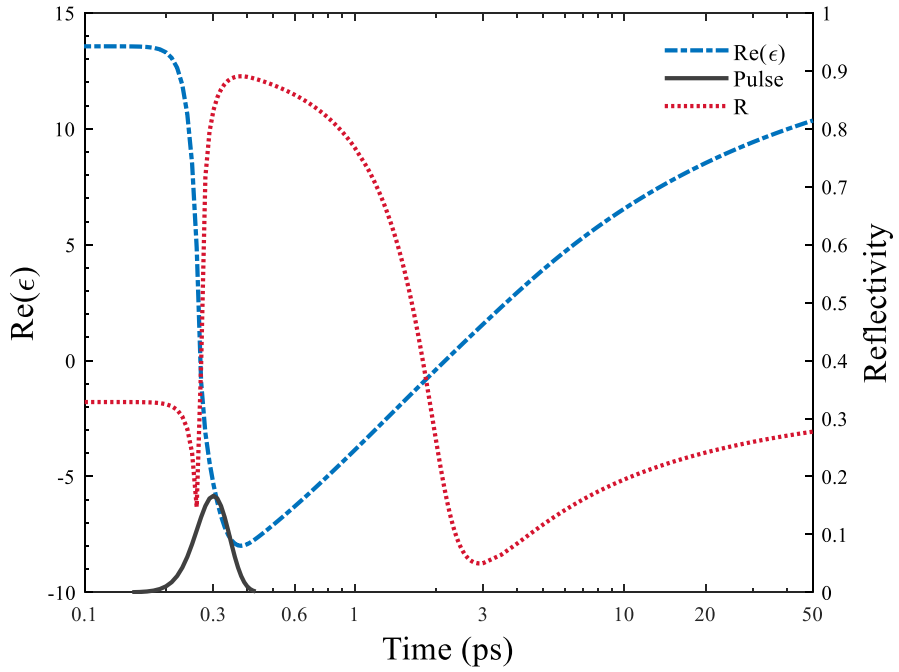

Figure 5.6: Evolution of the real part of the dielectric constant at $x = y = z = 0$. ($E_p = 70mJ/cm^2$, $\tau_p = 100fs$).

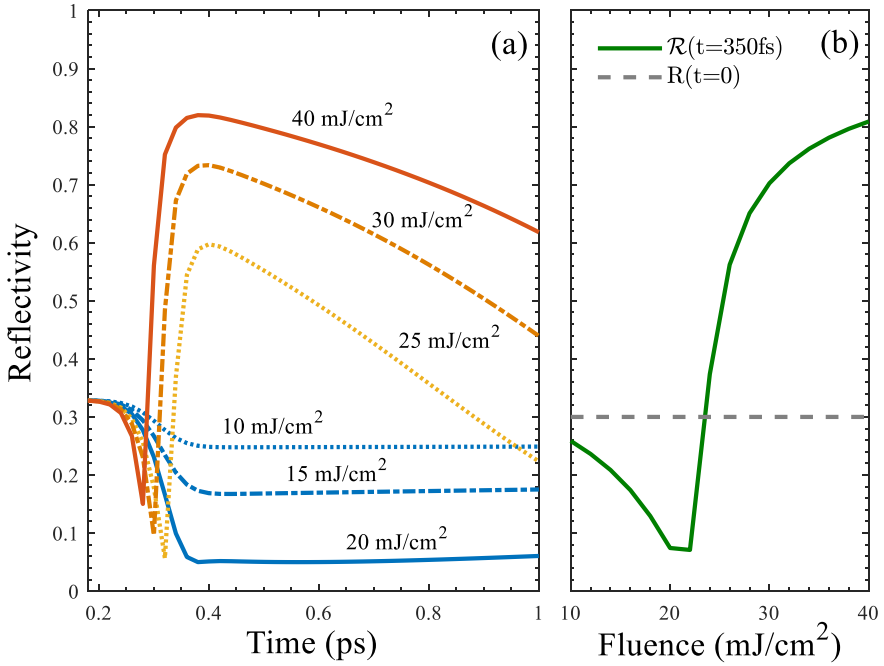

Figure 5.7: (a) Reflectivity evolution at various fluences at $z = 0$ ($\tau_p = 100fs$), (b) Absolute value of the difference between the maximum change of reflectivity from the initial value, $\mathbb{R}$, as a function of fluence.

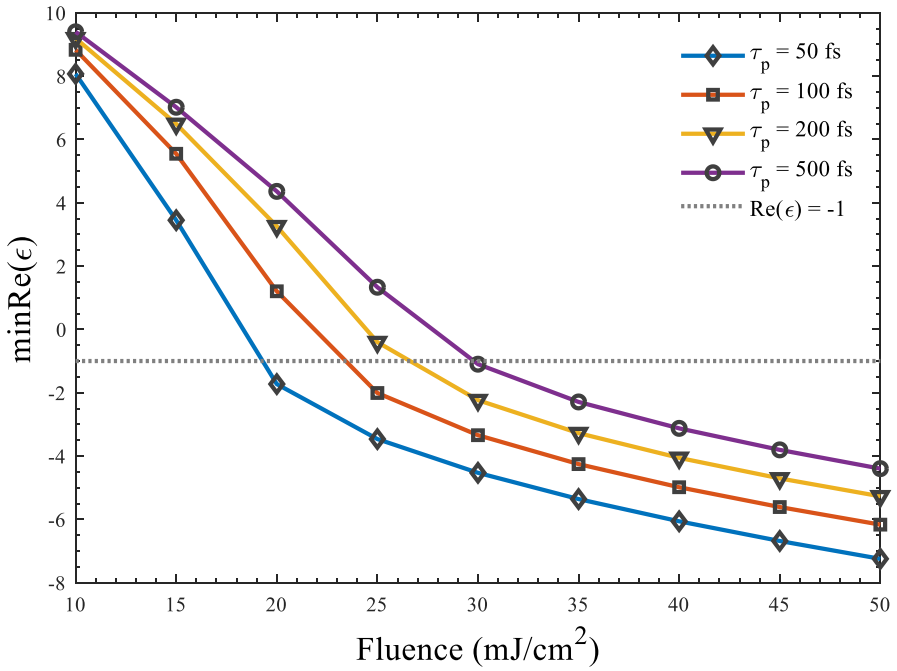

Figure 5.8: Dependence of the minimum value of the real part of the dielectric constant as a function of fluence for various values of the pulse duration.

due to a significant contribution of multi-photon-assisted excitation [108]. Similarly, keeping the fluence constant, a higher energy absorption is achieved when the temporal width of the pulse is smaller which results in an enhanced density of excited carriers. In Fig.5.8, it is shown that the laser conditions suffice to excite SP ($Re(\varepsilon) < -1$).

To emphasize on the features of the excited SP, a spatiotemporal representation of the real part of the dielectric constant (Fig.5.9) is illustrated. The white line defines the boundaries of the region in which the material is characterized by $Re(\varepsilon) < -1$ which allows the excitation of SP. According to the illustrated picture, the maximum damping depth is of the order of $18nm$ if the SP conditions are satisfied. This is similar to the simulated value for Si [108].

On the other hand, the lifetime of the SP (i.e. smaller than the time required for melting and larger than the time needed to couple with the incident beam) as well the carrier density value ($\sim 2.6 \times 10^{21} cm^{-3}$ at around 80% of the intensity (Fig.5.10)) indicate that a SP-related periodic modulation of a resultant energy deposition through the coupling with the incident beam is possible (for this part, simulations have been performed for $E_p = 200mJ/cm^2$, $\tau_p = 100fs$ to compare

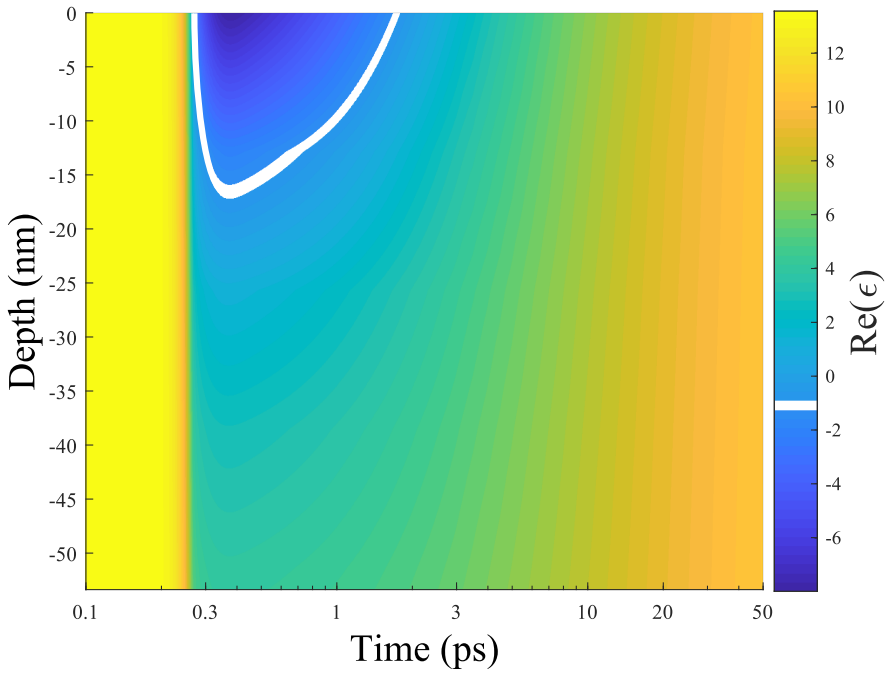

Figure 5.9: Spatio-temporal evolution of the real part of the dielectric constant. White line defines the limit where $Re(\varepsilon) < -1$. ($E_p = 70mJ/cm^2$, $\tau_p = 100fs$).

with experimental results). According to the computed value of the SP wavelength ($\sim 772nm$) based on the relevant N_e ($2.6 \times 10^{21} cm^{-3}$) and the use of Eq.5.10, there is a deviation from the experimental result (in the range of between $550nm$ and $680nm$ for NP $= 14$). This is an indication that the employment of Eq.5.10 towards calculating the SP-resonance wavelength is problematic as the expression was derived on the assumption that

the surface morphology is flat (i.e. requirement of continuity of electric and magnetic field on flat profiles). Therefore, as suggested in Section II, a different methodology is

required when NP is large enough to lead to the production of corrugated surfaces.

5.5.2 *Periodic structures and damage thresholds*

In previous reports, a correlation of the SP wavelength on the corrugation depth was proposed based on Finite Difference Time Domain (FDTD) simulations [90, 144]. While the evaluation of the optimum coupling of the laser beam with the excited SP requires appropri-

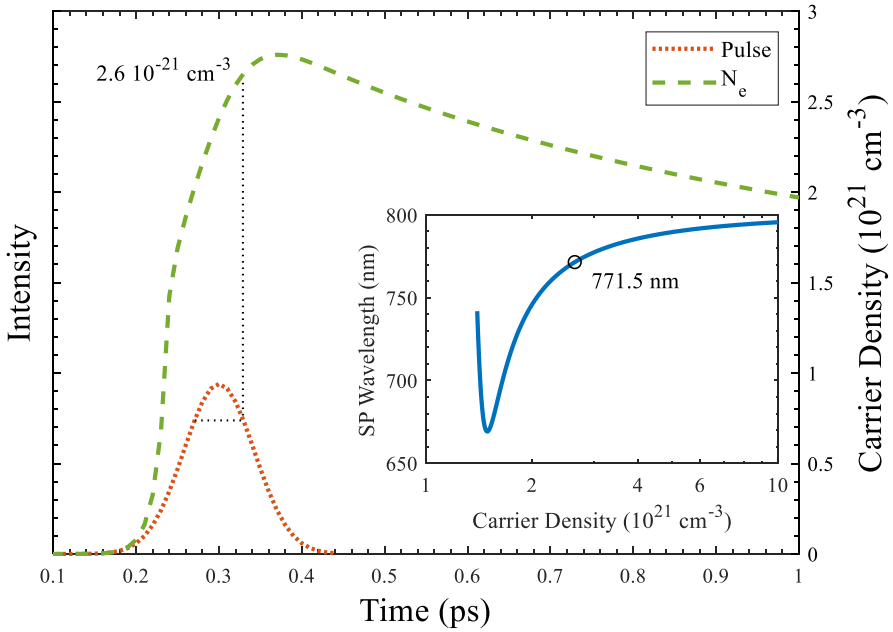

Figure 5.10: Carrier density evolution as a function of time. The temporal intensity profile defines the carrier density that gives a resonance (at 80%). ($E_p = 200mJ/cm^2$, $\tau_p = 100fs$).

ate calculations for GaAs, an estimate of the SP wavelength values can be deduced given the resemblance of the produced depths to those in our simulations. The dependence of the SP wavelength (Λ_{SP}) as a function of the corrugation height is

illustrated in Fig.5.11a (a blue shift to smaller wavelengths with increase of corrugation height as shown for Silicon (Si) [90]) while the approach to describe the multiscale physical mechanisms presented in Section II yield the correlation of the periodicity of the induced structures as a function of the number of pulses (Fig.5.11b). To correlate the number of pulses with the induced ripple's corrugation features (bottom-to-peak distance), Eqs.1-14 were solved together to calculate the effect of ablation and hydrodynamical transport impact; the latter is illustrated through the analysis of the fluid transport that is due to the temperature gradient and induced Marangoni mechanism of mass transfer [93, 136]). The surface profile produced from the simulations is illustrated for NP = 14 in a sector of the heat-affected region (Fig.5.12) where the rippled profile is characterized by an average periodicity Λ that is approximately equal to $637nm$. It is shown that the orientation of the induced periodic structures are perpendicular to the polarization

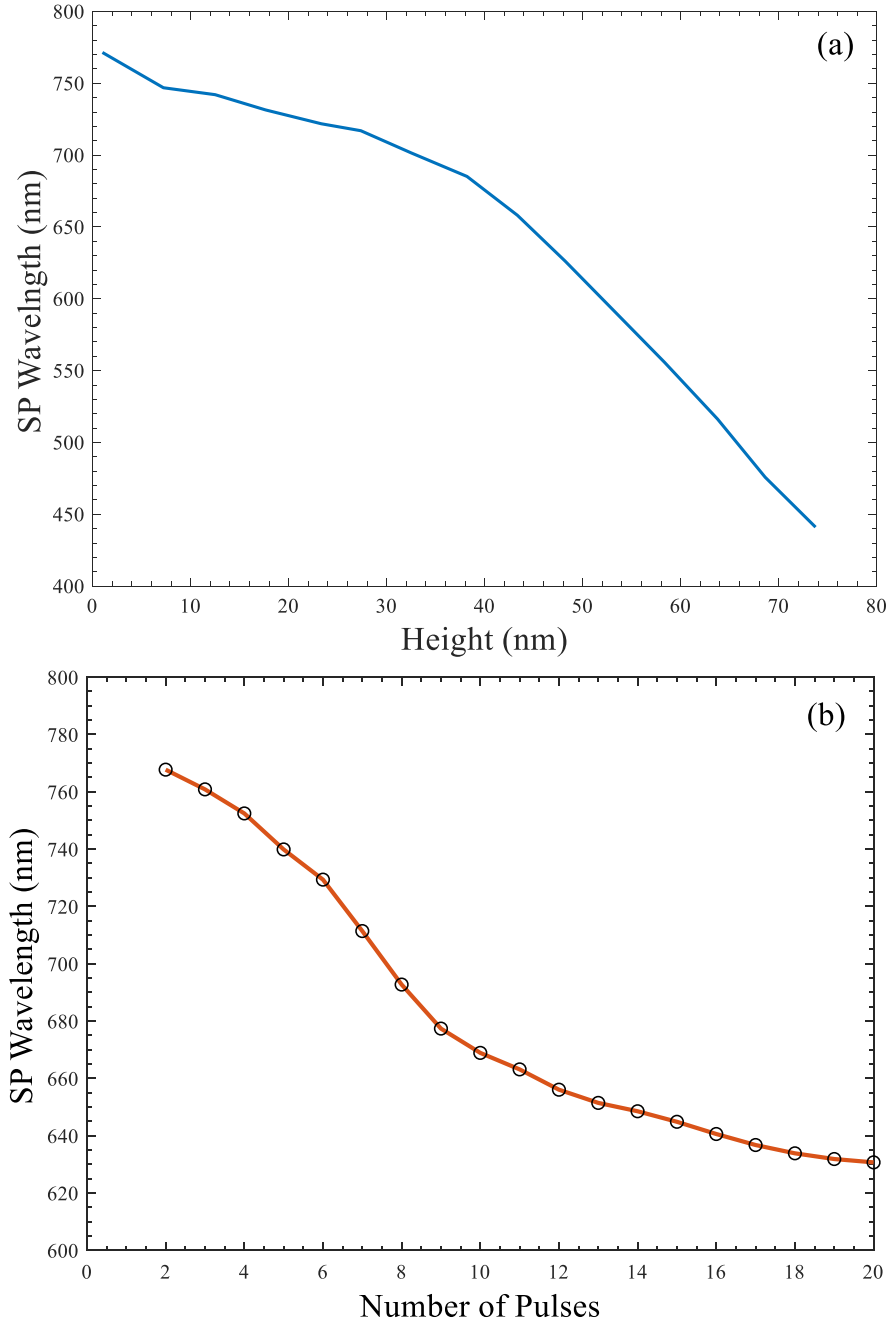

Figure 5.11: (a) SP wavelength vs. corrugation height, (b) SP periodicity vs. NP ($E_p = 200mJ/cm^2, \tau_p = 100fs$).

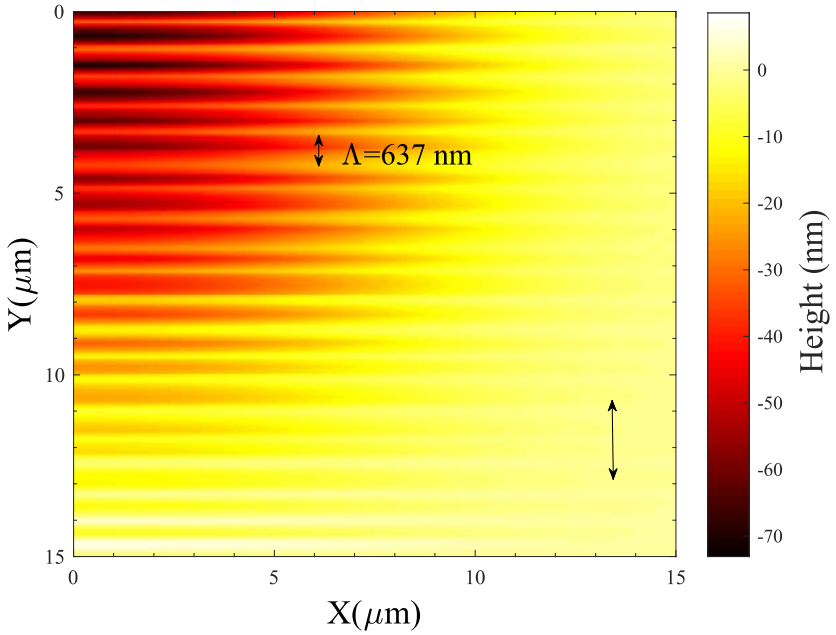

Figure 5.12: Surface pattern in a quadrant. Black doubled arrow at the bottom right indicates the polarization direction of the electric field of the incident beam. Λ stands for the calculated rippled periodicity. (NP = 14, $E_p = 200mJ/cm^2$, $\tau_p = 100fs$).

of the electric field of the incident beam (indicated by the *black doubled arrow* in Fig.5.12). The simulated result for NP = 14 for the ripple frequency ($\sim 637nm$ while the SP wavelength is $648nm$) appears to be close to the experimental result (Fig.5.2). The value difference between the SP wavelength and the predicted result is due to the correction assuming the role of fluid dynamics [93, 111]. Certainly, conditions that could improve the agreement with experimental observations include the consideration of a more precise mass removal mechanism of the material due to intense heating [93, 111], as a deeper profile is expected (Fig.5.11a) to lead to a larger shift of SP wavelength to smaller values. An expected damage threshold sharp decrease due to incubation effects (i.e. formation of self-trapped excitons) could also lead to an increase of the profile depth that is necessary to induce the deeper profile [170, 171]. However, as a detailed description of the role of incubation effects for GaAs is still elusive [170, 171], further analysis especially at high temperatures cannot be performed in a conclusive and accurate way. One approach to attain a more accurate description is to incorporate molecular dynamics into the continuum modelling methodology [172].

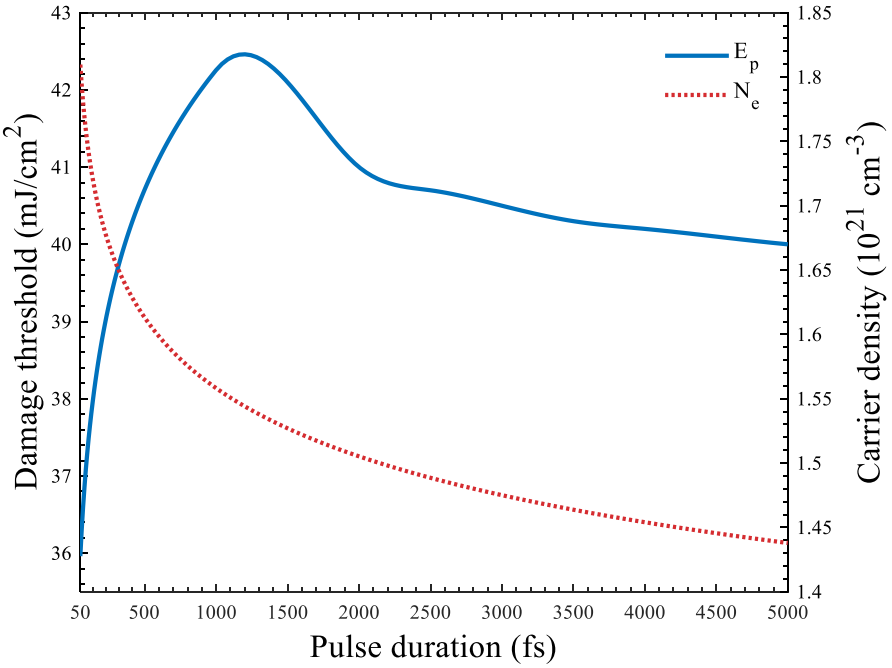

Figure 5.13: Damage thresholds and carrier density as a function of the pulse duration at $z = 0$.

The decrease of the SP wavelength with increasing dose (i.e. NP) that is reflected on the periodicity of the rippled profile (Fig.5.11b) follows the pattern also observed or predicted in other materials (see [84, 93–98, 100, 109, 173] and references therein). More specifically, a steep decrease is followed by saturation point. Although it is of paramount importance to explore whether (and at what values of NP), different periodic structures (i.e. grooves or spikes) are formed [84, 85, 174], such an investigation is beyond the scope of the present study.

While a detailed description of the physical mechanisms that lead to LIPSS formation is expected to allow production of the periodic structure formation in a systematic way, another significant area of investigation is the correlation of the damage thresholds (for $NP = 1$) with the laser parameters and more specifically the laser pulse duration. In regard to the determination of the value of the 'damage threshold', it is noted that there is an ambiguity regarding to whether morphological damage is associated to a mass displacement due to melting and re-solidification of the material or it is related to a mass removal (i.e. or ablation). In Fig.5.13, the computed

fluence ('damage threshold') corresponds to the minimum fluence value that induces melting of the material and it is plotted against

the pulse duration. As explained previously, a pulse width increase leads to a decrease of the absorbed energy (reflected also on the reduced number of excitation carriers shown in Fig.5.13) which indicates that more energy is required to damage the surface. Hence, in that case, the pulse should be characterized by a higher intensity that increases the damage threshold. Simulation results show that the damage threshold varies as $\sim \tau_p^{\gamma}$ at small pulse durations ($< 1ps$, where $\gamma = 0.053 \pm 0.011$). Similar dependencies have been estimated for other materials [123, 131, 161]. By contrast, at larger τ_p, there is a pronounced decrease of the damage threshold which is explained by an increased maximum lattice temperature [131]; the decline of the damage threshold at increasing pulse durations (larger than a few ps) has also been reported in previous studies [104, 131, 161]. The theoretical prediction is tested against experimental data in previous reports, nevertheless, those experimental results correspond to ablation studies or in other conditions [105, 126–128]. More specifically, in a previous report, $E_p^{dammage} = 100mJ/cm^2$ for $\tau_p = 70fs$ while experimental results in this work and an analysis of the SEM images (Fig.5.2) show that the laser conditions ($E_p^{dammage} = 200mJ/cm^2$ for $\tau_p 100fs$) produce some small mass removal. Due to the fact that mass removal requires large temperatures which in other materials is estimated to be about 2-3 times larger than the melting point (considering temperatures above the boiling or critical points [93, 98]) and given the, approximately, linear dependence of the temperature from the fluence, a rough estimate can be deduced to project the damage thresholds in Fig.5.13. Therefore, an estimated $35 - 37mJ/cm^2$ is deduced for a (experimental) value for the melting threshold for $\tau_p = 100fs$ which is in a good agreement with the theoretical predictions (Fig.5.13). Nevertheless, a more accurate conclusion will be drawn if more appropriately developed experimental protocols are introduced to evaluate the damage thresholds at the onset of the phase transition. To the best of our knowledge, there are not similar reports with experimental results for the pulse durations explored in this study.

Furthermore, apart from the estimation of the damage threshold and the frequencies of the periodic structures, the methodology can be used to derive further a complete description of the evolution of the morphological features of the induced structures (such as height, depth, volume of ablated region, etc.) as well as an elaborated account of the fluid dynamics (see [136]). Similar approaches have been ensued in previous reports [93, 97], however, a detailed presentation of such results is beyond the scope of the current work.

The theoretical model presented in this work aimed to describe systematically the parameters that influence the ultrafast dynamics of GaAs after heating with ultrashort pulses and estimate the thermal response of the material (associated eventually with surface modification); nevertheless, there are still many unexplored issues that need to be addressed (i.e. effective mass dependence on fluence, wavelength dependence, excitation in very short pulses, role of more complex beam polarization states, structural effects in extreme conditions, distinction between amorphous or crystalline material, mechanical effects, more accurate behaviour in ablation conditions, formation of voids inside the material after repetitive irradiation, role of incubation effects, consideration of degeneracy and departure from a Maxwell-Boltzmann-based assumption of carrier distribution, precise computation of carrier collision frequency and electron-phonon coupling, inclusion of the influence of impact ionisation and carrier diffusion, etc.) before a complete picture of the physical processes that characterize heating of GaAs with femtosecond laser pulses.

5.6 CONCLUSIONS

A detailed theoretical framework was presented that describes, for the first time, both the ultrafast dynamics and surface modification physical mechanism after heating of GaAs with ultrashort pulsed lasers. The influence of the laser conditions such as the pulse duration and the fluence were evaluated in an effort to explore conditions that lead to SP excitation. Results show an increase of the maximum value of the reflectivity at increasing fluence that emphasizes the metallic character of the heated material. To account for the frequencies of the experimentally observed periodic structures, a dose-dependent modulation of the SP wavelength which is excited on the corrugated surface is performed. Simulation results revealed a $\sim \tau_p^{0.053\pm0.011}$(at relatively small values of the pulse duration) dependence of the damage threshold and a SP-related periodic structure formation. The correlation of the laser characteristics dependencies of the ultrafast dynamics, material damage and onset of periodic structure formation can be used to streamline the modulation of the frequencies of the structures on the surface of a still not fully explored semiconductor under intense heating.

6

GENERAL CONCLUSIONS

In the thesis, the author's work performed at the Okinawa Institute of Science and Technology, Femtosecond Spectroscopy Unit during the first 2 years and at the University of Crete, Physics department for the last 3 years of the PhD enrollment is presented. It is mainly devoted to the study of the first THz photoconductive antenna based on femtosecond laser-ablated GaAs and a detailed theoretical framework on the ultrafast dynamics and surface modification physical mechanism after heating of GaAs with ultrashort pulsed lasers. The obtained results are interesting in both points of view of fundamental science and potential applications.

In the first part, we have presented THz-generation efficiency with up to 65% improvement, from a THz photoconductive antenna based on femtosecond laser-ablated GaAs, when compared to a SI-GaAs antenna. The optoelectronic properties of SI-GaAs, that were affected from femtosecond-laser-ablation, were studied in order to understand and explain the results of our measurements. We performed a parametric analysis to evaluate the optimal values of the optical excitation polarization angle, the orientation of the ablated ripples in respect to the electrodes, the number of pulses per illuminated spot and the fluence, involved in the laser ablation of the active region of the antenna. Other parameters that were not studied can also be optimized , such as laser ablation wavelength and pulse duration. Although we estimate that the performance of the antenna will not be affected by changes in the ripple size, since they are defined by the wavelength of the ablation laser, that can range from optical to NIR wavelengths, much smaller than the produced THz wavelengths. Bottom-line for this project, we demonstrate an example of a device with femtosecond-laser-ablation processing, which is an incredible tool to engineer material properties, such as carrier lifetime, hyper-doping and photoabsorption, hence granting access to fabricating more efficient THz devices and optoelectronic materials with lower cost.

In the second part, we have concentrated on modeling the ultrafast dynamics and surface modification physical mechanism after heating of GaAs with ultrashort pulsed lasers in a detailed theoretical framework. Since the ripple formation arise from SP, we explored the laser conditions, like pulse duration and the fluency, that lead

to excitation of SP. In the results we observe a metallic behavior of the semiconductor surface at higher fluences, due to the increased excited free carrier concentration, following with a rise in the maximum value of reflectivity. We perform a dose-dependent modulation of the SP-wavelength, which is excited on the corrugated surface, in order to explain the spatial frequency of the ripples observed in the experimental samples. Results of the SP-caused ripples and the dependence of the damage threshold present a $\sim \tau_p^{0.053\pm0.011}$ (at relatively small values of the pulse duration). The study on the dependence between material damage, initiation of ripple formation and ultrafast dynamics can be exploited to engineer the spatial frequencies of periodic structure formations on the surface of GaAs, that still remains not fully studied under conditions of excessive heating. Hence, a detailed description of the thermal response of the material is aimed to allow a systematic laser-based processing and produce surface structures with application-based properties.

Part III

APPENDIX

BIBLIOGRAPHY

[1] Nathan M. Burford and Magda O. El-Shenawee. "Review of terahertz photoconductive antenna technology." In: *Optical Engineering* 56.1 (2017), p. 010901. ISSN: 0091-3286. DOI: 10.1117/1.OE.56.1.010901. URL: http://opticalengineering.spiedigitallibrary.org/article.aspx?doi=10.1117/1.OE.56.1.010901 (cit. on p. 7).

[2] Dae Sin Kim and D. S. Citrin. "Coulomb and radiation screening in photoconductive terahertz sources." In: *Applied Physics Letters* 88.16 (2006), p. 161117. ISSN: 0003-6951. DOI: 10.1063/1.2196480. URL: http://aip.scitation.org/doi/10.1063/1.2196480 (cit. on p. 9).

[3] Stephen E. Ralph and D. Grischkowsky. "Trap-enhanced electric fields in semi-insulators: The role of electrical and optical carrier injection." In: *Applied Physics Letters* 59.16 (1991), pp. 1972–1974. ISSN: 0003-6951. DOI: 10.1063/1.106153. URL: http://aip.scitation.org/doi/10.1063/1.106153 (cit. on p. 9).

[4] Masatsugu Yamashita, Kodo Kawase, Chiko Otani, Toshihiko Kiwa, and Masayoshi Tonouchi. "Imaging of large-scale integrated circuits using laser-terahertz emission microscopy." In: *Optics express* 13.1 (2005), pp. 115–120. ISSN: 1094-4087. DOI: 10.1364/OPEX.13.000115. URL: https://www.osapublishing.org/oe/abstract.cfm?uri=oe-13-1-115 (cit. on p. 16).

[5] Ruth M. Woodward, Bryan E. Cole, Vincent P. Wallace, Richard J. Pye, Donald D. Arnone, Edmund H. Linfield, and Michael Pepper. "Terahertz pulse imaging in reflection geometry of human skin cancer and skin tissue." In: *Physics in Medicine and Biology* 47.21 (2002), pp. 3853–3863. ISSN: 00319155. DOI: 10.1088/0031-9155/47/21/325. URL: http://stacks.iop.org/0031-9155/47/i=21/a=325?key=crossref.ee5adcbc8d6ef833bb46aa6cbd0a050e (cit. on p. 16).

[6] M. Nagel, P. Haring Bolivar, M. Brucherseifer, H. Kurz, A. Bosserhoff, and R. Büttner. "Integrated THz technology for label-free genetic diagnostics." In: *Applied Physics Letters* 80.1 (2002), pp. 154–156. ISSN: 00036951. DOI: 10.1063/1.1428619.

URL: http://aip.scitation.org/doi/10.1063/1.1428619 (cit. on p. 16).

[7] J. Y. Chen, J. R. Knab, J. Cerne, and A. G. Markelz. "Large oxidation dependence observed in terahertz dielectric response for cytochrome c." In: *Physical Review E - Statistical, Nonlinear, and Soft Matter Physics* 72.4 (2005), p. 040901. ISSN: 15393755. DOI: 10.1103/PhysRevE.72.040901. URL: https://link.aps.org/doi/10.1103/PhysRevE.72.040901 (cit. on p. 16).

[8] S. E. Whitmire, D. Wolpert, A. G. Markelz, J. R. Hillebrecht, J. Galan, and R. R. Birge. "Protein flexibility and conformational state: A comparison of collective vibrational modes of wild-type and D96N bacteriorhodopsin." In: *Biophysical Journal* 85.2 (2003), pp. 1269–1277. ISSN: 00063495. DOI: 10.1016/S0006-3495(03)74562-7. URL: http://linkinghub.elsevier.com/retrieve/pii/S0006349503745627 (cit. on p. 16).

[9] M. Herrmann, H. Tabata, and T. Kawai. "Terahertz time-domain spectroscopy and imaging of DNA." In: *IQEC, International Quantum Electronics Conference Proceedings* 2005.14 (2005), pp. 1240–1241. ISSN: 01959271. DOI: 10.1109/IQEC.2005.1561064. URL: https://www.osapublishing.org/oe/abstract.cfm?uri=oe-13-14-5205 (cit. on p. 16).

[10] Markus Walther, Bernd M. Fischer, and P. Uhd Jepsen. "Noncovalent intermolecular forces in polycrystalline and amorphous saccharides in the far infrared." In: *Chemical Physics* 288.2-3 (2003), pp. 261–268. ISSN: 03010104. DOI: 10.1016/S0301-0104(03)00031-4. URL: http://linkinghub.elsevier.com/retrieve/pii/S0301010403000314 (cit. on p. 16).

[11] Naoto Nagai, Ryoichi Kumazawa, and Ryoichi Fukasawa. "Direct evidence of inter-molecular vibrations by THz spectroscopy." In: *Chemical Physics Letters* 413.4-6 (2005), pp. 495–500. ISSN: 00092614. DOI: 10.1016/j.cplett.2005.08.023. URL: http://linkinghub.elsevier.com/retrieve/pii/S0009261405011875 (cit. on p. 16).

[12] Philip F. Taday, I. V. Bradley, D. D. Arnone, and M. Pepper. "Using Terahertz pulse spectroscopy to study the crystalline structure of a drug: A case study of the polymorphs of ranitidine hydrochloride." In: *Journal of Pharmaceutical Sciences* 92.4 (2003), pp. 831–838. ISSN: 00223549. DOI: 10.1002/jps.10358. URL: http://linkinghub.elsevier.com/retrieve/pii/S0022354916312151 (cit. on p. 16).

[13] Masayoshi Tonouchi. "Cutting-edge terahertz technology." In: *Nature Photonics* 1.2 (Feb. 2007), pp. 97–105. ISSN: 1749-4885. DOI: 10.1038/nphoton.2007.3. URL: http://www.nature.com/articles/nphoton.2007.3 (cit. on pp. 17, 20, 47).

[14] Hideki Hirori, Kumiko Yamashita, Masaya Nagai, and Koichiro Tanaka. "Attenuated total reflection spectroscopy in time domain using terahertz coherent pulses." In: *Japanese Journal of Applied Physics, Part 2: Letters* 43.10 A (2004), pp. L1287–L1289. ISSN: 00214922. DOI: 10.1143/JJAP.43.L1287. URL: http://stacks.iop.org/1347-4065/43/L1287 (cit. on p. 18).

[15] Masaya Nagai, Hiroyuki Yada, Takashi Arikawa, and Koichiro Tanaka. "Terahertz time-domain attenuated total reflection spectroscopy in water and biological solution." In: *International Journal of Infrared and Millimeter Waves* 27.4 (2006), pp. 505–515. ISSN: 01959271. DOI: 10.1007/s10762-006-9098-3. URL: http://link.springer.com/10.1007/s10762-006-9098-3 (cit. on p. 18).

[16] M. Misra, K. Kotani, I. Kawayama, H. Murakami, and M. Tonouchi. "Observation of TO1 soft mode in SrTiO3 films by terahertz time domain spectroscopy." In: *Applied Physics Letters* 87.18 (2005), p. 182909. ISSN: 0003-6951. DOI: 10.1063/1.2128039. URL: http://aip.scitation.org/doi/10.1063/1.2128039 (cit. on p. 18).

[17] Naoto Nagai and Ryoichi Fukasawa. "Abnormal dispersion of polymer films in the THz frequency region." In: *Chemical Physics Letters* 388.4-6 (2004), pp. 479–482. ISSN: 00092614. DOI: 10.1016/j.cplett.2004.03.044. URL: http://linkinghub.elsevier.com/retrieve/pii/S0009261404003914 (cit. on p. 18).

[18] Naoto Nagai, Tomoko Imai, Ryoichi Fukasawa, Koya Kato, and Koji Yamauchi. "Analysis of the intermolecular interaction of nanocomposites by THz spectroscopy." In: *Applied Physics Letters* 85.18 (2004), pp. 4010–4012. ISSN: 00036951. DOI: 10.1063/1.1811795. URL: http://aip.scitation.org/doi/10.1063/1.1811795 (cit. on p. 18).

[19] Naoto Nagai, Masakiyo Sumitomo, Mitsuru Imaizumi, and Ryoichi Fukasawa. "Characterization of electron- or proton-irradiated Si space solar cells by THz spectroscopy." In: *Semiconductor Science and Technology* 21.2 (2006), pp. 201–209. ISSN: 02681242. DOI: 10.1088/0268-1242/21/2/019. URL: http:

//stacks.iop.org/0268-1242/21/i=2/a=019?key=crossref.f9ee331d480d407893a44dc6a6292b5f (cit. on p. 18).

[20] D. M. Mittleman, J. Cunningham, M. C. Nuss, and M. Geva. "Noncontact semiconductor wafer characterization with the terahertz Hall effect." In: *Applied Physics Letters* 71.1 (1997), pp. 16–18. ISSN: 0003-6951. DOI: 10.1063/1.119456. URL: http://aip.scitation.org/doi/10.1063/1.119456 (cit. on p. 18).

[21] S. Nashima, O. Morikawa, K. Takata, and M. Hangyo. "Temperature dependence of optical and electronic properties of moderately doped silicon at terahertz frequencies." In: *Journal of Applied Physics* 90.2 (2001), pp. 837–842. ISSN: 0021-8979. DOI: 10.1063/1.1376673. URL: http://aip.scitation.org/doi/10.1063/1.1376673 (cit. on p. 18).

[22] Hua Zhong, Jingzhou Xu, Xu Xie, Tao Yuan, R. Reightler, E. Madaras, and Xi-Cheng Zhang. "Nondestructive defect identification with terahertz time-of-flight tomography." In: *IEEE Sensors Journal* 5.2 (2005), pp. 203–208. ISSN: 1530-437X. DOI: 10.1109/JSEN.2004.841341. URL: http://ieeexplore.ieee.org/document/1411797/ (cit. on pp. 19, 21).

[23] A.W.M. Lee, B.S. Wil, Sushil Kumar, Qing Hu, and J.L. Reno. "Real-time imaging using a 4.3-THz quantum cascade laser and a 320 /spl times/ 240 microbolometer focal-plane array." In: *IEEE Photonics Technology Letters* 18.13 (2006), pp. 1415–1417. ISSN: 1041-1135. DOI: 10.1109/LPT.2006.877220. URL: http://ieeexplore.ieee.org/document/1643241/ (cit. on p. 19).

[24] A. Hirata, T. Kosugi, H. Takahashi, R. Yamaguchi, F. Nakajima, T. Furuta, H. Ito, H. Sugahara, Y. Sato, and T. Nagatsuma. "120-GHz-band millimeter-wave photonic wireless link for 10-Gb/s data transmission." In: *IEEE Transactions on Microwave Theory and Techniques* 54.5 (2006), pp. 1937–1944. ISSN: 0018-9480. DOI: 10.1109/TMTT.2006.872798. URL: http://ieeexplore.ieee.org/document/1629034/ (cit. on p. 22).

[25] T. Kosugi, M. Tokumitsu, T. Enoki, M. Muraguchi, A. Hirata, and T. Nagatsuma. "120-GHz Tx/Rx chipset for 10-Gbit/s wireless applications using 0.1 μm-gate InP HEMTs." In: *2004 IEEE International SOI Conference (IEEE Cat. No.04CH37573)*. IEEE, pp. 171–174. ISBN: 0-7803-8616-7. DOI: 10.1109/CSICS.2004.1392524. URL: http://ieeexplore.ieee.org/document/1392524/ (cit. on pp. 22, 23).

[26] Y. Doi, S. Hirooka, A. Sato, M. Kawada, H. Shibai, Y. Okamura, S. Makiuti, T. Nakagawa, N. Hiromoto, and M. Fujiwara. "Large-format and compact stressed Ge:Ga array for the ASTRO-F (IRIS) mission." In: *Advances in Space Research* 30.9 (2002), pp. 2099–2104. ISSN: 02731177. DOI: 10.1016/S0273-1177(02)00594-X. URL: http://linkinghub.elsevier.com/retrieve/pii/S027311770200594X (cit. on p. 23).

[27] Mikio Fujiwara, Norihisa Hiromoto, Hiroshi Shibai, Takanori Hirao, and Takao Nakagawa. "Development of far-infrared Ge:Ga photoconductor 2D array for 3-THz imaging." In: ed. by Bjorn F. Andresen, Gabor F. Fulop, and Marija Strojnik. 2000, p. 842. DOI: 10.1117/12.409839. URL: http://proceedings.spiedigitallibrary.org/proceeding.aspx?doi=10.1117/12.409839 (cit. on p. 23).

[28] "AKARI." In: (). URL: http://www.ir.isas.jaxa.jp/AKARI/ (cit. on p. 23).

[29] J. Orenstein, J. Corson, S. Oh, and J.N. Eckstein. "Superconducting fluctuations in Bi2Sr2Ca1-xDyxCu2O8+δ as seen by terahertz spectroscopy." In: *Annalen der Physik* 15.7-8 (2006), pp. 596–605. ISSN: 0003-3804. DOI: 10.1002/andp.200510202. URL: http://doi.wiley.com/10.1002/andp.200510202 (cit. on p. 24).

[30] J. van Tilborg, C. B. Schroeder, C. V. Filip, Cs. Tóth, C. G. R. Geddes, G. Fubiani, R. Huber, R. A. Kaindl, E. Esarey, and W. P. Leemans. "Temporal Characterization of Femtosecond Laser-Plasma-Accelerated Electron Bunches Using Terahertz Radiation." In: *Physical Review Letters* 96.1 (2006), p. 014801. ISSN: 0031-9007. DOI: 10.1103/PhysRevLett.96.014801. URL: https://link.aps.org/doi/10.1103/PhysRevLett.96.014801 (cit. on p. 24).

[31] E. Beaurepaire, G. M. Turner, S. M. Harrel, M. C. Beard, J.-Y. Bigot, and C. A. Schmuttenmaer. "Coherent terahertz emission from ferromagnetic films excited by femtosecond laser pulses." In: *Applied Physics Letters* 84.18 (2004), pp. 3465–3467. ISSN: 0003-6951. DOI: 10.1063/1.1737467. URL: http://aip.scitation.org/doi/10.1063/1.1737467 (cit. on p. 24).

[32] Kouhei Takahashi, Noriaki Kida, and Masayoshi Tonouchi. "Terahertz Radiation by an Ultrafast Spontaneous Polarization Modulation of Multiferroic <math display="inline"> <msub> <mi>BiFeO</mi> <mn>3</mn> </msub> </math> Thin Films."

In: *Physical Review Letters* 96.11 (2006), p. 117402. ISSN: 0031-9007. DOI: 10.1103/PhysRevLett.96.117402. URL: https://link.aps.org/doi/10.1103/PhysRevLett.96.117402 (cit. on p. 24).

[33] Noriaki Kida, Hironaru Murakami, and Masayoshi Tonouchi. "Terahertz Optics in Strongly Correlated Electron Systems." In: *Terahertz Optoelectronics*. Berlin/Heidelberg: Springer-Verlag, pp. 271–330. DOI: 10.1007/10828028_8. URL: http://link.springer.com/10.1007/10828028{_}8 (cit. on p. 24).

[34] R. Huber, C. Kübler, S. Tübel, A. Leitenstorfer, Q. T. Vu, H. Haug, F. Köhler, and M.-C. Amann. "Femtosecond Formation of Coupled Phonon-Plasmon Modes in InP: Ultrabroadband THz Experiment and Quantum Kinetic Theory." In: *Physical Review Letters* 94.2 (2005), p. 027401. ISSN: 0031-9007. DOI: 10.1103/PhysRevLett.94.027401. URL: https://link.aps.org/doi/10.1103/PhysRevLett.94.027401 (cit. on p. 24).

[35] Zhongping Jian and Daniel M. Mittleman. "Broadband group-velocity anomaly in transmission through a terahertz photonic crystal slab." In: *Physical Review B* 73.11 (2006), p. 115118. ISSN: 1098-0121. DOI: 10.1103/PhysRevB.73.115118. URL: https://link.aps.org/doi/10.1103/PhysRevB.73.115118 (cit. on p. 24).

[36] Zhongping Jian, Jeremy Pearce, and Daniel M. Mittleman. "Characterizing Individual Scattering Events by Measuring the Amplitude and Phase of the Electric Field Diffusing through a Random Medium." In: *Physical Review Letters* 91.3 (2003), p. 033903. ISSN: 0031-9007. DOI: 10.1103/PhysRevLett.91.033903. URL: https://link.aps.org/doi/10.1103/PhysRevLett.91.033903 (cit. on p. 24).

[37] W. J. Padilla, A. J. Taylor, C. Highstrete, Mark Lee, and R. D. Averitt. "Dynamical Electric and Magnetic Metamaterial Response at Terahertz Frequencies." In: *Physical Review Letters* 96.10 (2006), p. 107401. ISSN: 0031-9007. DOI: 10.1103/PhysRevLett.96.107401. URL: https://link.aps.org/doi/10.1103/PhysRevLett.96.107401 (cit. on p. 24).

[38] Yuguang Zhao and D. Grischkowsky. "Terahertz demonstrations of effectively two-dimensional photonic bandgap structures." In: *Optics Letters* 31.10 (2006), p. 1534. ISSN: 0146-9592. DOI: 10.1364/OL.31.001534. URL: https://www.osapublishing.org/abstract.cfm?URI=ol-31-10-1534 (cit. on p. 24).

[39] Amit Agrawal and Ajay Nahata. "Time-domain radiative properties of a single subwavelength aperture surrounded by an exit side surface corrugation." In: *Optics Express* 14.5 (2006), p. 1973. ISSN: 1094-4087. DOI: 10.1364/OE.14.001973. URL: https://www.osapublishing.org/oe/abstract.cfm?uri=oe-14-5-1973 (cit. on p. 24).

[40] Kenji Ikushima, Yasuhiro Yoshimura, Takuma Hasegawa, Susumu Komiyama, Takeji Ueda, and Kazuhiko Hirakawa. "Photon-counting microscopy of terahertz radiation." In: *Applied Physics Letters* 88.15 (2006), p. 152110. ISSN: 0003-6951. DOI: 10.1063/1.2194473. URL: http://aip.scitation.org/doi/10.1063/1.2194473 (cit. on p. 24).

[41] Charles Kittel. *Introduction to Solid State Physics*. 8th ed. Willey, 2004. ISBN: 0-471-41526-X (cit. on pp. 26, 29, 31).

[42] Juergen Reif. "Basic Physics of Femtosecond Laser Ablation." In: 2010, pp. 19–41. DOI: 10.1007/978-3-642-03307-0_2. URL: http://link.springer.com/10.1007/978-3-642-03307-0{_}2 (cit. on p. 28).

[43] Matthias C Hoffmann and József András Fülöp. "Intense ultrashort terahertz pulses: generation and applications." In: *Journal of Physics D: Applied Physics* 44.8 (2011), p. 083001. ISSN: 0022-3727. DOI: 10.1088/0022-3727/44/8/083001. URL: http://stacks.iop.org/0022-3727/44/i=8/a=083001?key=crossref.412a24191f4272e9e96ee981164259a4 (cit. on p. 33).

[44] A. J. Lochtefeld, M. R. Melloch, J. C. P. Chang, and E. S. Harmon. "The role of point defects and arsenic precipitates in carrier trapping and recombination in low-temperature grown GaAs." In: *Applied Physics Letters* 69.10 (1996), pp. 1465–1467. ISSN: 0003-6951. DOI: 10.1063/1.116909. URL: http://aip.scitation.org/doi/10.1063/1.116909 (cit. on p. 33).

[45] I. S. Gregory, C. Baker, W. R. Tribe, M. J. Evans, H. E. Beere, E. H. Linfield, A. G. Davies, and M. Missous. "High resistivity annealed low-temperature GaAs with 100 fs lifetimes." In: *Applied Physics Letters* 83.20 (2003), pp. 4199–4201. ISSN: 0003-6951. DOI: 10.1063/1.1628389. URL: http://aip.scitation.org/doi/10.1063/1.1628389 (cit. on p. 33).

[46] E. S. Harmon, M. R. Melloch, J. M. Woodall, D. D. Nolte, N. Otsuka, and C. L. Chang. "Carrier lifetime versus anneal in low temperature growth GaAs." In: *Applied Physics Letters* 63.16 (1993), pp. 2248–2250. ISSN: 0003-6951. DOI: 10.1063/1.110542.

URL: http://aip.scitation.org/doi/10.1063/1.110542 (cit. on p. 33).

[47] H.S. Loka, S.D. Benjamin, and P.W.E. Smith. "Optical characterization of low-temperature-grown GaAs for ultrafast all-optical switching devices." In: *IEEE Journal of Quantum Electronics* 34.8 (1998), pp. 1426–1437. ISSN: 00189197. DOI: 10.1109/3.704335. URL: http://ieeexplore.ieee.org/document/704335/ (cit. on p. 33).

[48] S. Winnerl, F. Peter, S. Nitsche, A. Dreyhaupt, B. Zimmermann, M. Wagner, H. Schneider, M. Helm, and K. Kohler. "Generation and Detection of THz Radiation With Scalable Antennas Based on GaAs Substrates With Different Carrier Lifetimes." In: *IEEE Journal of Selected Topics in Quantum Electronics* 14.2 (2008), pp. 449–457. ISSN: 1077-260X. DOI: 10.1109/JSTQE.2007.910104. URL: http://ieeexplore.ieee.org/document/4481137/ (cit. on p. 33).

[49] Y. C. Shen, P. C. Upadhya, E. H. Linfield, H. E. Beere, and A. G. Davies. "Ultrabroadband terahertz radiation from low-temperature-grown GaAs photoconductive emitters." In: *Applied Physics Letters* 83.15 (2003), pp. 3117–3119. ISSN: 0003-6951. DOI: 10.1063/1.1619223. URL: http://aip.scitation.org/doi/10.1063/1.1619223 (cit. on p. 34).

[50] Mihai Stafe, Aurelian Marcu, and Niculae N. Puscas. *Pulsed Laser Ablation of Solids*. Vol. 53. Springer Series in Surface Sciences. Berlin, Heidelberg: Springer Berlin Heidelberg, 2014. ISBN: 978-3-642-40977-6. DOI: 10.1007/978-3-642-40978-3. URL: http://link.springer.com/10.1007/978-3-642-40978-3 (cit. on p. 36).

[51] B. N. Chichkov, C. Momma, S. Nolte, F. Von Alvensleben, and A. Tünnermann. "Femtosecond, picosecond and nanosecond laser ablation of solids." In: *Applied Physics A: Materials Science and Processing* 63.2 (Aug. 1996), pp. 109–115. ISSN: 09478396. DOI: 10.1007/BF01567637. URL: http://link.springer.com/10.1007/BF01567637 (cit. on p. 47).

[52] Rafael R. Gattass and Eric Mazur. "Femtosecond laser micromachining in transparent materials." In: *Nature Photonics* 2.4 (Apr. 2008), pp. 219–225. ISSN: 1749-4885. DOI: 10.1038/nphoton.2008.47. URL: http://www.nature.com/articles/nphoton.2008.47 (cit. on p. 47).

[53] Claude Phipps, ed. *Laser Ablation and its Applications*. Vol. 129. Springer Series in Optical Sciences. Boston, MA: Springer US, 2007. ISBN: 978-0-387-30452-6. DOI: 10.1007/978-0-387-30453-3. URL: http://link.springer.com/10.1007/978-0-387-30453-3 (cit. on p. 47).

[54] S. K. Sundaram and E. Mazur. "Inducing and probing non-thermal transitions in semiconductors using femtosecond laser pulses." In: *Nature Materials* 1.4 (Dec. 2002), pp. 217–224. ISSN: 1476-1122. DOI: 10.1038/nmat767. URL: http://www.nature.com/articles/nmat767 (cit. on p. 47).

[55] A. Borowiec and H. K. Haugen. "Subwavelength ripple formation on the surfaces of compound semiconductors irradiated with femtosecond laser pulses." In: *Applied Physics Letters* 82.25 (June 2003), pp. 4462–4464. ISSN: 0003-6951. DOI: 10.1063/1.1586457. URL: http://aip.scitation.org/doi/10.1063/1.1586457 (cit. on p. 47).

[56] Meng-Ju Sher, Mark T. Winkler, and Eric Mazur. "Pulsed-laser hyperdoping and surface texturing for photovoltaics." In: *MRS Bulletin* 36.06 (June 2011), pp. 439–445. ISSN: 0883-7694. DOI: 10.1557/mrs.2011.111. URL: http://www.journals.cambridge.org/abstract{_}S0883769411001114 (cit. on p. 47).

[57] C. Wu, C. H. Crouch, L. Zhao, J. E. Carey, R. Younkin, J. A. Levinson, E. Mazur, R. M. Farrell, P. Gothoskar, and A. Karger. "Near-unity below-band-gap absorption by microstructured silicon." In: *Applied Physics Letters* 78.13 (Mar. 2001), pp. 1850–1852. ISSN: 0003-6951. DOI: 10.1063/1.1358846. URL: http://aip.scitation.org/doi/10.1063/1.1358846 (cit. on p. 47).

[58] Zhen-Yu Zhao, Zhi-Qiang Song, Wang-Zhou Shi, and Quan-Zhong Zhao. "Optical absorption and photocurrent enhancement in semi-insulating gallium arsenide by femtosecond laser pulse surface microstructuring." In: *Optics Express* 22.10 (May 2014), p. 11654. ISSN: 1094-4087. DOI: 10.1364/OE.22.011654. URL: https://www.osapublishing.org/oe/abstract.cfm?uri=oe-22-10-11654 (cit. on pp. 47, 48, 51, 59, 61).

[59] A. Y. Vorobyev and Chunlei Guo. "Antireflection effect of femtosecond laser-induced periodic surface structures on silicon." In: *Optics Express* 19.S5 (Sept. 2011), A1031. ISSN: 1094-4087. DOI: 10.1364/OE.19.0A1031. URL: https://www.osapublishing.org/oe/abstract.cfm?uri=oe-19-S5-A1031 (cit. on pp. 47, 61).

[60] Jörn Bonse, Arkadi Rosenfeld, and Jörg Krüger. "On the role of surface plasmon polaritons in the formation of laser-induced periodic surface structures upon irradiation of silicon by femtosecond-laser pulses." In: *Journal of Applied Physics* 106.10 (Nov. 2009), p. 104910. ISSN: 0021-8979. DOI: 10.1063/1.3261734. URL: http://aip.scitation.org/doi/10.1063/1.3261734 (cit. on pp. 47, 61).

[61] Thibault J.-Y. Derrien, Tatiana E. Itina, Rémi Torres, Thierry Sarnet, and Marc Sentis. "Possible surface plasmon polariton excitation under femtosecond laser irradiation of silicon." In: *Journal of Applied Physics* 114.8 (Aug. 2013), p. 083104. ISSN: 0021-8979. DOI: 10.1063/1.4818433. URL: http://aip.scitation.org/doi/10.1063/1.4818433 (cit. on p. 47).

[62] Charles A. Schmuttenmaer. "Exploring Dynamics in the Far-Infrared with Terahertz Spectroscopy." In: *Chemical Reviews* 104.4 (Apr. 2004), pp. 1759–1780. ISSN: 0009-2665. DOI: 10.1021/cr020685g. URL: http://pubs.acs.org/doi/abs/10.1021/cr020685g (cit. on p. 47).

[63] Bradley Ferguson and Xi-Cheng Zhang. "Materials for terahertz science and technology." In: *Nature Materials* 1.1 (Sept. 2002), pp. 26–33. ISSN: 1476-1122. DOI: 10.1038/nmat708. URL: http://www.nature.com/doifinder/10.1038/nmat708 (cit. on p. 47).

[64] Chen Zaichun, Mohsen Rahmani, Gong Yandong, Chong Tow Chong, and Hong Minghui. "Realization of Variable Three-Dimensional Terahertz Metamaterial Tubes for Passive Resonance Tunability." In: *Advanced Materials* 24.23 (June 2012), OP143–OP147. ISSN: 09359648. DOI: 10.1002/adma.201104575. URL: http://doi.wiley.com/10.1002/adma.201104575 (cit. on p. 47).

[65] Abhishek Singh, Sanjoy Pal, Harshad Surdi, S. S. Prabhu, Vandana Nanal, and R. G. Pillay. "Highly efficient and electrically robust carbon irradiated semi-insulating GaAs based photoconductive terahertz emitters." In: *Applied Physics Letters* 104.6 (Feb. 2014), p. 063501. ISSN: 0003-6951. DOI: 10.1063/1.4864623. URL: http://aip.scitation.org/doi/10.1063/1.4864623 (cit. on p. 47).

[66] J. Lloyd-Hughes, S. K. E. Merchant, L. Fu, H. H. Tan, C. Jagadish, E. Castro-Camus, and M. B. Johnston. "Influence of surface passivation on ultrafast carrier dynamics and terahertz radiation generation in GaAs." In: *Applied Physics Letters* 89.23

(Dec. 2006), p. 232102. ISSN: 0003-6951. DOI: 10.1063/1.2398915. URL: http://aip.scitation.org/doi/10.1063/1.2398915 (cit. on p. 47).

[67] Y. C. Shen, P. C. Upadhya, E. H. Linfield, H. E. Beere, and A. G. Davies. "Ultrabroadband terahertz radiation from low-temperature-grown GaAs photoconductive emitters." In: *Applied Physics Letters* 83.15 (Oct. 2003), pp. 3117–3119. ISSN: 0003-6951. DOI: 10.1063/1.1619223. URL: http://aip.scitation.org/doi/10.1063/1.1619223 (cit. on p. 47).

[68] R. A. Kaindl, M. A. Carnahan, D. Hägele, R. Lövenich, and D. S. Chemla. "Ultrafast terahertz probes of transient conducting and insulating phases in an electron–hole gas." In: *Nature* 423.6941 (June 2003), pp. 734–738. ISSN: 0028-0836. DOI: 10.1038/nature01676. URL: http://www.nature.com/articles/nature01676 (cit. on p. 48).

[69] Amit Pratap Singh, Avinashi Kapoor, and K.N. Tripathi. "Ripples and grain formation in GaAs surfaces exposed to ultrashort laser pulses." In: *Optics & Laser Technology* 34.7 (Oct. 2002), pp. 533–540. ISSN: 00303992. DOI: 10.1016/S0030-3992(02)00063-4. URL: http://linkinghub.elsevier.com/retrieve/pii/S0030399201001141http://linkinghub.elsevier.com/retrieve/pii/S0030399202000634 (cit. on p. 48).

[70] J.T. Darrow, X.-C. Zhang, D.H. Auston, and J.D. Morse. "Saturation properties of large-aperture photoconducting antennas." In: *IEEE Journal of Quantum Electronics* 28.6 (June 1992), pp. 1607–1616. ISSN: 00189197. DOI: 10.1109/3.135314. URL: http://ieeexplore.ieee.org/document/135314/ (cit. on p. 52).

[71] P. J. Hale, J. Madeo, C. Chin, S. S. Dhillon, J. Mangeney, J. Tignon, and K. M. Dani. "20 THz broadband generation using semi-insulating GaAs interdigitated photoconductive antennas." In: *Optics Express* 22.21 (Oct. 2014), p. 26358. ISSN: 1094-4087. DOI: 10.1364/OE.22.026358. URL: https://www.osapublishing.org/oe/abstract.cfm?uri=oe-22-21-26358 (cit. on p. 55).

[72] C. H. Crouch, J. E. Carey, J. M. Warrender, M. J. Aziz, E. Mazur, and F. Y. Génin. "Comparison of structure and properties of femtosecond and nanosecond laser-structured silicon." In: *Applied Physics Letters* 84.11 (Mar. 2004), pp. 1850–1852. ISSN: 0003-

6951. DOI: 10.1063/1.1667004. URL: http://aip.scitation.org/doi/10.1063/1.1667004 (cit. on p. 59).

[73] Meng-Ju Sher and Eric Mazur. "Intermediate band conduction in femtosecond-laser hyperdoped silicon." In: *Applied Physics Letters* 105.3 (July 2014), p. 032103. ISSN: 0003-6951. DOI: 10.1063/1.4890618. URL: http://aip.scitation.org/doi/10.1063/1.4890618 (cit. on p. 59).

[74] Anatoliy Y. Vorobyev and Chunlei Guo. "Direct femtosecond laser surface nano/microstructuring and its applications." In: *Laser & Photonics Reviews* 7.3 (2013), pp. 385–407. ISSN: 18638880. DOI: 10.1002/lpor.201200017. URL: http://doi.wiley.com/10.1002/lpor.201200017 (cit. on p. 69).

[75] V Zorba, L Persano, D Pisignano, A Athanassiou, E Stratakis, R Cingolani, P Tzanetakis, and C Fotakis. "Making silicon hydrophobic: wettability control by two-lengthscale simultaneous patterning with femtosecond laser irradiation." In: *Nanotechnology* 17.13 (2006), pp. 3234–3238. ISSN: 0957-4484. DOI: 10.1088/0957-4484/17/13/026. URL: http://stacks.iop.org/0957-4484/17/i=13/a=026?key=crossref.47105282c32e0d794c77191585a90392 (cit. on p. 69).

[76] Vassilia Zorba, Emmanuel Stratakis, Marios Barberoglou, Emmanuel Spanakis, Panagiotis Tzanetakis, Spiros H. Anastasiadis, and Costas Fotakis. "Biomimetic Artificial Surfaces Quantitatively Reproduce the Water Repellency of a Lotus Leaf." In: *Advanced Materials* 20.21 (2008), pp. 4049–4054. ISSN: 09359648. DOI: 10.1002/adma.200800651. URL: http://doi.wiley.com/10.1002/adma.200800651 (cit. on p. 69).

[77] D. (Dieter) Bauerle. *Laser processing and chemistry*. Springer, 2000, p. 788. ISBN: 3540668918 (cit. on p. 69).

[78] Jean-Claude. Diels and Wolfgang Rudolph. *Ultrashort laser pulse phenomena : fundamentals, techniques, and applications on a femtosecond time scale*. Elsevier/Academic Press, 2006, p. 652. ISBN: 9780080466408 (cit. on p. 69).

[79] Evie L. Papadopoulou, Athina Samara, Marios Barberoglou, Aleka Manousaki, Stamatis N. Pagakis, Ema Anastasiadou, Costas Fotakis, and Emmanuel Stratakis. "Silicon Scaffolds Promoting Three-Dimensional Neuronal Web of Cytoplasmic Processes." In: *Tissue Engineering Part C: Methods* 16.3 (2010), pp. 497–502. ISSN: 1937-3384. DOI: 10.1089/ten.tec.2009.0216.

URL: https://www.liebertpub.com/doi/10.1089/ten.tec.2009.0216 (cit. on p. 69).

[80] Z. B. Wang, M. H. Hong, Y. F. Lu, D. J. Wu, B. Lan, and T. C. Chong. "Femtosecond laser ablation of polytetrafluoroethylene (Teflon) in ambient air." In: *Journal of Applied Physics* 93.10 (2003), pp. 6375–6380. ISSN: 0021-8979. DOI: 10.1063/1.1568154. URL: http://aip.scitation.org/doi/10.1063/1.1568154 (cit. on p. 69).

[81] R. Böhme, S. Pissadakis, D. Ruthe, and K. Zimmer. "Laser backside etching of fused silica with ultra-short pulses." In: *Applied Physics A* 85.1 (2006), pp. 75–78. ISSN: 0947-8396. DOI: 10.1007/s00339-006-3652-7. URL: http://link.springer.com/10.1007/s00339-006-3652-7 (cit. on p. 69).

[82] Suzana M. Petrović, B. Gaković, D. Peruško, E. Stratakis, I. Bogdanović-Radović, M. Čekada, C. Fotakis, and B. Jelenković. "Femtosecond laser-induced periodic surface structure on the Ti-based nanolayered thin films." In: *Journal of Applied Physics* 114.23 (2013), p. 233108. ISSN: 0021-8979. DOI: 10.1063/1.4848016. URL: http://aip.scitation.org/doi/10.1063/1.4848016 (cit. on pp. 69, 70).

[83] B. N. Chichkov, C. Momma, S. Nolte, F. Alvensleben, and A. Tünnermann. "Femtosecond, picosecond and nanosecond laser ablation of solids." In: *Applied Physics A Materials Science & Processing* 63.2 (1996), pp. 109–115. ISSN: 0947-8396. DOI: 10.1007/BF01567637. URL: http://link.springer.com/10.1007/BF01567637 (cit. on p. 69).

[84] George D. Tsibidis, C. Fotakis, and E. Stratakis. "From ripples to spikes: A hydrodynamical mechanism to interpret femtosecond laser-induced self-assembled structures." In: *Physical Review B* 92.4 (2015), p. 041405. ISSN: 1098-0121. DOI: 10.1103/PhysRevB.92.041405. URL: https://link.aps.org/doi/10.1103/PhysRevB.92.041405 (cit. on pp. 69, 70, 99).

[85] Jijil JJ Nivas, Shutong He, Andrea Rubano, Antonio Vecchione, Domenico Paparo, Lorenzo Marrucci, Riccardo Bruzzese, and Salvatore Amoruso. "Direct Femtosecond Laser Surface Structuring with Optical Vortex Beams Generated by a q-plate." In: *Scientific Reports* 5.1 (2016), p. 17929. ISSN: 2045-2322. DOI: 10.1038/srep17929. URL: http://www.nature.com/articles/srep17929 (cit. on pp. 69, 99).

[86] Martynas Beresna, Mindaugas Gecevičius, Peter G. Kazansky, and Titas Gertus. "Radially polarized optical vortex converter created by femtosecond laser nanostructuring of glass." In: *Applied Physics Letters* 98.20 (2011), p. 201101. ISSN: 0003-6951. DOI: 10.1063/1.3590716. URL: http://aip.scitation.org/doi/10.1063/1.3590716 (cit. on p. 69).

[87] Evangelos Skoulas, Alexandra Manousaki, Costas Fotakis, and Emmanuel Stratakis. "Biomimetic surface structuring using cylindrical vector femtosecond laser beams." In: *Scientific reports* 7 (2017), p. 45114. ISSN: 2045-2322. DOI: 10.1038/srep45114. URL: http://www.ncbi.nlm.nih.gov/pubmed/28327611http://www.pubmedcentral.nih.gov/articlerender.fcgi?artid=PMC5361190 (cit. on p. 69).

[88] E. Stratakis, A. Ranella, and C. Fotakis. "Biomimetic micro/-nanostructured functional surfaces for microfluidic and tissue engineering applications." In: *Biomicrofluidics* 5.1 (2011), p. 013411. ISSN: 1932-1058. DOI: 10.1063/1.3553235. URL: http://aip.scitation.org/doi/10.1063/1.3553235 (cit. on pp. 69, 77).

[89] J. Bonse, M. Munz, and H. Sturm. "Structure formation on the surface of indium phosphide irradiated by femtosecond laser pulses." In: *Journal of Applied Physics* 97.1 (2005), p. 013538. ISSN: 0021-8979. DOI: 10.1063/1.1827919. URL: http://aip.scitation.org/doi/10.1063/1.1827919 (cit. on pp. 69, 70, 77).

[90] Min Huang, Fuli Zhao, Ya Cheng, Ningsheng Xu, and Zhizhan Xu. "Origin of Laser-Induced Near-Subwavelength Ripples: Interference between Surface Plasmons and Incident Laser." In: *ACS Nano* 3.12 (2009), pp. 4062–4070. ISSN: 1936-0851. DOI: 10.1021/nn900654v. URL: http://pubs.acs.org/doi/10.1021/nn900654v (cit. on pp. 69, 70, 77, 78, 95, 96).

[91] J. E. Sipe, Jeff F. Young, J. S. Preston, and H. M. van Driel. "Laser-induced periodic surface structure. I. Theory." In: *Physical Review B* 27.2 (1983), pp. 1141–1154. ISSN: 0163-1829. DOI: 10.1103/PhysRevB.27.1141. URL: https://link.aps.org/doi/10.1103/PhysRevB.27.1141 (cit. on pp. 69, 70, 77, 78).

[92] Zhou Guosheng, P. M. Fauchet, and A. E. Siegman. "Growth of spontaneous periodic surface structures on solids during laser illumination." In: *Physical Review B* 26.10 (1982), pp. 5366–5381. ISSN: 0163-1829. DOI: 10.1103/PhysRevB.26.5366. URL:

https://link.aps.org/doi/10.1103/PhysRevB.26.5366 (cit. on pp. 69, 77).

[93] G. D. Tsibidis, M. Barberoglou, P. A. Loukakos, E. Stratakis, and C. Fotakis. "Dynamics of ripple formation on silicon surfaces by ultrashort laser pulses in subablation conditions." In: *Physical Review B* 86.11 (2012), p. 115316. ISSN: 1098-0121. DOI: 10.1103/PhysRevB.86.115316. URL: https://link.aps.org/doi/10.1103/PhysRevB.86.115316 (cit. on pp. 69–72, 75–81, 83, 89, 90, 96, 98–100).

[94] George D. Tsibidis, Evangelos Skoulas, Antonis Papadopoulos, and Emmanuel Stratakis. "Convection roll-driven generation of supra-wavelength periodic surface structures on dielectrics upon irradiation with femtosecond pulsed lasers." In: *Physical Review B* 94.8 (2016), p. 081305. ISSN: 2469-9950. DOI: 10.1103/PhysRevB.94.081305. URL: https://link.aps.org/doi/10.1103/PhysRevB.94.081305 (cit. on pp. 69, 70, 77, 99).

[95] G. D. Tsibidis, E. Stratakis, and K. E. Aifantis. "Thermoplastic deformation of silicon surfaces induced by ultrashort pulsed lasers in submelting conditions." In: *Journal of Applied Physics* 111.5 (2012), p. 053502. ISSN: 0021-8979. DOI: 10.1063/1.3688020. URL: http://aip.scitation.org/doi/10.1063/1.3688020 (cit. on pp. 69, 77, 99).

[96] Antonis Papadopoulos, Evangelos Skoulas, George D. Tsibidis, and Emmanuel Stratakis. "Formation of periodic surface structures on dielectrics after irradiation with laser beams of spatially variant polarisation: a comparative study." In: *Applied Physics A* 124.2 (2018), p. 146. ISSN: 0947-8396. DOI: 10.1007/s00339-018-1573-x. URL: http://link.springer.com/10.1007/s00339-018-1573-x (cit. on pp. 69, 77, 99).

[97] George D. Tsibidis and Emmanuel Stratakis. "Ripple formation on silver after irradiation with radially polarised ultrashort-pulsed lasers." In: *Journal of Applied Physics* 121.16 (2017), p. 163106. ISSN: 0021-8979. DOI: 10.1063/1.4982071. URL: http://aip.scitation.org/doi/10.1063/1.4982071 (cit. on pp. 69, 77, 78, 99, 100).

[98] George D. Tsibidis, Alexandros Mimidis, Evangelos Skoulas, Sabrina V. Kirner, Jörg Krüger, Jörn Bonse, and Emmanuel Stratakis. "Modelling periodic structure formation on 100Cr6 steel after irradiation with femtosecond-pulsed laser beams." In: *Applied Physics A* 124.1 (2018), p. 27. ISSN: 0947-8396. DOI:

10.1007/s00339-017-1443-y. URL: http://link.springer.com/10.1007/s00339-017-1443-y (cit. on pp. 69, 77, 80, 99, 100).

[99] Milton Birnbaum. "Semiconductor Surface Damage Produced by Ruby Lasers." In: *Journal of Applied Physics* 36.11 (1965), pp. 3688–3689. ISSN: 0021-8979. DOI: 10.1063/1.1703071. URL: http://aip.scitation.org/doi/10.1063/1.1703071 (cit. on pp. 69, 77).

[100] Jorn Bonse, Sandra Hohm, Sabrina V. Kirner, Arkadi Rosenfeld, and Jorg Kruger. "Laser-Induced Periodic Surface Structures—A Scientific Evergreen." In: *IEEE Journal of Selected Topics in Quantum Electronics* 23.3 (2017). ISSN: 1077-260X. DOI: 10.1109/JSTQE.2016.2614183. URL: http://ieeexplore.ieee.org/document/7581030/ (cit. on pp. 69, 77, 99).

[101] Yanhua Han and Shiliang Qu. "The ripples and nanoparticles on silicon irradiated by femtosecond laser." In: *Chemical Physics Letters* 495.4-6 (2010), pp. 241–244. ISSN: 0009-2614. DOI: 10.1016/J.CPLETT.2010.06.071. URL: https://www.sciencedirect.com/science/article/abs/pii/S0009261410008808 (cit. on p. 69).

[102] Tsing-Hua Her, Richard J. Finlay, Claudia Wu, Shrenik Deliwala, and Eric Mazur. "Microstructuring of silicon with femtosecond laser pulses." In: *Applied Physics Letters* 73.12 (1998), pp. 1673–1675. ISSN: 0003-6951. DOI: 10.1063/1.122241. URL: http://aip.scitation.org/doi/10.1063/1.122241 (cit. on p. 69).

[103] A.J. Pedraza, J.D. Fowlkes, and Y.-F. Guan. "Surface nanostructuring of silicon." In: *Applied Physics A* 77.2 (), pp. 277–284. ISSN: 0947-8396. DOI: 10.1007/s00339-003-2113-9. URL: https://link.springer.com/article/10.1007/s00339-003-2113-9 (cit. on pp. 69, 89).

[104] Henry M. van Driel. "Kinetics of high-density plasmas generated in Si by 1.06- and 0.53- μm picosecond laser pulses." In: *Physical Review B* 35.15 (1987), pp. 8166–8176. ISSN: 0163-1829. DOI: 10.1103/PhysRevB.35.8166. URL: https://link.aps.org/doi/10.1103/PhysRevB.35.8166 (cit. on pp. 69, 71, 72, 74, 75, 84, 85, 89, 90, 100).

[105] S. K. Sundaram and E. Mazur. "Inducing and probing non-thermal transitions in semiconductors using femtosecond laser

pulses." In: *Nature Materials* 1.4 (2002), pp. 217–224. ISSN: 1476-1122. DOI: 10.1038/nmat767. URL: http://www.nature.com/articles/nmat767 (cit. on pp. 69, 70, 100).

[106] E. Knoesel, A. Hotzel, and M. Wolf. "Ultrafast dynamics of hot electrons and holes in copper: Excitation, energy relaxation, and transport effects." In: *Physical Review B* 57.20 (1998), pp. 12812–12824. ISSN: 0163-1829. DOI: 10.1103/PhysRevB.57.12812. URL: https://link.aps.org/doi/10.1103/PhysRevB.57.12812 (cit. on p. 69).

[107] Thibault J.-Y. Derrien, Jörg Krüger, Tatiana E. Itina, Sandra Höhm, Arkadi Rosenfeld, and Jörn Bonse. "Rippled area formed by surface plasmon polaritons upon femtosecond laser double-pulse irradiation of silicon: the role of carrier generation and relaxation processes." In: *Applied Physics A* 117.1 (2014), pp. 77–81. ISSN: 0947-8396. DOI: 10.1007/s00339-013-8205-2. URL: http://link.springer.com/10.1007/s00339-013-8205-2 (cit. on pp. 69, 70, 76).

[108] Thibault J.-Y. Derrien, Tatiana E. Itina, Rémi Torres, Thierry Sarnet, and Marc Sentis. "Possible surface plasmon polariton excitation under femtosecond laser irradiation of silicon." In: *Journal of Applied Physics* 114.8 (2013), p. 083104. ISSN: 0021-8979. DOI: 10.1063/1.4818433. URL: http://aip.scitation.org/doi/10.1063/1.4818433 (cit. on pp. 69, 75, 76, 89, 94).

[109] Jörn Bonse, Arkadi Rosenfeld, and Jörg Krüger. "On the role of surface plasmon polaritons in the formation of laser-induced periodic surface structures upon irradiation of silicon by femtosecond-laser pulses." In: *Journal of Applied Physics* 106.10 (2009), p. 104910. ISSN: 0021-8979. DOI: 10.1063/1.3261734. URL: http://aip.scitation.org/doi/10.1063/1.3261734 (cit. on pp. 70, 78, 99).

[110] Thibault J.-Y. Derrien, Tatiana E. Itina, Rémi Torres, Thierry Sarnet, and Marc Sentis. "Possible surface plasmon polariton excitation under femtosecond laser irradiation of silicon." In: *Journal of Applied Physics* 114.8 (2013), p. 083104. ISSN: 0021-8979. DOI: 10.1063/1.4818433. URL: http://aip.scitation.org/doi/10.1063/1.4818433 (cit. on pp. 70–72).

[111] M. Barberoglou, G. D. Tsibidis, D. Gray, E. Magoulakis, C. Fotakis, E. Stratakis, and P. A. Loukakos. "The influence of ultra-fast temporal energy regulation on the morphology of Si surfaces through femtosecond double pulse laser irradia-

tion." In: *Applied Physics A* 113.2 (2013), pp. 273–283. ISSN: 0947-8396. DOI: 10.1007/s00339-013-7893-y. URL: http://link.springer.com/10.1007/s00339-013-7893-y (cit. on pp. 70, 98).

[112] G. D. Tsibidis, E. Stratakis, P. A. Loukakos, and C. Fotakis. "Controlled ultrashort-pulse laser-induced ripple formation on semiconductors." In: *Applied Physics A* 114.1 (2014), pp. 57–68. ISSN: 0947-8396. DOI: 10.1007/s00339-013-8113-5. URL: http://link.springer.com/10.1007/s00339-013-8113-5 (cit. on p. 70).

[113] Olga Varlamova, Florenta Costache, Jürgen Reif, and Michael Bestehorn. "Self-organized pattern formation upon femtosecond laser ablation by circularly polarized light." In: *Applied Surface Science* 252.13 (2006), pp. 4702–4706. ISSN: 01694332. DOI: 10.1016/j.apsusc.2005.08.120. URL: http://linkinghub.elsevier.com/retrieve/pii/S0169433205013991 (cit. on p. 70).

[114] J. Z. P. Skolski, G. R. B. E. Römer, J. V. Obona, V. Ocelik, A. J. Huis in 't Veld, J. Th. M. De Hosson, G.R.B.E. Römer, and A.J. Huis in 't Veld. "Laser-induced periodic surface structures: Fingerprints of light localization." In: *Physical Review B* 85.7 (2012), p. 075320. ISSN: 1098-0121. DOI: 10.1103/PhysRevB.85.075320. URL: https://link.aps.org/doi/10.1103/PhysRevB.85.075320 (cit. on p. 70).

[115] Jörn Bonse and Jörg Krüger. "Pulse number dependence of laser-induced periodic surface structures for femtosecond laser irradiation of silicon." In: *Journal of Applied Physics* 108.3 (2010), p. 034903. ISSN: 0021-8979. DOI: 10.1063/1.3456501. URL: http://aip.scitation.org/doi/10.1063/1.3456501 (cit. on p. 70).

[116] F. Garrelie, J.-P. Colombier, F. Pigeon, S. Tonchev, N. Faure, M. Bounhalli, S. Reynaud, and O. Parriaux. "Evidence of surface plasmon resonance in ultrafast laser-induced ripples." In: *Optics Express* 19.10 (2011), p. 9035. ISSN: 1094-4087. DOI: 10.1364/OE.19.009035. URL: https://www.osapublishing.org/oe/abstract.cfm?uri=oe-19-10-9035 (cit. on p. 70).

[117] Jincheng Wang and Chunlei Guo. "Ultrafast dynamics of femtosecond laser-induced periodic surface pattern formation on metals." In: *Applied Physics Letters* 87.25 (2005), p. 251914. ISSN: 0003-6951. DOI: 10.1063/1.2146067. URL: http://aip.scitation.org/doi/10.1063/1.2146067 (cit. on p. 70).

[118] J. Bonse, J. Krüger, S. Höhm, and A. Rosenfeld. "Femtosecond laser-induced periodic surface structures." In: *Journal of Laser Applications* 24.4 (2012), p. 042006. ISSN: 1042-346X. DOI: 10.2351/1.4712658. URL: http://lia.scitation.org/doi/10.2351/1.4712658 (cit. on p. 70).

[119] Yasuhiko Shimotsuma, Peter G. Kazansky, Jiarong Qiu, and Kazuoki Hirao. "Self-Organized Nanogratings in Glass Irradiated by Ultrashort Light Pulses." In: *Physical Review Letters* 91.24 (2003), p. 247405. ISSN: 0031-9007. DOI: 10.1103/PhysRevLett.91.247405. URL: https://link.aps.org/doi/10.1103/PhysRevLett.91.247405 (cit. on p. 70).

[120] B. Chimier, O. Utéza, N. Sanner, M. Sentis, T. Itina, P. Lassonde, F. Légaré, F. Vidal, and J. C. Kieffer. "Damage and ablation thresholds of fused-silica in femtosecond regime." In: *Physical Review B* 84.9 (2011), p. 094104. ISSN: 1098-0121. DOI: 10.1103/PhysRevB.84.094104. URL: https://link.aps.org/doi/10.1103/PhysRevB.84.094104 (cit. on p. 70).

[121] George D. Tsibidis. "Ultrafast dynamics of non-equilibrium electrons and strain generation under femtosecond laser irradiation of Nickel." In: *Applied Physics A* 124.4 (2018), p. 311. ISSN: 0947-8396. DOI: 10.1007/s00339-018-1704-4. URL: http://link.springer.com/10.1007/s00339-018-1704-4 (cit. on p. 70).

[122] George D. Tsibidis. "The influence of dynamical change of optical properties on the thermomechanical response and damage threshold of noble metals under femtosecond laser irradiation." In: *Journal of Applied Physics* 123.8 (2018), p. 085903. ISSN: 0021-8979. DOI: 10.1063/1.5011738. URL: http://aip.scitation.org/doi/10.1063/1.5011738 (cit. on p. 70).

[123] Chandra S. R. Nathala, Ali Ajami, Wolfgang Husinsky, Bilal Farooq, Sergey I. Kudryashov, Albena Daskalova, Irina Bliznakova, and Andreas Assion. "Ultrashort laser pulse ablation of copper, silicon and gelatin: effect of the pulse duration on the ablation thresholds and the incubation coefficients." In: *Applied Physics A* 122.2 (2016), p. 107. ISSN: 0947-8396. DOI: 10.1007/s00339-016-9625-6. URL: http://link.springer.com/10.1007/s00339-016-9625-6 (cit. on pp. 70, 100).

[124] A. A. Ionin, S. I. Kudryashov, S. V. Makarov, L. V. Seleznev, and D. V. Sinitsyn. "Electron dynamics and prompt ablation of aluminum surface excited by intense femtosecond laser

pulse." In: *Applied Physics A* 117.4 (2014), pp. 1757–1763. ISSN: 0947-8396. DOI: 10.1007/s00339-014-8826-0. URL: http://link.springer.com/10.1007/s00339-014-8826-0 (cit. on p. 70).

[125] A. Borowiec and H. K. Haugen. "Subwavelength ripple formation on the surfaces of compound semiconductors irradiated with femtosecond laser pulses." In: *Applied Physics Letters* 82.25 (2003), pp. 4462–4464. ISSN: 0003-6951. DOI: 10.1063/1.1586457. URL: http://aip.scitation.org/doi/10.1063/1.1586457 (cit. on p. 70).

[126] J. Paul Callan, Albert M.-T. Kim, Christopher A.D. Roeser, and Eric Mazur. "Ultrafast dynamics and phase changes in highly excited GaAs." In: *Semiconductors and*. Vol. 67. 2001, pp. 151–203. ISBN: 0127521763. DOI: 10.1016/S0080-8784(01)80170-8. arXiv: 0-12-752176-3. URL: http://www.sciencedirect.com/science/article/pii/S0080878401801708http://linkinghub.elsevier.com/retrieve/pii/S0080878401801708 (cit. on pp. 71, 100).

[127] A. M.-T. Kim, J. P. Callan, C. A. D. Roeser, and E. Mazur. "Ultrafast dynamics and phase changes in crystalline and amorphous GaAs." In: *Physical Review B* 66.24 (2002), p. 245203. ISSN: 0163-1829. DOI: 10.1103/PhysRevB.66.245203. URL: https://link.aps.org/doi/10.1103/PhysRevB.66.245203 (cit. on pp. 71, 100).

[128] K. Sokolowski-Tinten, H. Schulz, J. Bialkowski, and D. Linde. "Two distinct transitions in ultrafast solid-liquid phase transformations of GaAs." In: *Applied Physics A Solids and Surfaces* 53.3 (1991), pp. 227–234. ISSN: 0721-7250. DOI: 10.1007/BF00324257. URL: http://link.springer.com/10.1007/BF00324257 (cit. on pp. 71, 100).

[129] Sunghyun Moon, Kangho Kim, Youngjo Kim, Junseok Heo, and Jaejin Lee. "Highly efficient single-junction GaAs thin-film solar cell on flexible substrate." In: *Scientific Reports* 6.1 (2016), p. 30107. ISSN: 2045-2322. DOI: 10.1038/srep30107. URL: http://www.nature.com/articles/srep30107 (cit. on p. 71).

[130] Julien Madéo, Athanasios Margiolakis, Zhen-Yu Zhao, Peter J Hale, Michael K L Man, Quan-Zhong Zhao, Wei Peng, Wang-Zhou Shi, and Keshav M Dani. "Ultrafast properties of femtosecond-laser-ablated GaAs and its application to terahertz optoelectronics." In: *Optics letters* 40.14 (2015), pp. 3388–91. ISSN: 1539-4794.

DOI: 10.1364/OL.40.003388. URL: http://www.ncbi.nlm.nih.gov/pubmed/26176476 (cit. on p. 71).

[131] J.K. Chen, D.Y. Tzou, and J.E. Beraun. "Numerical investigation of ultrashort laser damage in semiconductors." In: *International Journal of Heat and Mass Transfer* 48.3-4 (2005), pp. 501–509. ISSN: 00179310. DOI: 10.1016/j.ijheatmasstransfer.2004.09.015. URL: http://linkinghub.elsevier.com/retrieve/pii/S001793100400417X (cit. on pp. 71–75, 89, 90, 100).

[132] A. Rämer, O. Osmani, and B. Rethfeld. "Laser damage in silicon: Energy absorption, relaxation, and transport." In: *Journal of Applied Physics* 116.5 (2014), p. 053508. ISSN: 0021-8979. DOI: 10.1063/1.4891633. URL: http://aip.scitation.org/doi/10.1063/1.4891633 (cit. on pp. 71–76, 89, 90).

[133] S I Anisimov, B L Kapeliovich, T L Perel'man, and L D Landau. *Electron emission from metal surfaces exposed to ultrashort laser pulses*. Tech. rep. 1975. URL: http://www.jetp.ac.ru/cgi-bin/dn/e{_}039{_}02{_}0375.pdf (cit. on pp. 71, 72).

[134] D. Agassi. "Phenomenological model for pisosecond-pulse laser annealing of semiconductors." In: *Journal of Applied Physics* 55.12 (1984), pp. 4376–4383. ISSN: 0021-8979. DOI: 10.1063/1.333007. URL: http://aip.scitation.org/doi/10.1063/1.333007 (cit. on pp. 73, 84).

[135] Ioffe. "Electrical properties of GaAs." In: (). URL: http://www.ioffe.ru/SVA/NSM/Semicond/GaAs/electric.html (cit. on pp. 73, 74).

[136] Ioffe. "See Supplementary Material at [URL] for a detailed description of (a) electron temperature and carrier density evolution for different fluences, (b) approximate estimation of surface tension for diffferent lattice temperature values, (c) heat conductivity." In: () (cit. on pp. 74, 81, 85, 86, 89, 96, 100).

[137] K. Sokolowski-Tinten and D. von der Linde. "Generation of dense electron-hole plasmas in silicon." In: *Physical Review B* 61.4 (2000), pp. 2643–2650. ISSN: 0163-1829. DOI: 10.1103/PhysRevB.61.2643. URL: https://link.aps.org/doi/10.1103/PhysRevB.61.2643 (cit. on pp. 75, 92).

[138] J.-W. Pan, J.-L. Shieh, J.-H. Gau, J.-I. Chyi, J.-C. Lee, and K.-J. Ling. "Study of the optical properties of In _{0.52} (Al _x Ga _{1- x}) _{0.48} As by variable angle spectroscopic ellipsometry." In: *Journal of Applied Physics* 78.1 (1995), pp. 442–445.

ISSN: 0021-8979. DOI: 10.1063/1.360624. URL: http://aip.scitation.org/doi/10.1063/1.360624 (cit. on p. 75).

[139] Włodzimierz Nakwaski. "Effective masses of electrons and heavy holes in GaAs, InAs, A1As and their ternary compounds." In: *Physica B: Condensed Matter* 210.1 (1995), pp. 1–25. ISSN: 0921-4526. DOI: 10.1016/0921-4526(94)00921-H. URL: https://www.sciencedirect.com/science/article/pii/092145269400921H (cit. on pp. 75, 76).

[140] H. (Heinz) Raether. *Surface plasmons on smooth and rough surfaces and on gratings*. Springer-Verlag, 1988, p. 136. ISBN: 9783540173632 (cit. on pp. 76, 77).

[141] J M Pitarke, V M Silkin, E V Chulkov, and P M Echenique. "Theory of surface plasmons and surface-plasmon polaritons." In: *Reports on Progress in Physics* 70.1 (2007), pp. 1–87. ISSN: 0034-4885. DOI: 10.1088/0034-4885/70/1/R01. URL: http://stacks.iop.org/0034-4885/70/i=1/a=R01?key=crossref.5b1052b473009d0de2f21c63e367f570 (cit. on p. 76).

[142] Alexey M. Bonch-Bruevich. "Surface electromagnetic waves in optics." In: *Optical Engineering* 31.4 (1992), p. 718. ISSN: 00913286. DOI: 10.1117/12.56133. URL: http://opticalengineering.spiedigitallibrary.org/article.aspx?doi=10.1117/12.56133 (cit. on p. 77).

[143] Jincheng Wang and Chunlei Guo. "Numerical study of ultrafast dynamics of femtosecond laser-induced periodic surface structure formation on noble metals." In: *Journal of Applied Physics* 102.5 (2007), p. 053522. ISSN: 0021-8979. DOI: 10.1063/1.2776004. URL: http://aip.scitation.org/doi/10.1063/1.2776004 (cit. on p. 77).

[144] J.P. Colombier. "Plasmonic and Hydrodynamic Effects in Ultrafast Laser-Induced Periodic Surface Structures on Metals." In: *Journal of Laser Micro/Nanoengineering* 7.3 (2012), pp. 362–368. ISSN: 18800688. DOI: 10.2961/jlmn.2012.03.0023. URL: http://www.jlps.gr.jp/jlmn/index.php?action=laser{_}volno{\&}volno=703 (cit. on pp. 78, 95).

[145] Heinz Raether. *Surface Plasmons on Smooth and Rough Surfaces and on Gratings*. Vol. 111. Springer Tracts in Modern Physics. Berlin, Heidelberg: Springer Berlin Heidelberg, 1988. ISBN: 978-3-540-17363-2. DOI: 10.1007/BFb0048317. URL: http://link.springer.com/10.1007/BFb0048317 (cit. on p. 78).

[146] Haiyan Zhao, Wenchong Niu, Bin Zhang, Yongping Lei, Masaru Kodama, and Takashi Ishide. "Modelling of keyhole dynamics and porosity formation considering the adaptive keyhole shape and three-phase coupling during deep-penetration laser welding." In: *Journal of Physics D: Applied Physics* 44.48 (2011), p. 485302. ISSN: 0022-3727. DOI: 10.1088/0022-3727/44/48/485302. URL: http://stacks.iop.org/0022-3727/44/i=48/a=485302?key=crossref.e91dac1807a69cad52e6c17498635244 (cit. on p. 80).

[147] Jung-Ho Cho, Dave F Farson, John O Milewski, and Kendall J Hollis. "Weld pool flows during initial stages of keyhole formation in laser welding." In: *Journal of Physics D: Applied Physics* 42.17 (2009), p. 175502. ISSN: 0022-3727. DOI: 10.1088/0022-3727/42/17/175502. URL: http://stacks.iop.org/0022-3727/42/i=17/a=175502?key=crossref.35e98d7bb6cfa3cebb026f498e8757ae (cit. on p. 80).

[148] D.P. Korfiatis, K.-A. Th. Thoma, and J.C. Vardaxoglou. "Numerical modeling of ultrashort-pulse laser ablation of silicon." In: *Applied Surface Science* 255.17 (2009), pp. 7605–7609. ISSN: 01694332. DOI: 10.1016/j.apsusc.2009.04.036. URL: http://linkinghub.elsevier.com/retrieve/pii/S0169433209004115 (cit. on p. 80).

[149] L D Landau and E. M. Lifshitz. *Fluid Mechanics (2nd Edition)*. 1987, p. 554. ISBN: 9781483161044 (cit. on p. 80).

[150] Jun Zhou, Hai-Lung Tsai, and Pei-Chung Wang. "Transport Phenomena and Keyhole Dynamics during Pulsed Laser Welding." In: *Journal of Heat Transfer* 128.7 (2006), p. 680. ISSN: 00221481. DOI: 10.1115/1.2194043. URL: http://heattransfer.asmedigitalcollection.asme.org/article.aspx?articleid=1448395 (cit. on p. 80).

[151] Roger Kelly and Antonio Miotello. "Comments on explosive mechanisms of laser sputtering." In: *Applied Surface Science* 96-98 (1996), pp. 205–215. ISSN: 01694332. DOI: 10.1016/0169-4332(95)00481-5. URL: http://linkinghub.elsevier.com/retrieve/pii/0169433295004815 (cit. on p. 81).

[152] Nadezhda M Bulgakova and Igor M Bourakov. "Phase explosion under ultrashort pulsed laser ablation: modeling with analysis of metastable state of melt." In: *Applied Surface Science* 197-198 (2002), pp. 41–44. ISSN: 01694332. DOI: 10.1016/S0169-

4332(02)00300-8. URL: http://linkinghub.elsevier.com/retrieve/pii/S0169433202003008 (cit. on p. 81).

[153] J K Chen and J E Beraun. "Modelling of ultrashort laser ablation of gold films in vacuum." In: *Journal of Optics A: Pure and Applied Optics* 5.3 (2003), pp. 168–173. ISSN: 1464-4258. DOI: 10.1088/1464-4258/5/3/304. URL: http://stacks.iop.org/1464-4258/5/i=3/a=304?key=crossref.e9377d2dacadaa615ab90d63b03a8420 (cit. on pp. 81, 83).

[154] Pablo Solana and Guillermo Negro. "A study of the effect of multiple reflections on the shape of the keyhole in the laser processing of materials." In: *Journal of Physics D: Applied Physics* 30.23 (1997), pp. 3216–3222. ISSN: 0022-3727. DOI: 10.1088/0022-3727/30/23/006. URL: http://stacks.iop.org/0022-3727/30/i=23/a=006?key=crossref.a99829446315c2fec48fc48c5dbbdb57 (cit. on p. 82).

[155] Youhei Morinishi, Oleg V. Vasilyev, and Takeshi Ogi. "Fully conservative finite difference scheme in cylindrical coordinates for incompressible flow simulations." In: *Journal of Computational Physics* 197.2 (2004), pp. 686–710. ISSN: 00219991. DOI: 10.1016/j.jcp.2003.12.015. URL: http://linkinghub.elsevier.com/retrieve/pii/S0021999103006594 (cit. on p. 82).

[156] Y. Morinishi, T.S. Lund, O.V. Vasilyev, and P. Moin. "Fully Conservative Higher Order Finite Difference Schemes for Incompressible Flow." In: *Journal of Computational Physics* 143.1 (1998), pp. 90–124. ISSN: 00219991. DOI: 10.1006/jcph.1998.5962. URL: http://linkinghub.elsevier.com/retrieve/pii/S0021999198959629 (cit. on p. 82).

[157] B. Schumann. "Properties of Gallium Arsenide. EMIS Datareviews Series no. 2, second edition. INSPEC, The Institute of Electric Engineering, London and New York 1990, 790 + XXIV Seiten, zahlreiche Tabellen und Literaturangaben, Sachwortverzeichnis, ISBN 0-85296-485-4." In: *Crystal Research and Technology* 26.1 (1991), pp. 18–18. ISSN: 02321300. DOI: 10.1002/crat.2170260104. URL: http://doi.wiley.com/10.1002/crat.2170260829http://doi.wiley.com/10.1002/crat.2170260104 (cit. on p. 84).

[158] V. M. Glazov and A. S. Pashinkin. "Thermal expansion and heat capacity of GaAs and InAs." In: *Inorganic Materials* 36.3 (2000), pp. 225–231. ISSN: 0020-1685. DOI: 10.1007/BF02757926.

URL: http://link.springer.com/10.1007/BF02757926 (cit. on p. 84).

[159] Ronald H. Bogaard and C. Y. Ho. "Thermal Conductivity of Gallium Arsenide at High Temperature." In: *Thermal Conductivity 20*. Boston, MA: Springer US, 1989, pp. 163–170. DOI: 10.1007/978-1-4613-0761-7_15. URL: http://link.springer.com/10.1007/978-1-4613-0761-7{_}15 (cit. on p. 84).

[160] J. S. Blakemore. "Semiconducting and other major properties of gallium arsenide." In: *Journal of Applied Physics* 53.10 (1982), R123–R181. ISSN: 0021-8979. DOI: 10.1063/1.331665. URL: http://aip.scitation.org/doi/10.1063/1.331665 (cit. on p. 84).

[161] J. R. Meyer, M. R. Kruer, and F. J. Bartoli. "Optical heating in semiconductors: Laser damage in Ge, Si, InSb, and GaAs." In: *Journal of Applied Physics* 51.10 (1980), p. 5513. ISSN: 00218979. DOI: 10.1063/1.327469. URL: http://scitation.aip.org/content/aip/journal/jap/51/10/10.1063/1.327469 (cit. on pp. 84, 100).

[162] F. Kadlec, H. Němec, and P. Kužel. "Optical two-photon absorption in GaAs measured by optical-pump terahertz-probe spectroscopy." In: *Physical Review B* 70.12 (2004), p. 125205. ISSN: 1098-0121. DOI: 10.1103/PhysRevB.70.125205. URL: https://link.aps.org/doi/10.1103/PhysRevB.70.125205 (cit. on p. 84).

[163] Daniel Steiauf, Emmanouil Kioupakis, and Chris G. Van de Walle. "Auger Recombination in GaAs from First Principles." In: *ACS Photonics* 1.8 (2014), pp. 643–646. ISSN: 2330-4022. DOI: 10.1021/ph500119q. URL: http://pubs.acs.org/doi/10.1021/ph500119q (cit. on p. 84).

[164] D. E. Aspnes, S. M. Kelso, R. A. Logan, and R. Bhat. "Optical properties of AlxGa1-xAs." In: *Journal of Applied Physics* 60.2 (1986), pp. 754–767. ISSN: 00218979. DOI: 10.1063/1.337426 (cit. on p. 84).

[165] Bart J. Van Zeghbroeck. "Effective mass and energy bandgap of Ge, Si and GaAs, 1997 https://ecee.colorado.edu/~bart/book/effmass.htm." In: (). URL: https://ecee.colorado.edu/~bart/book/effmass.htm (cit. on p. 84).

[166] K. Itagaki and K. Yamaguchi. "High temperature heat contents of III-V semiconductor systems." In: *Thermochimica Acta* 163 (1990), pp. 1–12. ISSN: 0040-6031. DOI: 10.1016/0040-6031(90)

80374-8. URL: https://www.sciencedirect.com/science/article/pii/0040603190803748 (cit. on p. 85).

[167] Taeseok Kim, Manoj R. Pillai, Michael J. Aziz, Michael A. Scarpulla, Oscar D. Dubon, Kin M. Yu, Jeffrey W. Beeman, and Mark C. Ridgway. "Heat flow model for pulsed laser melting and rapid solidification of ion implanted GaAs." In: *Journal of Applied Physics* 108.1 (2010), p. 013508. ISSN: 0021-8979. DOI: 10.1063/1.3457106. URL: http://aip.scitation.org/doi/10.1063/1.3457106 (cit. on p. 85).

[168] Koichi Kakimoto and Taketoshi Hibiya. "Temperature dependence of viscosity of molten GaAs by an oscillating cup method." In: *Applied Physics Letters* 50.18 (1987), pp. 1249–1250. ISSN: 0003-6951. DOI: 10.1063/1.97924. URL: http://aip.scitation.org/doi/10.1063/1.97924 (cit. on p. 85).

[169] R. Rupp and G. Müller. "Experimental study of the surface tension of molten GaAs and its temperature dependence under controlled As-vapor pressure." In: *Journal of Crystal Growth* 113.1-2 (1991), pp. 131–139. ISSN: 00220248. DOI: 10.1016/0022-0248(91)90018-Z. URL: http://linkinghub.elsevier.com/retrieve/pii/002202489190018Z (cit. on p. 85).

[170] S.W. Winkler, I.M. Burakov, R. Stoian, N.M. Bulgakova, A. Husakou, A. Mermillod-Blondin, A. Rosenfeld, D. Ashkenasi, and I.V. Hertel. "Transient response of dielectric materials exposed to ultrafast laser radiation." In: *Applied Physics A* 84.4 (2006), pp. 413–422. ISSN: 0947-8396. DOI: 10.1007/s00339-006-3644-7. URL: http://link.springer.com/10.1007/s00339-006-3644-7 (cit. on p. 98).

[171] A. Rosenfeld, M. Lorenz, R. Stoian, and D. Ashkenasi. "Ultrashort-laser-pulse damage threshold of transparent materials and the role of incubation." In: *Applied Physics A: Materials Science & Processing* 69.7 (1999), S373–S376. ISSN: 0947-8396. DOI: 10.1007/s003390051419. URL: http://link.springer.com/10.1007/s003390051419 (cit. on p. 98).

[172] Dmitriy S. Ivanov and Leonid V. Zhigilei. "Combined atomistic-continuum modeling of short-pulse laser melting and disintegration of metal films." In: *Physical Review B* 68.6 (2003), p. 064114. ISSN: 0163-1829. DOI: 10.1103/PhysRevB.68.064114. URL: https://link.aps.org/doi/10.1103/PhysRevB.68.064114 (cit. on p. 98).

[173] George D. Tsibidis, Evangelos Skoulas, and Emmanuel Stratakis. "Ripple formation on nickel irradiated with radially polarized femtosecond beams." In: *Optics Letters* 40.22 (2015), p. 5172. ISSN: 0146-9592. DOI: 10.1364/OL.40.005172. URL: https://www.osapublishing.org/abstract.cfm?URI=ol-40-22-5172 (cit. on p. 99).

[174] Shutong He, Jijil JJ Nivas, K.K. Anoop, Antonio Vecchione, Minglie Hu, Riccardo Bruzzese, and Salvatore Amoruso. "Surface structures induced by ultrashort laser pulses: Formation mechanisms of ripples and grooves." In: *Applied Surface Science* 353 (2015), pp. 1214–1222. ISSN: 0169-4332. DOI: 10.1016/J.APSUSC.2015.07.016. URL: https://www.sciencedirect.com/science/article/pii/S0169433215015779 (cit. on p. 99).

COLOPHON

This document was typeset using the typographical look-and-feel `classicthesis` developed by André Miede and Ivo Pletikosić. The style was inspired by Robert Bringhurst's seminal book on typography "*The Elements of Typographic Style*". `classicthesis` is available for both LaTeX and LyX:

https://bitbucket.org/amiede/classicthesis/

Happy users of `classicthesis` usually send a real postcard to the author, a collection of postcards received so far is featured here:

http://postcards.miede.de/

Thank you very much for your feedback and contribution.